Bifurcations in single atom cavity QED

Thesis by

Michael A. Armen

In Partial Fulfillment of the Requirements

for the Degree of

Doctor of Philosophy
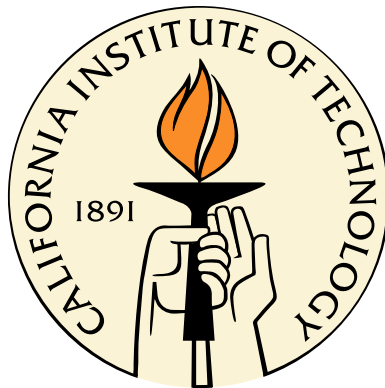
California Institute of Technology

Pasadena, California

2009

(Defended May 18, 2009)

Acknowledgments

Thank you...

To Levy: for an unexpectedly long-lived friendship. To Andy: for sharing my fine taste in clothing, coffee, and facial hair. To Stockton: I just saw you yesterday, so it's hard to be sentimental. Thanks for the pizza. To Au: you've always been my favorite. Don't tell the others. To McKeever: for being generally more grumpy and abrasive than me. To these dear, dear friends from the way, way back days of grad school: you are all equally to blame for my extended stay. Who knows what I would have accomplished in your absence. Shame on all of you.

To Kevin: for being a true friend through NorCal gloom, and laughing in the face of certain oily doom. Go with Christ, bra. To Tony: for always trying to pull me to the keen side. I will continue to deflect your efforts with all the apathy I can muster. But, please, don't stop!

To the many, many, many members of MabuchiLab that I have had the benefit of knowing over these many, many, many years of grad school: JW, Andre, Andrew D, Timmy, Ramon, Luc, Asa, Jen, Nathan, Chungsok, Andrew S, Joe K, Nicole, Orion, Kenny, Chucky, Dmitri, Gopal, Jie, Mike Z. Thank you all for enhancing the Mabuchi Group experience beyond the confines of a sub-basement lab. And, for the record, Mike Z fouled me repeatedly during our one-on-one exhibition match. There, it's in writing now.

To the friends that I remember individually but list jointly: Paul, Megan, Catharine, Kimmy, Wajma, Elizabeth, Amanda, Sena, Joe Z, Paige, Josh, Shac, Ali, Stojan, and Kevin B. Thanks for all the good times. I hope to see you all in the future.

To Sheri: where would I be without you? Probably digging ditches somewhere in

the Inland Empire. Thank you for everything. And please take care of that cactus; despite its prickly exterior, it longs for affection.

To Hideo: for years of support, guidance, and patience. Thank you for the experience and the opportunities you've given me. Also, I think we may have damaged your outdoor grill. Ask Tony for the details.

To Marcel and Mateo: thanks for all the chips and salsa.

To Chris Wallace: thank you, from the bottom of my heart. I continue to enjoy the fruits of your generosity.

To Mom and Dad: for all the patience, support, and hospitality at Casa de Armen. I love you both very much.

Abstract

Current research in single-atom cavity quantum electrodynamics largely emphasizes the input-output properties of strongly coupled systems, from normal mode splitting [1] to photon blockade [2]. But over the last decade, experiments have, with few exceptions, focused on relatively weak driving conditions. This thesis concentrates on a range of quantum nonlinear phenomena in the strong driving regime. In particular, I discuss the observation of random-telegraph phase switching in the light transmitted through a Fabry-Perot resonator containing one strongly coupled atom and 10-100 photons, confirming long-standing predictions of a phenomenon known as single-atom phase bistability [3, 4]. These results highlight the relevance of cavity quantum electrodynamics in the development of attojoule nanophotonic logic and signal processing. In addition, I consider a general class of bifurcation phenomena that are manifest within this physical setting. Here, focus is placed on the investigation of quantum-classical correspondence near semiclassical bifurcation points.

Contents

List of Figures

Chapter 1

Introduction

It's kind of incredible that the system to be analyzed *ad nauseam* throughout this thesis consists of just one atom coupled to the quantized electromagnetic field confined within an optical resonator [5]. Even worse, the primary model that I beat into the ground makes the additional simplifications of treating the atom as a two-level system (which it isn't) and the electromagnetic field as though it consists of a single mode (which it doesn't). Nevertheless, the system is quite complex [6] and resulting description is quite accurate [1, 2, 5, 7–13]. That such a simple underlying model can actually predict the behavior of real experimental systems is a testament to the incredible technical advances in atomic and optical physics over the last few decades [11, 14–18], providing exquisite tools for control and (ultimately) measurement of fundamental microscopic system dynamics. These developments have made possible real-time observations of open quantum systems for which a delicate interplay of coherent dynamics, dissipation, and quantum fluctuations determine the qualitative system behavior [3, 6, 11, 19, 20]. So, before jumping into the gory and the technical, I'd like to explain how such a simple model can be so accurate, and why it's not so simple.

1.1 The atom-field interaction: qualitative

Fundamental matter-radiation interactions may be experimentally realized within the context of optical cavity quantum electrodynamics (cavity QED) [21]. The key
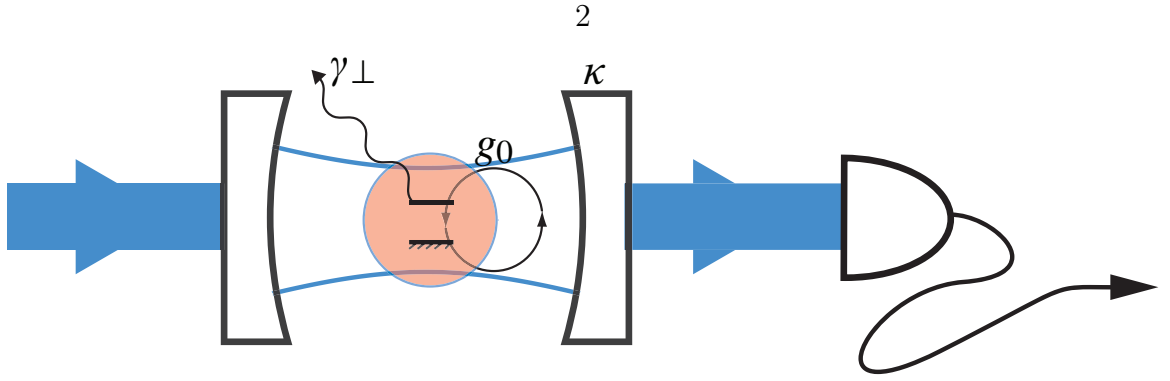
Figure 1.1: A cartoon schematic of the basic cavity QED system: a two level atom interacts with a single mode cavity. g is the atom-field coupling strength, $2\gamma_\perp$ is the atomic spontaneous emission rate, and κ is the cavity field decay rate. The system dynamics may be inferred (in real time) through detection of the cavity's decay field.

idea here is to place our precious atom, with all its natural limitations, within an electromagnetic resonator (the cavity) of high quality factor and small mode volume (depicted in Figure 1.1.) The high quality factor insures that the atom-radiation interaction may be long lived, while the small mode volume implies that a single quantum of the cavity excitation will have a larger influence on the atom than the remaining 4π steradians of vacuum modes. To a very good approximation atom-cavity coherent dynamics are described by the dipole Hamiltonian:

$$\hat{H}_{int} = \hat{d} \cdot \hat{E} \xrightarrow{max} d\sqrt{\frac{\hbar\omega}{2\epsilon_0 V_m}} \; , \tag{1.1}$$

where $\hat{d}$ is the atomic dipole operator, and $\hat{E}$ is the electric field operator. The right-hand side represents the maximum achievable coupling energy between the atom, with dipole moment d, and a single photon, with electric field magnitude $E_1 = \sqrt{\frac{\hbar\omega}{2\epsilon_0 V_m}}$. Here, ω is the optical transition frequency and V_m is the cavity mode volume.

In this idealized version of things, three fundamental rates characterize the unconditional behavior of this system [6]. First, the atomic internal states are coupled to the cavity mode by coupling constant g_0, which quantifies the rate of coherent energy exchange between the atom and cavity:

$$g_0 \equiv \frac{dE_1}{\hbar} \; . \tag{1.2}$$

This coherent interaction is limited by two dissipative mechanisms: energy can leave the system through atomic spontaneous emission into free space, at a rate $2\gamma_\perp$, and photons can leak out of the cavity at a rate 2κ. Presumably the coherent dynamics will tend to dominate the qualitative system behavior for sufficiently large g_0 – but how large is large enough?

Ideally g_0 should be large enough that: a single-photon excitation of the cavity is sufficient to saturate the atomic response, and conversely, a single atom inserted into the cavity has a profound (*i.e.*, nonlinear) effect on the field. The former condition can be achieved easily enough: since a saturated atom in free-space can, at most, scatter light at a rate $\sim \gamma_\perp$, it stands that a drive strength equivalent to one photon per unit radiative volume, $V_{rad} \sim \lambda^2 c/\gamma_\perp$, will saturate the atomic response. The mode volume dependence of Eq. 1.1 implies, then, that for a modified mode volume, V'_{rad}, this 'saturation photon number' will scale $\propto V'_{rad}/V_{rad}$ – in other words, for a cavity of mode volume V_m the number of cavity photons needed to overwhelm the puny atom is roughly $\sim (\gamma_\perp/g_0)^2$. Interestingly, this quantity depends solely on the cavity's mode *volume* and not at all on its *quality*.

This condition alone does not imply anything about the atom's qualitative influence on the cavity field. If the behavior of this atom is to have any chance at strongly influencing the cavity field, and therefore producing a measurable change in the cavity's (accessible) decay channel, two conditions must be met: first, the atomic influence over the cavity field should be enhanced through multiple passes of intracavity radiation; second, the cavity mode volume should be as small as possible, so that a large fraction of the mode interacts with the atomic cross-section per pass. Together, these conditions set a requirement on the ratio $g_0 : \kappa$.

Now, the standard way to quantify the atomic influence over the cavity field argues from atomic cross-sections, dipole moments, cumbersome factors of $\hbar$, *etc.* Such arguments have no place in my precious introduction[1]. A more elegant way

---

[1]If there are N atoms in a cavity that supports, on average, m bounces of the intracavity field, then the fraction of each intracavity excitation that is eaten by the atoms is roughly $Nm\sigma_0/A$, where σ_0 is the resonant atomic scattering cross-section and A is the mode's cross-sectional area. Demanding that this fraction be of order unity implies that $N \sim A/(m\sigma_0)$ atoms must be present. Substituting

to understand these relations is to consider the ratio of atomic to cavity energy dissipation: if this ratio is small, the presence of an atom will have a negligible effect on the cavity steady-state field. It's easy to estimate the atomic dissipation rate, it's simply $\gamma_\perp$, provided the atom is saturated by the laser field. For the cavity, though, there really is no maximal energy dissipation rate since the rate increases linearly with the intracavity photon number. Clearly, then, we'd like to keep this number down so that the atom's influence is maximized. Therefore, choosing judiciously an intracavity excitation number $(\gamma_\perp/g_0)^2$ (as derived above) will maximize the atomic losses while minimizing the cavity losses. In this case, the ratio of cavity to atomic loss is roughly: $\left[(\gamma_\perp/g_0)^2 \kappa\right]/\gamma_\perp = \kappa\gamma_\perp/g_0^2$. When this quantity is < 1, then for a single atom can have profound effect on the intracavity field.

As it turns out [6], these two dimensionless parameters quantify how 'interesting' the qualitative behavior of a cavity QED system will appear to the experimentalist who has access to, for example, the cavity's output field. In particular, for *saturation photon numbers* $n_0 \equiv 2\gamma_\perp^2/g_0^2 < 1$, a single photon can saturate the atomic response or cause a nonlinear system response, and for *critical atom numbers* $N_0 \equiv 2\gamma_\perp\kappa/g_0^2 < 1$, a single atom can significantly alter the cavity field and can therefore be easily detected. When both of these parameters are sub-unity, we are in the so-called 'strong coupling' regime of cavity QED.

In the opposite regime, where $(n_0, N_0) \gg 1$, the dynamical equations governing the system evolution may be expanded in powers $\left(n_0^{-1}, N_0^{-1}\right) \ll 1$, so that an initial quantum description may be rigorously reduced into a semiclassical description, but with small noise fluctuations caused by the underlying 'quantumness' [22]. The key, though, is that in the semiclassical regime, the quantum fluctuations are sufficiently small that we may safely think of the system's underlying 'quantumness' as merely a perturbation atop qualitatively semiclassical behavior.

$m \sim (c/2L)/\kappa$, $V_m \approx AL$, and $\sigma_0 \sim \lambda^2$ gives us $N \sim \kappa V_m/c\lambda^2$. Now, since $V_m \sim d^2c/(\hbar g_0^2\epsilon_0\lambda)$, we have $N \sim \kappa/g_0^2 \cdot \left(d^2/\epsilon_0\hbar\lambda^3\right)$, where the term in the parenthesis is the well-known expression for the spontaneous emission rate! Thus we recover the same result as in the main text. But really, is that satisfying?

1.2 The atom-field interaction: quantitative

Conceptually, the clearest starting point for modeling the system dynamics is the Jaynes-Cummings Hamiltonian [7]:

$$\hat{H}_{jc} = \omega_0 \hat{a}^\dagger \hat{a} + \omega_0 \hat{\sigma}_+ \hat{\sigma}_- + i g_0 (\hat{a}^\dagger \hat{\sigma}_- - \hat{a} \hat{\sigma}_+) \ , \tag{1.3}$$

whose terms account for, respectively, the field and atomic free evolution and the dipole interaction Hamiltonian (note, throughout this thesis I routinely set $\hbar = 1$ in Hamiltonian, eigenvalue, and dynamical equations – $\hbar$ is reinserted when required.) For simplicity, this Hamiltonian is expressed for the situation where the field and atomic frequencies are identically ω_0; the more general case will be dealt with in the subsequent chapters. The interaction Hamiltonian is scaled by g_0, the atom-photon coupling rate introduced in the previous section. $\hat{a}$ and $\hat{a}^\dagger$ are the field annihilation and creation operators, and $\hat{\sigma}_-$ and $\hat{\sigma}_+$ are the atomic lowering and raising operators.

The eigenstates of this coupled system are characterized by a sharing of excitation between the atom and cavity degrees of freedom. For n excitations in the system, these states reflect this notion of energy exchange as they are comprised of the superposition of the (uncoupled) n-excitation states:

$$|\pm, n\rangle = \frac{1}{\sqrt{2}} \left(|e, n-1\rangle \pm i |g, n\rangle \right), \tag{1.4}$$

with (g, e) here denoting the atomic ground and excited states. Although the bare uncoupled states, $|e, n-1\rangle$ and $|g, n\rangle$, are degenerate with eigenvalues $n\omega_0$, the coupled system eigenvalues possess a pronounced energy splitting as a results of the atom-field interaction:

$$E_\pm^{(n)} = n\omega_0 \pm \sqrt{n} g_0 \ . \tag{1.5}$$

This level structure is depicted in Figure 1.2 for up to three excitations in the system.

Obviously, the presence of dissipation can cloud this picture. When the strong
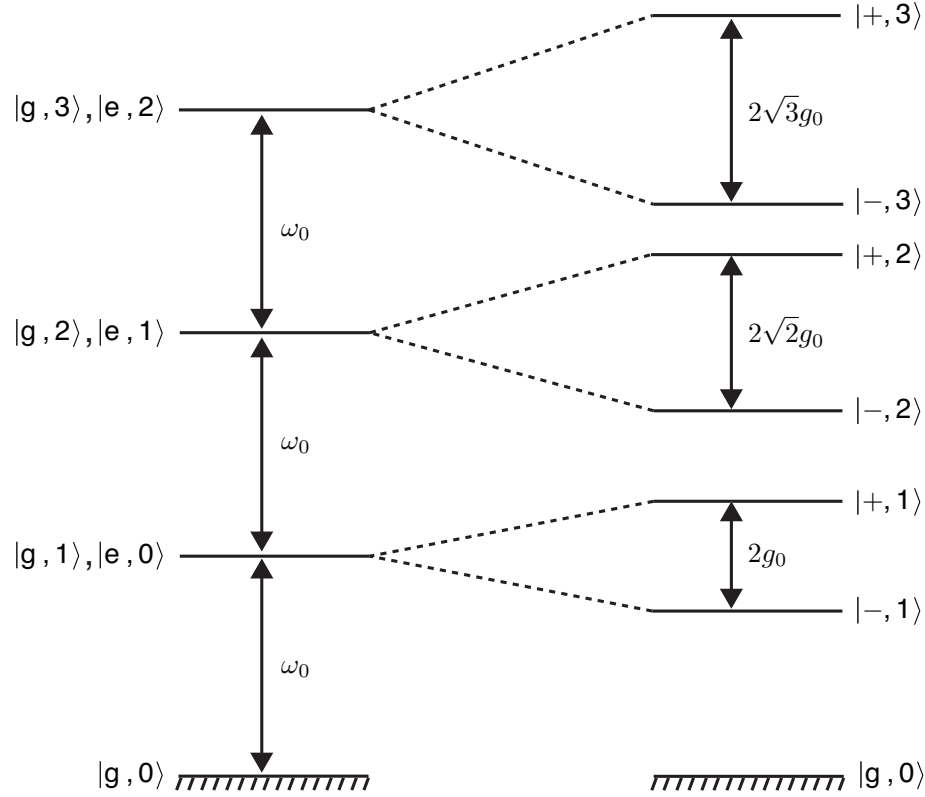
Figure 1.2: The resonant Jaynes-Cummings energy ladder for small excitations.

coupling conditions (outlined above) are met, however, the underlying structure of the Jaynes-Cummings Hamiltonian can be inferred from the systems input-output behavior. In particular, the observation of the low n normal mode splitting predicted by Eq. 1.5 is perhaps the most well-known experimental result of cavity QED [1], and most research over the last decade has focussed on the system input-output behavior in the low excitation regime [1, 2, 18, 23, 24]. This isn't surprising since it is in this regime that the anharmonic nature of the Jaynes-Cummings eigenstates are most evident: $i.e.$, relative to the uncoupled resonant frequency ω_0, the detuning between successive levels decreases rapidly as the system is driven to larger excitation levels:

$$g_0 \rightarrow (\sqrt{2} - 1)g_0 \rightarrow (\sqrt{3} - \sqrt{2})g_0 \rightarrow \ldots \rightarrow (\sqrt{n+1} - \sqrt{n})g_0 \ . \qquad (1.6)$$

For very large excitations, this detuning is $\sim 1/\sqrt{n}$ and the transmission spectrum of this coupled system approaches that of an empty cavity. This behavior is depicted
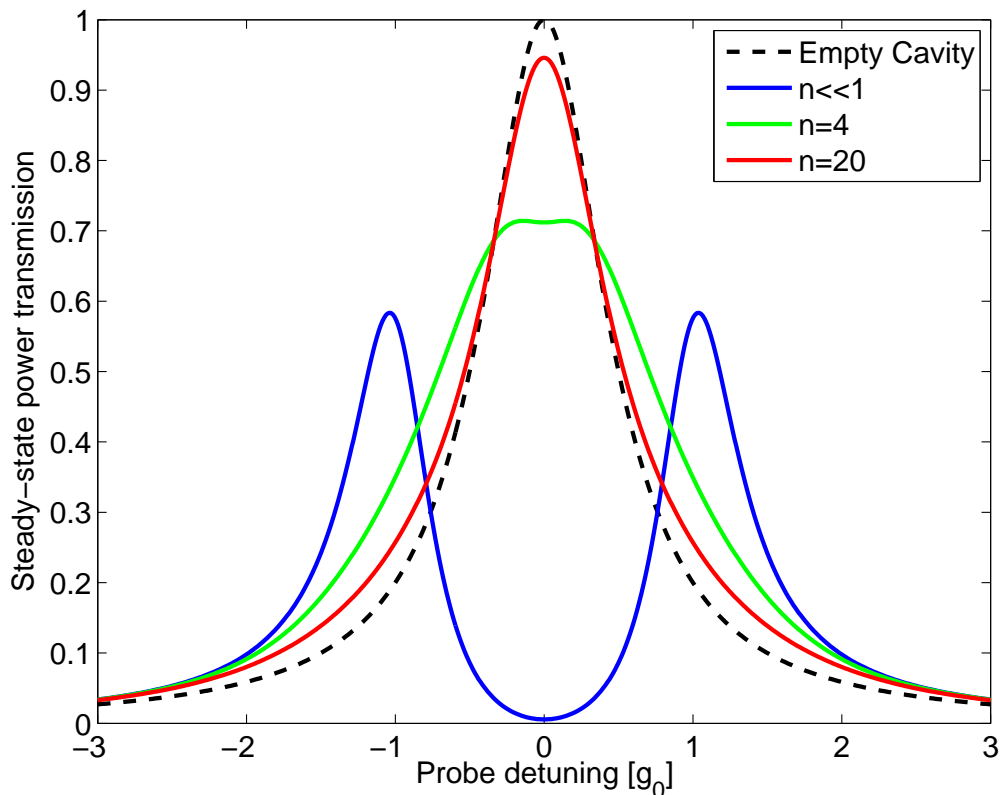
Figure 1.3: Dependence of the steady-state system transmission on the drive strength. The normal mode splitting for low excitations (blue) disappears in the larger excitation regime. The used parameter values, $\{g_0, \kappa, \gamma_\perp\}/2\pi = \{16, 8.0, 2.6\}$MHz, are those of the experimental system described in Chapter 2. The empty cavity response (dashed black) is a Lorentzian of full width $\delta f = 2\kappa/2\pi$.

in Figure 1.3, which shows the steady-state transmission over a range of excitation strengths. Here, the excitation strength (given in the legend) is parametrized by the mean intracavity photon number that it would generate for an atom-less cavity.

1.3 The atom-field interaction: nonlinearity and bifurcations

From the above discussion, one might conclude that the 'interesting' system behavior disappears in the regime of large excitation. This is in fact true for a weakly coupled system. If our atom interacts with a coherent field of mean photon number $\bar{n} \gg 1$

and Poisson fluctuations $\sqrt{\bar{n}}$, the system will be excited over a range of eigenvalues

$$2\sqrt{\bar{n}+\sqrt{\bar{n}}}g_0 - 2\sqrt{\bar{n}-\sqrt{\bar{n}}}g_0 \approx 2\sqrt{\bar{n}}g_0\left[(1+\frac{1}{2\sqrt{\bar{n}}}) - (1-\frac{1}{2\sqrt{\bar{n}}})\right] \rightarrow 2g_0. \quad (1.7)$$

When $\{\gamma_\perp, \kappa\} \gg g_0$ these dynamical variations are negligible in comparison to the system dephasing. In this limit, we are justified in making the approximation $2\sqrt{n}g_0 \rightarrow 2\sqrt{\bar{n}}g_0$ and treating the electromagnetic field semiclassically. Thus, we recover the semiclassical limit of atomic dressed states

$$|\pm\rangle = \frac{1}{\sqrt{2}}\left(|e\rangle \pm i|g\rangle\right) , \quad (1.8)$$

with constant frequency splitting $2\sqrt{\bar{n}}g_0 \equiv \Omega$, where Ω is the Rabi frequency [25, 26]. In this regime, the system's macroscopic behavior can be understood from a semi-classical model with small (quantum) fluctuations tacked on [6, 22]. But this is not necessarily true for a strongly-coupled system. In this case, fluctuations over the photon number distribution can not be ignored through the substitution $n \rightarrow \bar{n}$, since the energy variations over this distribution are quite large relative to the other system dynamical rates. Under strong coupling conditions, the interplay between dissipative and coherent dynamics can reorganize the system's qualitative behavior; that is, quantum fluctuations can not simply be 'tacked on' after the fact. In fact, it is in the *weak-driving* regime where the system's behavior is, in some sense, more predictable. In particular, the vacuum-Rabi splitting can be explained using a semiclassical description of the system (discussed in Section 2.1.3.4).

The work presented in this thesis concentrates on the interesting effects that reside in this large excitation regime. In Chapter 2, I describe an experiment [27] in which individual spontaneous emission events from a strongly-coupled single atom cause phase-switching of an intracavity field of mean photon numbers in the range $10 \leftrightarrow 100$, thereby confirming the long-existing prediction of optical phase bistability, which is also known as spontaneous dressed-state polarization [3, 4, 28]. And while this particular experiment suffers from rather modest results (due to the values of the

fundamental parameters, g_0 and κ), this demonstration highlights the relevance of cavity QED in future designs of ultralow energy nonlinear optical elements [29, 30]. Specifically, the ability of a single spontaneous emission event to change the properties of many photons is of relevance to the developing field of nanophotonic logic and signal processing.

But, in a larger sense, studying such nonlinear behavior within strongly coupled quantum systems is essential to understanding the interface between quantum and classical worlds. In the case of phase bistability, the qualitative nature of the system's macroscopic behavior is completely reorganized by the underlying quantum fluctuations. As expected, the standard semiclassical theory fails to capture the observed behavior in this regime. Instead, intuition must be sought from the underlying structure of the idealized quantum system, and the critical role spontaneous emission plays within it. Using this intuition, we can form a more appropriate semiclassical description which captures the observed behavior.

The utility of a semiclassical description becomes clear in Chapter 3. Here, I describe a study of bifurcations in the standard model of cavity QED with damping and driving [20]. Emphasis is placed on applying computational tools and methods to the semiclassical model in order to find dynamically interesting parameter regimes of the fully quantum problem. In particular, I consider bifurcation phenomena as focal points for the investigation of quantum-(semi)classical correspondence in cavity nonlinear optics. A general approach to characterizing the semiclassical bifurcation set is presented, and numerical simulations of the quantum dynamics about bifurcation points lead to observations of self-oscillation and bifurcation-type behavior in an experimentally accessible parameter regime for single-atom cavity QED. As we will see, a surprisingly wide range of input-output characteristics are supported by this small and simple state space.

Chapter 2

Phase Bistability

Section 2.1 introduces the cavity QED model. This is all standard stuff [21], but I include it here for your convenience. Section 2.2 describes the theoretical background for phase bistability in particular, and includes an introduction to some of the computational tools used for the experimental data analysis. Section 2.3 describes the apparatus and the experimental results.

2.1 Cavity QED background

We consider the driven Jaynes-Cummings Hamiltonian [6] which models the interaction of a single mode of an optical cavity having resonant frequency ω_c, with a two-level atom, comprised of a ground state $|g\rangle$ and an excited state $|e\rangle$ separated by a frequency ω_a. For an atom-field coupling constant g_0 and a drive field with amplitude $\mathcal{E}$ at frequency ω_p, the Hamiltonian is [$\hbar = 1$]:

$$\hat{\mathcal{H}} = \omega_c \hat{a}^\dagger \hat{a} + \omega_a \hat{\sigma}_+ \hat{\sigma}_- + ig_0(\hat{a}^\dagger \hat{\sigma}_- - \hat{a}\hat{\sigma}_+) + i\mathcal{E}(e^{-i\omega_p t}\hat{a}^\dagger - e^{i\omega_p t}\hat{a}) \;, \qquad (2.1)$$

where $\hat{a}$ is the field annihilation operator and $\hat{\sigma}_- = |g\rangle\langle e|$ is the atomic lowering operator. The pesky time dependence in Eq. 2.1 can be eliminated by transforming the dynamics into a frame rotating at the drive frequency. Formally this is accomplished through the transformation

$$\hat{T} = e^{-i\omega_0 t \hat{a}^\dagger \hat{a}} e^{-i\omega_0 t \hat{\sigma}_+ \hat{\sigma}_-} \;, \qquad (2.2)$$

so that we now evolve a rotating state vectors $|\psi\rangle$,

$$|\chi\rangle \rightarrow \hat{T}^\dagger |\chi\rangle \equiv |\psi\rangle \tag{2.3}$$

under the transformed Hamiltonian[1]

$$\hat{\mathcal{H}} \rightarrow \hat{T}^\dagger \hat{\mathcal{H}} \hat{T} + i\frac{\partial \hat{T}^\dagger}{\partial t}T \equiv \hat{H} \ . \tag{2.4}$$

This new Hamiltonian is expressed as

$$\hat{H} = \hat{H}_{jc} + \hat{H}_d \ , \tag{2.5}$$

where $\hat{H}_d$ is the modified (and now time independent) drive term

$$\hat{H}_d = i\mathcal{E}\left(\hat{a}^\dagger - \hat{a}\right) \ , \tag{2.6}$$

and $\hat{H}_{jc}$ is the Jaynes-Cummings Hamiltonian

$$\hat{H}_{jc} = \Theta \hat{a}^\dagger \hat{a} + \Delta \hat{\sigma}_+ \hat{\sigma}_- + ig_0(\hat{a}^\dagger \hat{\sigma}_- - \hat{a}\hat{\sigma}_+) \ . \tag{2.7}$$

Here, $\Theta = \omega_c - \omega_p$ is the cavity-probe detuning, and $\Delta = \omega_a - \omega_p$ is the atom-probe detuning.

---

[1]It's easy to verify that if an initial state $|\chi\rangle$ satisfies $i|\dot{\chi}\rangle = \hat{\mathcal{H}}|\chi\rangle$, then the transformed state $|\psi\rangle$ will satisfy $i|\dot{\psi}\rangle = \hat{H}|\psi\rangle$.

2.1.1 System eigenstructure

After expanding the annihilation operators in the standard Fock basis [33], the Hamiltonian in matrix form is

$$\hat{H}_{jc} = \begin{bmatrix} \Delta\hat{\sigma}_+\hat{\sigma}_- & -ig_0\hat{\sigma}_+ & 0 & 0 & \cdots \\ ig_0\hat{\sigma}_- & \Theta + \Delta\hat{\sigma}_+\hat{\sigma}_- & -\sqrt{2}ig_0\hat{\sigma}_+ & 0 & 0 \\ 0 & \sqrt{2}ig_0\hat{\sigma}_- & 2\Theta + \Delta\hat{\sigma}_+\hat{\sigma}_- & -\sqrt{3}ig_0\hat{\sigma}_+ & 0 \\ 0 & 0 & \sqrt{3}ig_0\hat{\sigma}_- & 3\Theta + \Delta\hat{\sigma}_+\hat{\sigma}_- & -\sqrt{4}ig_0\hat{\sigma}_+ \\ \vdots & 0 & 0 & \sqrt{4}ig_0\hat{\sigma}_- & \ddots \end{bmatrix} . \quad (2.8)$$

We can break up the Hamiltonian into block diagonal elements that are decoupled from one another,[2]

$$\begin{bmatrix} (n-1)\Theta + \Delta\hat{\sigma}_+\hat{\sigma}_- & -\sqrt{n}ig_0\hat{\sigma}_+ \\ \sqrt{n}ig_0\hat{\sigma}_- & n\Theta + \Delta\hat{\sigma}_+\hat{\sigma}_- \end{bmatrix} =$$

$$\begin{bmatrix} (n-1)\Theta & 0 & 0 & 0 \\ 0 & (n-1)\Theta + \Delta & -\sqrt{n}ig_0 & 0 \\ 0 & \sqrt{n}ig_0 & n\Theta & 0 \\ 0 & 0 & 0 & n\Theta + \Delta \end{bmatrix} . \quad (2.9)$$

Therefore, we need only diagonalize the general form[3]

$$\hat{H}_{jc}^{(n)} = \begin{bmatrix} (n-1)\Theta + \Delta & -\sqrt{n}ig_0 \\ \sqrt{n}ig_0 & n\Theta \end{bmatrix} . \quad (2.11)$$

---

[2]I use the atomic basis convention $|g\rangle = \begin{bmatrix} 1 & 0 \end{bmatrix}^T$ and $|e\rangle = \begin{bmatrix} 0 & 1 \end{bmatrix}^T$.
[3]We've ignored the first block diagonal element for the ground-state

$$\hat{H}_{jc}^{gs} = \begin{bmatrix} 0 \end{bmatrix} . \quad (2.10)$$
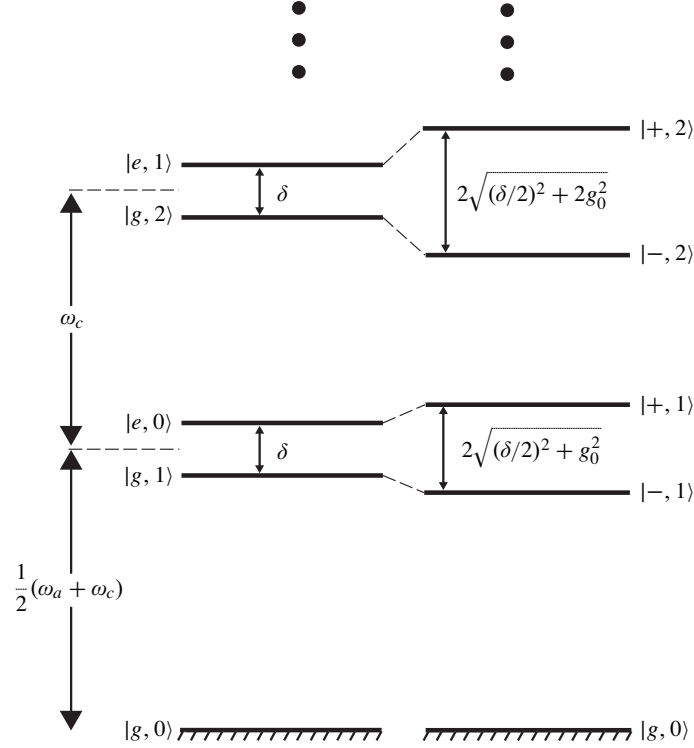
Figure 2.1: Energy level diagram of the Jaynes-Cummings Hamiltonian for general parameters. For clarity, the levels are displayed in the non-rotating frame.

The eigenvalues of this matrix are

$$
\begin{aligned}
E_n^{\pm} &= \frac{1}{2}\left[2(n-1)\Theta + (\omega_a + \omega_c) \pm \sqrt{(\omega_a - \omega_c)^2 + 4ng_0^2}\right] \\
&= n\Theta + \delta/2 \pm \sqrt{(\delta/2)^2 + ng_0^2}
\end{aligned}
\tag{2.12}
$$

with associated eigenvectors

$$
|\pm, n\rangle = \sqrt{\frac{1}{2}}\left[\sqrt{1 \pm \frac{\delta}{\sqrt{\delta^2 + 4ng_0^2}}}\,|e, n-1\rangle \pm i\sqrt{1 \mp \frac{\delta}{\sqrt{\delta^2 + 4ng_0^2}}}\,|g, n\rangle\right] . \tag{2.13}
$$

$\delta = \Delta - \Theta = \omega_a - \omega_c$ is the atom-cavity detuning. This energy spectrum, in the non-rotated frame, is depicted in Figure 2.1.

2.1.2 Some salient features that will be referred to later

2.1.2.1 Adiabatic passage

The resonant system eigenstates 1.4 represent an equal sharing of excitation between the atom and cavity. But as $|\delta|$ increases this amount of sharing decreases, and the upper and lower eigenstates, Eq. 2.13, develop either an atom-like or cavity-like behavior. For $\delta \gg 0$ the lower eigenstate, $|-, n\rangle$, is comprised primarily of $|g, n\rangle$ and is therefore more 'cavity-like' since the excitation is primarily within the cavity mode. For $\delta \ll 0$ the opposite is true: the lower eigenstate is now more 'atom-like' with excitation residing in the atomic internal states. This behavior can be easily understood from energy spectrum in Figure 2.1: while the eigenstate energies are symmetric with regards to the sign of δ, the uncoupled state energies are not. For a positive atom-cavity detuning, for example, the uncoupled excited atomic state has a stronger resemblance to the upper eigenstates, while the ground state is closer to the lower eigenstate.

Taking the limit $g_0 \to 0$ for the states 2.13 we obtain

$$
\begin{aligned}
\lim_{g_0 \to 0} |+, n\rangle \to & \left[\begin{array}{l} i|g, n\rangle \text{ , for } \delta < 0 \\ |e, n-1\rangle \text{ , for } \delta > 0 \end{array} \right] , \\
\lim_{g_0 \to 0} |-, n\rangle \to & \left[\begin{array}{l} |e, n-1\rangle \text{ , for } \delta < 0 \\ -i|g, n\rangle \text{ , for } \delta > 0 \end{array} \right] .
\end{aligned}
\tag{2.14}
$$

This indicates that if the atom-cavity coupling is turned on *slowly*, an initially decoupled state like $|g, n\rangle$ will tend towards $\pm i|\pm, n\rangle$, with the particular dressed state determined by the atom-cavity detuning. This is exactly related to the experimental scenario where an atom, initially prepared in the state $|g\rangle$, is introduced into a cavity initially prepared in the state $|n\rangle$. Note that for $g_0 > 0$, the lower eigenstate has lower energy than the *decoupled* system, and therefore the (spatially-varying) cavity mode, Eq. 2.15, can form a binding potential for the atom-cavity.

2.1.2.2 Spatial mode structure and forces on the atom

For modern experiments in cavity QED that employ laser cooling and trapping of atomic motion, the quantum dynamical timescales are generally very well separated from the characteristic timescales associated with atomic motion. In this case, it is generally convenient to account for the cavity mode structure through a spatially varying coupling constant [11]

$$g(r, z) = g_0 e^{-r^2/w_0^2} \cos kx \ . \tag{2.15}$$

Here, x is the position along the cavity axis, $r = \sqrt{y^2 + z^2}$ is the radial distance from the cavity axis, $k = 2\pi/\lambda$ is the wavevector, and we have assumed that the TEM_{00} mode, with waist w_0, is being used [34].

For the experiment in Section 2.3, we will generally be concerned with atomic motional effects when the cavity mean photon number is very large. In this case, we are justified in treating the field semiclassically. Taking expectations over the field, $\langle \hat{a} \rangle \to \alpha$ in Eq. 2.7, we arrive at the atomic, or semiclassical Hamiltonian

$$\hat{H}_{sc} = \Delta \hat{\sigma}_+ \hat{\sigma}_- + i g_0 (\alpha^* \hat{\sigma}_- - \alpha \hat{\sigma}_+) \ . \tag{2.16}$$

The eigenvalues and eigenvectors are

$$E^\pm = \frac{1}{2} \left(\Delta \pm \sqrt{\Delta^2 + 4\bar{n} g_0^2} \right) \ ,$$
$$|\pm\rangle = \sqrt{\frac{1}{2}} \left[\sqrt{1 \pm \frac{\Delta}{\sqrt{\Delta^2 + 4\bar{n} g_0^2}}} |e\rangle \pm i e^{-i\phi} \sqrt{1 \mp \frac{\Delta}{\sqrt{\Delta^2 + 4\bar{n} g_0^2}}} |g\rangle \right] \ , \tag{2.17}$$

which are the well known semiclassical dressed states and associated energies. Here, we've parameterized the complex field amplitude as $\alpha = |\alpha| e^{i\phi}$, and $\bar{n} = |\alpha|^2$ is the mean cavity photon number. The complex phase in the eigenvectors above has its origins in the oscillation phase of the drive field [26]. For a fixed ϕ we can just as well treat α as real by simply absorbing this phase into our definition of the rotating frame (which in this case is at the probing frequency.) I only left it in the definition above

to highlight the fact that the relative phase in these eigenstates is actually defined by the drive field. This is a manifestation of the fact that the real and imaginary components of the dipole moment are defined by the field phase:

$$\langle \hat{\sigma}_- + \hat{\sigma}_+ \rangle^\pm = \pm \sqrt{\frac{4ng_0^2}{\Delta^2 + 4ng_0^2}} \sin \phi$$
$$\langle i(\hat{\sigma}_- - \hat{\sigma}_+) \rangle^\pm = \pm \sqrt{\frac{4ng_0^2}{\Delta^2 + 4ng_0^2}} \cos \phi \ . \tag{2.18}$$

For posterity, we note that the population difference is given by

$$\langle \hat{\sigma}_z \rangle^\pm = \frac{\pm\Delta}{\sqrt{\Delta^2 + 4ng_0^2}} \ . \tag{2.19}$$

All this implies, amongst other things, that for interactions with traveling waves the relative phase in the eigenvectors is position dependent, since the field can be written

$$\mathcal{E}_{tw}(t) \propto \cos(kx - \omega t + \phi) \ . \tag{2.20}$$

This is not the case for standing waves, which we will employ. Here, the spatial and temporal degrees of freedom decouple

$$\mathcal{E}_{sw}(t) \propto \cos kx \, \cos(\omega t + \phi) \ . \tag{2.21}$$

Therefore, for a standing wave cavity the drive phase decouples from position and we write

$$|\pm\rangle = \sqrt{\frac{1}{2}} \left[\sqrt{1 \pm \frac{\Delta}{\sqrt{\Delta^2 + 4ng_0^2}}} |e\rangle \pm i \sqrt{1 \mp \frac{\Delta}{\sqrt{\Delta^2 + 4ng_0^2}}} |g\rangle \right] \ . \tag{2.22}$$

There is, however, the complication of *nodes* in a standing wave cavity. In particular, as an atom passes through a node ($kx = (2m+1)\pi/2$ in 2.15) the sign of the field changes. In the resonant case, $\Delta = 0$, this sign change implies an effective switching of the dressed state $|\pm\rangle \rightarrow |\mp\rangle$. This effect will be of some relevance for the data

analysis of Section 2.3.7.4.

Finally, returning to the issue of forces, the form of the eigenvalues 2.12 implies that the atom moves within a conservative potential defined by 2.15. In the resonant case, we have the potential

$$E^{\pm}(r, z) = \pm\sqrt{\bar{n}}g_0 e^{-r^2/w_0^2}|\cos kx| \; . \tag{2.23}$$

Therefore, the $|-\rangle$ state will see a confining potential and will be attracted to anti-nodes of the standing wave. In contrast, the $|+\rangle$ state will be radially repelled from the cavity, and will be funneled into field nodes. Note, for the case of nonzero Δ the magnitude of these forces is reduced, but the qualitative picture provided above still holds.

2.1.3 Dissipation and the master equation

In order to account for dissipation in the model, we need to incorporate the Hamiltonian dynamics into a master equation for the non-unitary evolution of a joint atom-cavity density operator $\hat{\rho}$. Under the two dissipation channels, $\gamma_{\perp}$ and κ, the unconditional master equation has the form

$$\dot{\hat{\rho}} = -i[\hat{H}, \hat{\rho}] + 2\kappa\hat{\mathcal{D}}[\hat{a}]\hat{\rho} + 2\gamma_{\perp}\hat{\mathcal{D}}[\hat{\sigma}_-]\hat{\rho} \; . \tag{2.24}$$

$\hat{H} = \hat{H}_{jc} + \hat{H}_d$ is the Hamiltonian in the rotating frame comprised of the Jaynes-Cummings and drive components, and the super-operator, $\hat{\mathcal{D}}$, accounts for decay of system excitation into the environment through the ubiquitous Lindblad decay term [35, 36]. For arbitrary system operators $\hat{O}$ and $\hat{P}$,

$$\hat{\mathcal{D}}[\hat{O}]\hat{P} = \hat{O}\hat{P}\hat{O}^{\dagger} - \frac{1}{2}\hat{O}^{\dagger}\hat{O}\hat{P} - \frac{1}{2}\hat{P}\hat{O}^{\dagger}\hat{O} \; . \tag{2.25}$$

Eq. 2.25 represents the most general form of Markovian dissipation that is trace preserving and therefore allows for multiple independent decay channels to summed [36]

.

2.1.3.1 The external drive

In the presence of dissipation a drive term is necessary to have a nontrivial steady-state solutions to 2.24. To remedy this behavior we incorporate the term

$$\hat{H}_d = i\mathcal{E}(\hat{a}^\dagger - \hat{a}) \ . \tag{2.26}$$

The phase convention in 2.26 insures that the empty[4] cavity steady-state is the coherent state $|\alpha\rangle = |\mathcal{E}/(\kappa + i\Theta)\rangle$. When driven on resonance, this steady-state coherent state amplitude is real valued, with $\alpha = \mathcal{E}/\kappa$.

Unlike the Jaynes-Cummings Hamiltonian 2.7, $\hat{H}_d$ couples blocks of different excitation. We have

$$\begin{bmatrix} (n-1)\Theta + \Delta\hat{\sigma}_+\hat{\sigma}_- & \sqrt{n}i(g_0\hat{\sigma}_+ + \mathcal{E}) \\ \sqrt{n}i(g_0\hat{\sigma}_+ + \mathcal{E}) & n\Theta + \Delta\hat{\sigma}_+\hat{\sigma}_- \end{bmatrix} =$$

$$\begin{bmatrix} (n-1)\Theta & 0 & -\sqrt{n}i\mathcal{E} & 0 \\ 0 & (n-1)\Theta + \Delta & -\sqrt{n}ig_0 & -\sqrt{n}i\mathcal{E} \\ \sqrt{n}i\mathcal{E} & \sqrt{n}ig_0 & n\Theta & 0 \\ 0 & \sqrt{n}i\mathcal{E} & 0 & n\Theta + \Delta \end{bmatrix} \tag{2.27}$$

which represents the driving term pushing the system into eigenstates of higher photon numbers through the (far) off diagonal elements. Furthermore, this drive couples upper and lower dressed states of adjacent blocks

$$\ldots \leftrightarrow |\pm, n-1\rangle \leftrightarrow |\pm, n\rangle \leftrightarrow |\pm, n+1\rangle \leftrightarrow \ldots, \tag{2.28}$$

and

$$\ldots \leftrightarrow |\pm, n-1\rangle \leftrightarrow |\mp, n\rangle \leftrightarrow |\pm, n+1\rangle \leftrightarrow \ldots. \tag{2.29}$$

---

[4]I use the phrase 'empty cavity' here, and throughout this thesis, to describe the situation where no atom is present. This phrase is not meant to imply that the cavity field is unexcited.

These two excitation pathways, however, will be relatively detuned by $\sim \pm\sqrt{n}g_0$, and, therefore, will not be simultaneously resonant for intra-cavity photon numbers where $\sqrt{n}g_0 \gg \{\kappa, \gamma_\perp\}$.

2.1.3.2 Displacing the mean field

For problems in the low-excitation regime, the master equation 2.24 may be integrated on a PC without much difficulty. However, when the drive is large enough so that the mean coherent state amplitude $\alpha = \mathcal{E}/\kappa \gg 1$, the large intra-cavity photon numbers become problematic computationally since the required Fock space dimension scales as $\langle \hat{a}^\dagger \hat{a} \rangle \approx |\alpha|^2$. Often, the intra-cavity field is very close to a coherent state but with *small* variations associated with the interesting atom-field dynamics. In this case, we can displace away the large mean field α, which is essentially a classical term and therefore uninteresting, so that we can focus on the small quantum fluctuations, which we *know* to be interesting.

The displacement operator [35],

$$\hat{D}(\alpha) = e^{\alpha\hat{a}^\dagger - \alpha^*\hat{a}} = e^{\alpha\hat{a}^\dagger}e^{-\alpha^*\hat{a}}e^{-|\alpha|^2/2} , \tag{2.30}$$

has the convenient property that it transforms the vacuum state as $\hat{D}(\alpha)|0\rangle \to |\alpha\rangle$ and the annihilation operator as

$$\hat{D}^\dagger(\alpha)\hat{a}\hat{D}(\alpha) = \hat{a} + \alpha . \tag{2.31}$$

Using 2.30, we displace the dynamics so that $\hat{H} \to \hat{D}^\dagger(\alpha)\hat{H}\hat{D}(\alpha)$ and obtain

$$\begin{aligned}
\hat{H}'_{jc} = {}& \Theta\hat{a}^\dagger\hat{a} + \Delta\hat{\sigma}_+\hat{\sigma}_- + ig_0(\hat{a}^\dagger\hat{\sigma}_- - \hat{a}\hat{\sigma}_+) \\
& + \Theta\left(\alpha\hat{a}^\dagger + \alpha^*\hat{a} + |\alpha|^2\right) + ig_0(\alpha^*\hat{\sigma}_- - \alpha\hat{\sigma}_+) ,
\end{aligned} \tag{2.32}$$

and

$$\hat{H}'_d = i\mathcal{E}\left(\hat{a}^\dagger - \hat{a}\right) + i\mathcal{E}\left(\alpha^* - \alpha\right) . \tag{2.33}$$

Unlike the transformation 2.2, this displacement *does* affect the field dissipation term:

$$2\kappa\hat{\mathcal{D}}[\hat{a}]\hat{\rho} \rightarrow \hat{D}^\dagger(\alpha)\left\{2\kappa\hat{\mathcal{D}}[\hat{a}]\left(\hat{D}(\alpha)\hat{\rho}'\hat{D}^\dagger(\alpha)\right)\right\}\hat{D}(\alpha)$$
$$\rightarrow 2\kappa\hat{\mathcal{D}}[\hat{a}]\hat{\rho}' - i\left[i\kappa\left(\alpha^*\hat{a} - \alpha\hat{a}^\dagger\right), \hat{\rho}'\right] \ , \tag{2.34}$$

where $\hat{\rho}' = \hat{D}^\dagger(\alpha)\hat{\rho}\hat{D}(\alpha)$ is the new (displaced) density matrix.

Using a result from Section 2.1.3.3 we make the judicious choice

$$\alpha = \frac{\mathcal{E}}{\kappa + i\Theta} \ , \tag{2.35}$$

and, after a few lines of algebra, we find that our transformed density matrix satisfies the following evolution (after dropping constant terms)

$$\dot{\hat{\rho}}' = -i[\hat{H}_{jc} + \hat{H}_d', \hat{\rho}] + 2\kappa\hat{\mathcal{D}}[\hat{a}]\hat{\rho}' + 2\gamma_\perp\hat{\mathcal{D}}[\hat{\sigma}_-]\hat{\rho}' \ , \tag{2.36}$$

$$\hat{H}_d' = -i\left(\frac{g_0\mathcal{E}}{\kappa + i\Theta}\right)\hat{\sigma}_+ + i\left(\frac{g_0\mathcal{E}}{\kappa - i\Theta}\right)\hat{\sigma}_- \ . \tag{2.37}$$

Evidently, the dynamics in the transformed frame are identical to those in the original frame – the only difference is the form of the drive term. In this new picture, the drive field does not excite the cavity mode but instead directly excites the atom. Of course, the original picture, with the drive exciting the cavity, is in some sense more physically motivated, but it's also quite biased – the cavity and the atom are *both* coupled to the drive field, after all. Now, this new picture wherein the drive term only excites the atoms is just as biased, but it's also very convenient since we may now work within the displaced Fock space, which can have much lower dimension. In any case, it stands that from a solution $\hat{\rho}'$ of the displaced master equation 2.36 we may construct the solution $\hat{\rho} = \hat{D}(\alpha)\hat{\rho}'\hat{D}^\dagger(\alpha)$ to the dynamics 2.24 of the more 'natural' picture. Similarly, if we're only interested in computing operator expectation values

we can use, for example,

$$\operatorname{Tr}[\hat{a}\hat{\rho}] = \operatorname{Tr}[\hat{a}\hat{\rho}'] + \alpha \ , \tag{2.38}$$

which is much more convenient than transforming the entire density matrix.

2.1.3.3 Semiclassical description: the Maxwell-Bloch Equations

Note, the results of this section are expanded upon in great detail in Chapter 3.

Unfortunately, aside from brute numerical integration, it's difficult to extract much information from the master equation 2.24 because analytic treatments are possible for very few applications. For many parameter regimes, however, the operator expectation equations of motion can provide much insight. Using that $\frac{d\langle\hat{O}\rangle}{dt} = \langle\hat{O}\dot{\hat{\rho}}\rangle$, we get the operator equations of motion:

$$\begin{aligned}
\frac{d\langle\hat{a}\rangle}{dt} &= -(\kappa + i\Theta)\langle\hat{a}\rangle + g_0\langle\hat{\sigma}_-\rangle + \mathcal{E} \\
\frac{d\langle\hat{\sigma}_-\rangle}{dt} &= -(\gamma_\perp + i\Delta)\langle\hat{\sigma}_-\rangle + g_0\langle\hat{a}\hat{\sigma}_z\rangle \\
\frac{d\langle\hat{\sigma}_z\rangle}{dt} &= -2\gamma_\perp(\langle\hat{\sigma}_z\rangle + 1) - 2g_0(\langle\hat{a}^\dagger\hat{\sigma}_-\rangle + \langle\hat{\sigma}_+\hat{a}\rangle) \ .
\end{aligned} \tag{2.39}$$

$\hat{\sigma}_z = [\hat{\sigma}_+, \hat{\sigma}_-] = |e\rangle\langle e| - |g\rangle\langle g|$ measures the atomic population difference. Unfortunately, these equations are not amenable to analytic analysis either because they are not closed – the dual-operator expectation values, like $\langle\hat{a}\hat{\sigma}_z\rangle$, muck everything up. We can, of course, simply factor these terms, $e.g.$, $\langle\hat{a}\hat{\sigma}_z\rangle \to \langle\hat{a}\rangle\langle\hat{\sigma}_z\rangle$, but in doing so we necessarily introduce errors associated with the atom-field entanglement. Therefore, we should expect the resulting equations to be reliable only for conditions where the atom and field are weakly coupled.

Making these factorizations leads to the semiclassical Maxwell-Bloch Equations [33, 37], which describe the coupled evolution of the complex field amplitude, $z = \langle\hat{a}\rangle$, the complex atomic polarization, $v = 2\langle\hat{\sigma}_-\rangle$, and the real-valued atomic population

difference $m = \langle \hat{\sigma}_z \rangle$:

$$\dot{z} = -(\kappa + i\Theta)z + g_0 v/2 + \mathcal{E}$$
$$\dot{v} = -(\gamma_\perp + i\Delta)v + 2g_0 z m \qquad (2.40)$$
$$\dot{m} = -2\gamma_\perp(m+1) - g_0(z^* v + z v^*) \ .$$

Note that $|v| \leq 1$ and $-1 \leq m \leq 1$.

The utility of the coupled equations 2.40 lies primarily in their relative simplicity when compared to the full master equation 2.24. For example, the analytic form for the steady-state empty cavity field,

$$z_{ss} = \frac{\mathcal{E}}{\kappa + i\Theta} \ , \qquad (2.41)$$

can be easily inferred whereas the master equation must be solved numerically for steady-state solutions. In general, the evolution given by 2.40 will differ from the true evolution 2.24, *i.e.*, z_{ss} and $\mathrm{Tr}\,[\hat{a}\hat{\rho}_{ss}]$, *etc.* This difference can be significant under strong-coupling conditions [38, 39].

2.1.3.4 The linear regime and the transmission spectrum

In the weak-driving limit [6], $\bar{n} \ll n_0$, the system can have at most one excitation, so that for all transmissive properties we may assume the atom is in the ground-state, $m_{ss} \to -1$. In fact, we must have $\langle \hat{a}\sigma_z \rangle \equiv -\langle \hat{a} \rangle$ if there is *only* one excitation allowed in the system. Therefore, the atom-field interaction will be completely linear since atomic saturation effects will be nonexistent, and we need only solve the two equations

$$\dot{z} = -(\kappa + i\Theta)z + g_0 v/2 + \mathcal{E}$$
$$\dot{v} = -(\gamma_\perp + i\Delta)v - 2g_0 z \qquad (2.42)$$

which have steady-states given by

$$z_{ss} = \frac{\gamma_\perp + i\Delta}{g_0^2 + (\kappa + i\Theta)(\gamma_\perp + i\Delta)}\mathcal{E}$$

$$v_{ss} = -\frac{2g_0}{g_0^2 + (\kappa + i\Theta)(\gamma_\perp + i\Delta)}\mathcal{E} \ . \tag{2.43}$$

Therefore, the (normalized) transmission coefficient of the coupled system is

$$\frac{z_{ss}}{\mathcal{E}/\kappa} \equiv T = \frac{\kappa(\gamma_\perp + i\Delta)}{g_0^2 + (\kappa + i\Theta)(\gamma_\perp + i\Delta)} \ . \tag{2.44}$$

Defining the fluctuations, $\delta z = z - z_{ss}$ and $\delta_v = v - v_{ss}$, the linear dynamics about steady-state are characterized by

$$\dot{\delta z} = -(\kappa + i\Theta)\delta z + g_0 \delta v/2$$

$$\dot{\delta v} = -(\gamma_\perp + i\Delta)\delta v - 2g_0\delta z \ , \tag{2.45}$$

with eigenvalues given by

$$\lambda^\pm = -\frac{1}{2}\left[(\gamma_\perp + i\Delta) + (\kappa + i\Theta) \pm \sqrt{[(\gamma_\perp + i\Delta) - (\kappa + i\Theta)]^2 - 4g_0^2}\right] \tag{2.46}$$

and rather messy eigenvectors. In the loss-less case, however, thing necessarily simplify

$$\lambda^\pm = -\frac{i}{2}\left[(\Delta + \Theta) \pm \sqrt{(\Delta - \Theta)^2 + 4g_0^2}\right]$$

$$\delta\vec{u}^\pm = \begin{bmatrix} \delta z^\pm \\ \delta v^\pm \end{bmatrix} = \begin{bmatrix} \dfrac{-i\left[\delta \mp \sqrt{\delta^2 + 4g_0^2}\right]}{\sqrt{16g_0^2 + \left[\delta \mp \sqrt{\delta^2 + 4g_0^2}\right]^2}} \\ \dfrac{4g_0}{\sqrt{16g_0^2 + \left[\delta \mp \sqrt{\delta^2 + 4g_0^2}\right]^2}} \end{bmatrix} \ . \tag{2.47}$$

The eigenvalues clearly correspond to the energies of the upper and lower dressed-states of Eq. 2.12 for $n = 1$. Most importantly, we see that the semiclassical results capture the essence of the 'vacuum'-Rabi splitting of cavity QED: for $\Delta = \Theta = 0$, the $\lambda^\pm$ eigenvalues are split by an amount $\pm ig_0$, *independent* of the drive field strength.

This normal mode splitting is often attributed to the quantum nature of field – as an indication that the field only interacts in quantized steps – but we can see here that it's present for a classical field interacting with an elastic scatterer. However, the fact that the semiclassical equations correctly predict the eigenstructure of the system should not be taken as an indication that the weakly-driven system possesses no quantum properties. For example, correlation functions (which are an indication of system *dynamics*) of the cavity transmitted field can display photon antibunching in the weak-excitation regime [9].

2.2 Optical phase bistabilty

It's well known that a cavity filled with $N \gg 1$ atoms each weakly coupled to the field, $g_0 \leq \{\kappa, \gamma_\perp\}$, and driven strongly on resonance, $\mathcal{E} \gg \{g_0, \kappa, \gamma_\perp\}$, exhibits absorptive optical bistability [37, 40, 41]. This behavior can be understood through a straightforward extension of the Maxwell-Bloch Equations for N atoms (see Chapter 3 for details) or through simpler arguments based on a saturable intracavity absorber [42]. It was also recognized early on that a single atom cavity QED system in the weak coupling regime could also exhibit signatures of absorptive bistability. Under the right conditions, steady-state photon number distributions of the master equation 2.24 are doubly peaked, with the peaks centered on mean photon numbers predicted by the semiclassical theory of optical bistability [43]. It was believed, however, that the nonlinear behavior of a single atom system would be washed away in the strong coupling regime, since the saturation photon number, $n_0 = \gamma_\perp^2 / 2g_0^2$, would be so small that the (photon number) difference between coexisting stable states would necessarily be smaller than the quantum fluctuations.

However, this does not preclude the existence of nonlinear behavior in the strong-coupling regime – it only suggests that drawing quantum analogies from the *semiclassical* picture of a saturable absorber is no longer warranted. As we'll see, a new kind of nonlinear behavior emerges from this strongly coupled quantum system. The intuition for this behavior comes from the idealized structure of the underlying quantum

model. In fact, semiclassical analogies are drawn from an idealized *quantum* picture.

2.2.1 Back to the eigenstructure

Returning to the eigenvalues 2.12 and eigenvectors 2.13 of the Hamiltonian system, but considering now the system under resonance conditions, $\Delta = \Theta = 0$, we obtain eigenstates that are balanced superpositions

$$\lim_{\delta \to 0} |\pm, n\rangle \to \frac{1}{\sqrt{2}} \left[|e, n-1\rangle \pm i \, |g, n\rangle \right], \tag{2.48}$$

with energy levels

$$E_n^\pm = \pm n g_0 \; . \tag{2.49}$$

These states and energies are represented in Figure 2.2. In a sense, the resonant case leads to the strongest coupling between the atom and cavity. For this case, the eigenvalues indicate a pronounced 'splitting' of the atom-cavity transmission spectrum under weak driving conditions: the coupled system will no longer be 'resonant' with the probe at frequency ω_0, but instead will possess two transmission peaks at $\omega_0 \pm g_0$.

As the external drive strength is increased and the system populates higher and higher dressed states the transmission spectrum will return to the case of very weak coupling. To see this note that for $n \gg 1$ the frequency difference between adjacent upper/lower dressed states goes as

$$\begin{aligned}
\epsilon_n^\pm &= E_{n+1}^\pm - E_n^\pm \\
&= \pm\sqrt{n+1} g_0 \mp \sqrt{n} g_0 \approx \pm\frac{g_0}{2\sqrt{n}}
\end{aligned} \tag{2.50}$$

and therefore tends to zero as the system is excited to higher levels. Although the steady-state transmission ostensibly approaches that of an empty cavity for $n \gg 1$ (as depicted in Figure 1.3), the laser frequency is actually detuned from the coupled system, albeit by a very small amount. This is depicted in Figure 2.3 with the probe frequency slightly red detuned relative to the upper eigenstate transition, and slightly
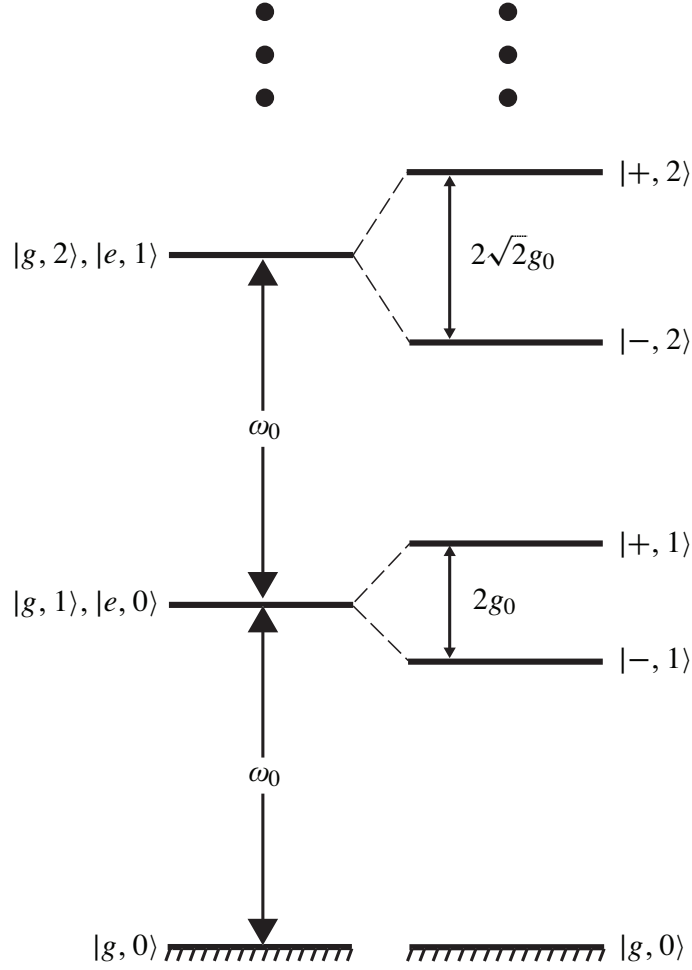
Figure 2.2: The eigenstructure (in the lab frame) of the Jaynes-Cummings Hamiltonian for the resonant case.

blue detuned from the lower. Note, though, that the detuning between the lower and upper eigenstates is quite large

$$
\begin{aligned}
\zeta_n^{\pm} &= E_{n+1}^{\pm} - E_n^{\mp} \\
&= \pm\sqrt{n+1}g_0 \pm \sqrt{n}g_0 \approx \pm 2\sqrt{n}g_0 \; ,
\end{aligned}
\tag{2.51}
$$

so that the lower and upper eigenstates can not couple to each other through the driving laser.
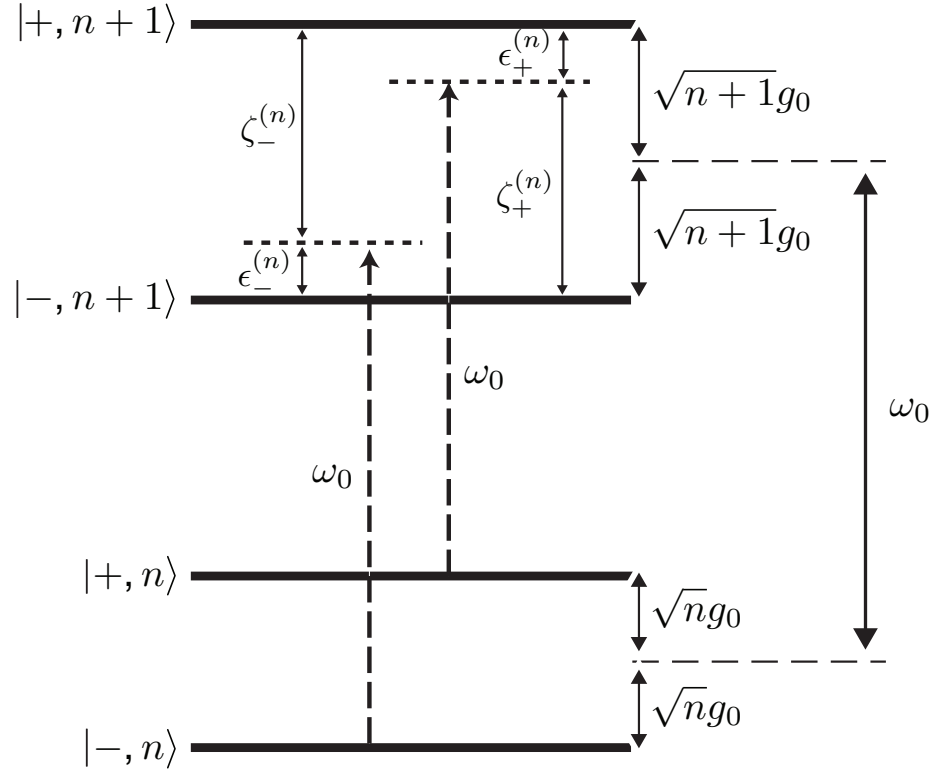
Figure 2.3: Transition detunings for phase bistability in the resonant case.

2.2.2 Everyone's favorite analogy

If we assume, for the time being, that the system localizes on either the upper or lower manifold of eigenstates, then in the limit of strong driving the field behavior should follow that of a damped harmonic oscillator being driven off resonance by a manifold dependent detuning. For very large mean photon numbers, we can neglect the variation of the detuning 2.50 with n, and take $\epsilon_n^\pm \to \pm g_0/2\sqrt{\bar{n}}$, where $\bar{n}$ is the mean intracavity photon number. The coherent state amplitude of this quantum harmonic oscillator satisfys [33, 35]

$$\dot{\alpha}^\pm = -\left(\kappa \pm \frac{ig_0}{2|\alpha^\pm|}\right)\alpha^\pm + \mathcal{E}, \tag{2.52}$$

where we have used the fact that for coherent states $\sqrt{\bar{n}^{\pm}} = |\alpha^{\pm}|$. Solving for the steady-states, we easily obtain the magnitude

$$|\alpha_{ss}^{\pm}| = \frac{\mathcal{E}}{\kappa}\sqrt{1 - \left(\frac{g_0}{2\mathcal{E}}\right)^2} , \qquad (2.53)$$

which can be re-substituted into Eq. 2.52 to yield

$$\alpha_{ss}^{\pm} = \frac{\mathcal{E}}{\kappa}\left[1 - \left(\frac{g_0}{2\mathcal{E}}\right)^2\right] \pm \frac{ig_0}{2\kappa}\sqrt{1 - \left(\frac{g_0}{2\mathcal{E}}\right)^2} . \qquad (2.54)$$

Evidently, then, for a sufficiently strong drive this driven, damped oscillator has two steady-state field amplitudes of equal magnitude but with an imaginary component that varies as $\approx \pm g_0/2\kappa$. However, these solutions only exist for $\mathcal{E} \geq g_0/2$, since the field magnitude given by Eq. 2.53 must be real valued. We might assume then, that this field strength is like a threshold for some qualitative change in the systems steady-state and dynamical behavior (although we should be be careful drawing conclusions from such an *ad hoc* model.)

So far we have ignored spontaneous emission completely. In its presence the oscillator states 2.54 will no longer be steady-states since the upper and lower dressed-state manifolds are now coupled. However, as we'll see, direct numerical integration of the master equation supports the interpretations of this section, and under the right conditions the steady-state of the full quantum mechanical treatment is roughly that of an incoherent mixture of these two coherent states

$$\hat{\rho}_{ss}^{f} \propto \frac{1}{2}\left(|\alpha_{ss}^{-}\rangle\langle\alpha_{ss}^{-}| + |\alpha_{ss}^{+}\rangle\langle\alpha_{ss}^{+}|\right) . \qquad (2.55)$$

2.2.3 Steady-state solutions to the master equation

The most direct way to compare steady-state results of the master equation with the harmonic oscillator analogy of the previous section is through the Q-function [33, 35]. The benefits of using the Q-function, over the other common quasi-probability distributions, are twofold. Firstly, the Q-function is positive-semidefinite, and is
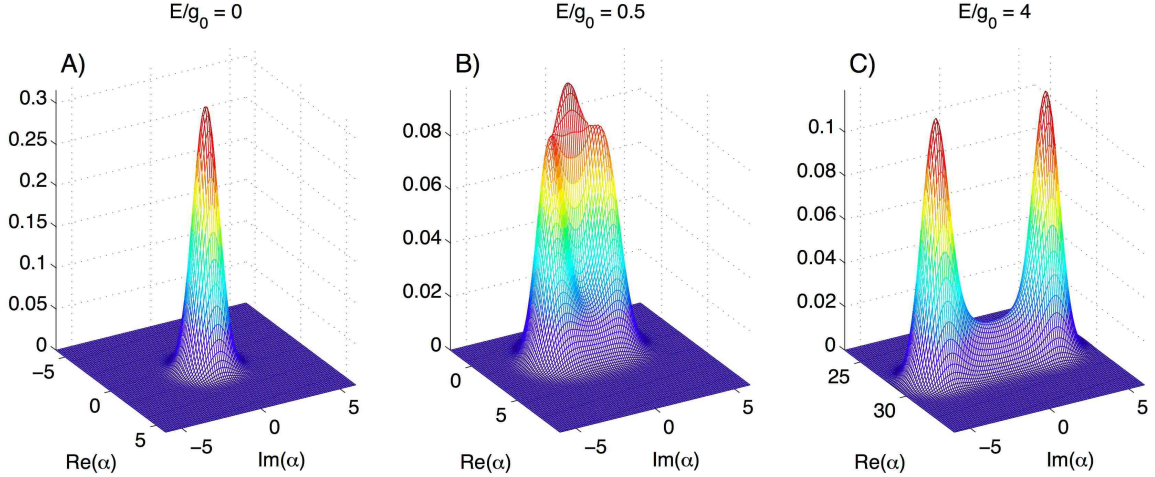
Figure 2.4: Steady-state Q-functions vs. $\mathcal{E}$ for an idealized parameter set: $g_0/\kappa \approx 7.3, \kappa/\gamma_\perp \approx 3.2$. The value of the drive term is A) $\mathcal{E} = 0$; B) $\mathcal{E} = g_0/2$; C) $\mathcal{E} = 4g_0$. Note, the imaginary axis is fixed for all three plots, and the peak positions in C) are at roughly $\text{Im}\,[\alpha] = \pm g_0/2\kappa \approx \pm 3.7$.

therefore better suited for making comparisons to classical probability distributions (such as the stationary distribution of a classical model with noise). Secondly, the value of the Q-function has a simple interpretation in terms of coherent states $|\alpha\rangle$ of the intracavity field. For any given density operator $\hat{\rho}$ we have

$$Q(\alpha) = \langle\alpha|\hat{\rho}^f|\alpha\rangle \ , \tag{2.56}$$

where $\hat{\rho}^f$ is the reduce density matrix on the field. Therefore, $Q(\alpha)$ may strictly be thought of as a probability, which further lends to its utility for making comparisons between quantum and semiclassical descriptions of equilibrium behavior.

In practice we can find the steady-state density operator ρ_{ss} of the master equation 2.24 simply by setting the terms on its right-hand side to zero and solving the resulting algebraic equation. We can then use $Q_{ss}(\alpha) = \langle\alpha|\hat{\rho}_{ss}^f|\alpha\rangle$ to visualize the results.

In Figure 2.4 we plot this Q-funcion for an ideal set of parameters that exhibit a pronounced bimodal distribution. The real and imaginary axis are, respectively, the real and imaginary components of the coherent state amplitude (*i.e.*, the amplitude

and phase quadratures):

$$\mathrm{Re}\,[\alpha] = \frac{1}{2} \left\langle \hat{a}^\dagger + \hat{a} \right\rangle \ ,$$
$$\mathrm{Im}\,[\alpha] = \frac{i}{2} \left\langle \hat{a}^\dagger - \hat{a} \right\rangle \ . \tag{2.57}$$

For each plot, the real and imaginary axes are centered on the expected empty cavity mean field, $\mathrm{Re}\,[\alpha] = \mathcal{E}/\kappa$. For small drive strengths the steady-state field distribution is essentially normal, as expected in the vacuum state, but with a slight broadening due to atomic scattering. However, as the drive field is increased through the predicted threshold, $\mathcal{E} = g_0/2$, the distribution begins to noticeably deviate from normal, and in the very strong driving regime two peaks are clearly visible. Note that in the absence of an atom-field interaction, the normal distribution seen in Figure 2.4A will simply shift along $\mathrm{Re}\,[\alpha]$ as the drive strength is increased.

I won't waste a bunch of space here plotting up Q-funcitons for every conceivable parameter set. Suffice it to say [3] that the agreement between the steady-state Q-functions and the harmonic oscillator picture of the previous section is excellent. In particular, for large drive strengths the peak splitting in phase goes as $\pm g_0/2\kappa$, and in the limit $g_0 \gg 2\kappa$ the drive field $\mathcal{E} = g_0/2$ sets a threshold for this bimodal display. Also, in Figure 2.4B it's clear that the steady-state distribution is 'lagging' significantly behind the empty cavity field value (at the center of the plot). We can understand this behavior easily from the Jaynes-Cummings structure for low excitations displayed in Figure 2.2 – the nominally resonant drive is off resonant from the coupled atom-cavity system by $\sim \pm g_0$, so that the cavity steady-state field amplitude is largely suppressed. With persistence, though, the drive will populate higher and higher rungs of the ladder, until at the critical value of $g_0/2$ the larger n states are sufficiently populated to allow for the near resonant pathways $|-, n-1\rangle \rightarrow |-, n\rangle \rightarrow |-, n+1\rangle$ and $|+, n-1\rangle \rightarrow |+, n\rangle \rightarrow |+, n+1\rangle$ to overwhelm the system with photons.

As alluded to at the end of Section 2.2.2, in the strong driving limit spontaneous emission couples the upper and lower eigenstate manifolds. Since the states $|\pm, n\rangle$ are

comprised of an equal mixture of atomic excited and ground states, we should expect that their spontaneous emission rate to be $\gamma_\perp$. For each emission event the initial state is knocked down by one excitation, but the resulting manifold will be random

$$
|\pm, n\rangle \rightsquigarrow \left\{ \begin{array}{l} |\pm, n-1\rangle \\[2mm] |\mp, n-1\rangle \end{array} \right. \tag{2.58}
$$

so that the effective rate of 'mixing' is $\gamma_\perp/2$. We can expect, then, that this bimodal field behavior to persist for finite $\gamma_\perp$, but with the individual peaks less distinguishable. In fact, this is the case – for example, the 'skirt' connecting the two peaks in Figure 2.4 is a consequence of a finite $\gamma_\perp$. As it turns out, the critical parameter that determines how distinct the two peaks appear is the ratio $\gamma_\perp/2\kappa$. But to understand this fact we need to move beyond steady-state Q-functions.

2.2.4   A (slightly) better semiclassical model

The semiclassical equations 2.40 don't predict the bimodal phase behavior shown in Figure 2.4. The resonant Maxwell-Bloch equations

$$
\begin{aligned}
\dot{z} &= -\kappa z + g_0 v/2 + \mathcal{E} \;, \\
\dot{v} &= -\gamma_\perp v + 2g_0 z m \;, \\
\dot{m} &= -2\gamma_\perp (m+1) - g_0(z^* v + z v^*) \;,
\end{aligned} \tag{2.59}
$$

have steady-states that satisfy

$$
\begin{aligned}
v_{ss} &= (2g_0/\gamma_\perp)\, z_{ss} m_{ss} \;, \\
m_{ss} &= -\frac{1}{1 + (2g_0^2/\gamma_\perp^2)\,|z_{ss}|^2} \;,
\end{aligned} \tag{2.60}
$$

and

$$
\mathcal{E}/\kappa = |z_{ss}| + \frac{(g_0^2/\gamma_\perp \kappa)\,|z_{ss}|}{1 + (2g_0^2/\gamma_\perp^2)\,|z_{ss}|^2} \;. \tag{2.61}
$$

If we take the limit $\gamma_\perp/\kappa \to 0$, these solutions exhibit absorptive bistability for small drive values, and for $\mathcal{E} \gg g_0/2$ there is only a single solution of the form

$$z_{ss} = \mathcal{E}/\kappa , \quad v_{ss} = 0 , \quad m_{ss} = 0 . \tag{2.62}$$

This corresponds to the cavity field overwhelming the atom into a completely unpolarized state; at this point, the intracavity field may respond to the drive as though there is no atom.

It shouldn't be too surprising that Eq. 2.62 fails to capture the behavior of the previous section, since the approximations leading to 2.59 are invalid under strong coupling. But still, if the arguments presented in Section 2.2.2 are correct, and the master equation seems to think they are, then the system state is essentially jumping between the two *separable* states $|+\rangle \otimes |\alpha^+\rangle$ and $|-\rangle \otimes |\alpha^-\rangle$, where

$$|\pm\rangle = \frac{1}{\sqrt{2}} \left(|e\rangle \pm i|g\rangle \right) , \tag{2.63}$$

are the semiclassical atomic dressed states. In this case, the operator factorizations made in Section 2.1.3.3 that lead to Eq. 2.59 are not so inappropriate. And yet, the Maxwell-Bloch equations are oblivious to this bimodal phase behavior.

Well maybe the Maxwell-Bloch equations are smarter than we (meaning I) think. The key problem is that the atomic steady-state in Eq. 2.62 is completely unpolarized. Of course, this *is* the steady-state mean we should expect if the underlying dynamics describe an atomic states randomly jumping between orthogonally polarized states. The problem is, once again, that pesky parameter $\gamma_\perp$, which tends to depolarize the atomic state even if we take $\gamma_\perp \to 0$ after solving for the steady-state. Instead, let's just force the atomic state to be polarized by setting $\gamma_\perp = 0$ *before* solving for the steady-states. In this case, we have the conservation law $|v_{ss}|^2 + m_{ss}^2 = 1$ to add to

the steady-state equations

$$\mathcal{E}/\kappa + (g_0/2\kappa)v_{ss} = z_{ss} \ ,$$

$$z_{ss}m_{ss} = 0 \ , \qquad (2.64)$$

$$z_{ss}^*v_{ss} + z_{ss}v_{ss}^* = 0 \ .$$

The solutions valid for $\mathcal{E} \le g/2$ are:

$$z_{ss} = 0 \ ,$$

$$v_{ss} = -2\mathcal{E}/g_0 \ , \qquad (2.65)$$

$$m_{ss} = \pm\sqrt{1 - (2\mathcal{E}/g_0)^2} \ ,$$

which correspond to an atom polarized just so that it's radiated field exactly cancels the drive field. Of course, the atom can not do this indefinitely, and for $\mathcal{E} \ge g/2$ the solutions become

$$z_{ss} = (\mathcal{E}/\kappa)[1 - (g_0/2\mathcal{E})^2] \pm i(g_0/2\kappa)\sqrt{1 - (g_0/2\mathcal{E})^2} \ ,$$

$$v_{ss} = -(g_0/2\mathcal{E}) \pm i\sqrt{1 - (g_0/2\mathcal{E})^2} \ , \qquad (2.66)$$

$$m_{ss} = 0 \ .$$

These states exhibit the bistability that we were looking for. The important thing about Eqs. 2.65-2.66 is that they accurately predict: (i) that the field is zero when the driving is weak; (ii) that there exists a threshold driving strength, $\mathcal{E} = g/2$, for the interesting things to happen; (iii) that phase bistability occurs for strong driving; and (iv) the optical phase is correlated with the atomic dipole orientation. In the limit of very strong driving, $\mathcal{E} \gg g$, the steady-states in Eq. 2.66 simplify further to:

$$z_{ss} = (\mathcal{E}/\kappa) \pm i(g/2\kappa) \ ,$$

$$v_{ss} = \mp i \ , \qquad (2.67)$$

$$m_{ss} = 0 \ .$$

These states are the classical analogs to the quantum tensor product of a optical

coherent state with an atomic dressed state. Physically, these states correspond to the atomic dipole either aligned or anti-aligned with the resonant drive field; the steady-state field thus contains a quadrature component corresponding to the field radiated by the atomic dipole, $g_0 v_{ss}/2$ in 2.59.

2.2.5 Quantum trajectory simulations

The dynamics obtained from direct numerical integration of the master equation 2.24 display nothing like the behavior outlined in Section 2.2.2. In Figure 2.5 this time evolution is presented for the parameters of Figure 2.4C, where the Q-function has a pronounce phase splitting. In Figure 2.5A we plot the phase, $\text{Tr}[\hat{Y}\hat{\rho}]$, and amplitude, $\text{Tr}[\hat{X}\hat{\rho}]$, quadratures of the intracavity field over a time $1/\gamma_\perp$, where

$$\hat{Y} = \frac{i}{2}(\hat{a}^\dagger - \hat{a}) \ , \tag{2.68}$$

and

$$\hat{X} = \frac{1}{2}(\hat{a}^\dagger + \hat{a}) \ . \tag{2.69}$$

The initial condition is the steady-state of an uncoupled atom and cavity: $|g\rangle \otimes |\mathcal{E}/\kappa\rangle$. Note that the plotted amplitude quadrature has the value $\mathcal{E}/\kappa$ subtracted so that it can be displayed in the same scale as the phase quadrature. Clearly there's nothing interesting going on here, except for a modest ripple in the amplitude quadrature a early times. The phase quadrature, however, is exactly zero (within simulation error). In Figure 2.5B we plot the evolution of the dressed states $\text{Tr}[|\pm\rangle\langle\pm|\hat{\rho}]$. Aside from an early time Rabi oscillation at frequency $\Omega_r \approx \sqrt{\bar{n}}g_0/2$, the dressed state populations decay into nearly unpolarized states. This behavior is exactly what our initial Maxwell-Bloch steady-states predicted 2.62.

From the intuitive harmonic oscillator picture of Section 2.2.2 we would expect the phase quadrature and atomic dressed states switch between the two values of Eq. 2.67, with the switching triggered by individual spontaneous emission events. We clearly don't see this. The thing is, the master equation 2.24 would never produce
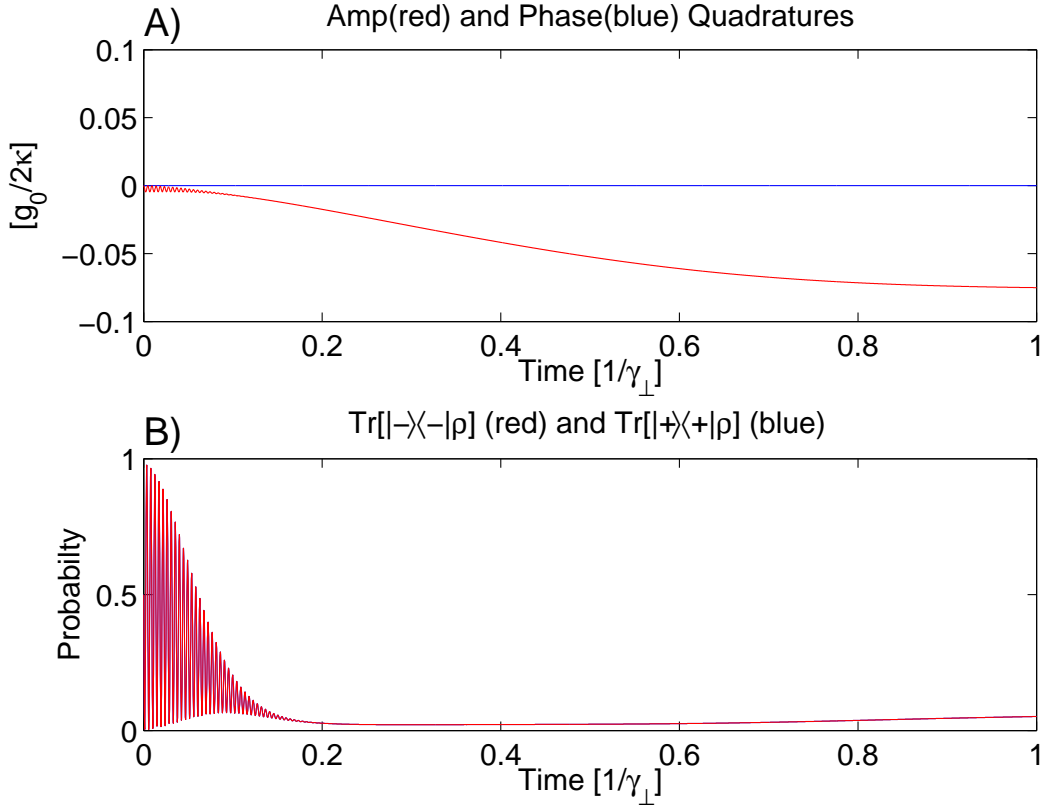
Figure 2.5: Solution to numerical integration of the unconditional master equation for parameters of Figure 2.4B. A) Expectation values of the amplitude $(\hat{a}^\dagger + \hat{a})/2$ and phase $i(\hat{a}^\dagger - \hat{a})/2$ quadratures – note, to display on the same scale the amplitude quadrature has its $t = 0$ value subtracted off. B) Probability of being in the upper and lower dressed states. Note, the two curves lie on top of each other.

this sort of behavior – as it's just a finite set of linear differential equations, the most we can expect is a bunch of damped sinusoids, which is essentially what we see. Of course, the behavior that leads to the Q-functions 2.4 is in there somewhere – we just need a way of coaxing it out. Now we could attempt to reconstruct this behavior by computing the time evolution of higher and higher moments of system operators [44], but I find this approach is cumbersome and quite unsatisfying.

The problem is that the master equation 2.24 describes the *unconditional* dynamics of the atom-cavity system. That is, the solutions $\hat{\rho}(t)$ of the master equation represent the knowledge we can have of the evolving system state without utilizing information obtainable via real-time measurements of the output fields (*i.e.*, cavity
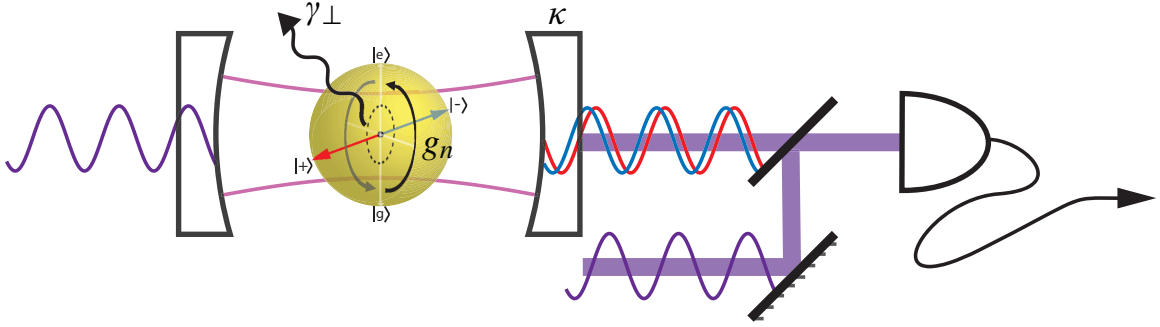
Figure 2.6: A schematic of a cavity QED system with homodyne measurement of the phase quadrature. In a parameter regime exhibiting phase bistability, the detected phase of the output field is correlated with the atomic dressed state.

transmission and atomic fluorescence). Therefore, we can gain further insight into the dynamics by considering quantum predictions regarding detection photocurrents. Fortunately, the same theory used to derive the master equation provides a powerful set of tools for a statistically-faithful sampling of continuous measurement records [6, 45, 46], and tells us how to interpret them as real-time observations of the intracavity dynamics [47]. In what follows I'll make use of these 'quantum trajectory' methods for Monte Carlo simulations of the photocurrent generated by homodyne detection of the cavity output field [45].

2.2.5.1 The stochastic Schrödinger equation

One possible, and in this case relevant, measurement scheme is homodyne detection, depicted in Figure 2.6. The cavity output field (the 'signal') is interfered with a coherent field (the 'local oscillator'), and the total intensity of these summed fields is measured by a standard photodetector. By varying the relative phase, θ, of the local oscillator field we may exact a measurement of the cavity field operator (see Section 2.3.5)

$$\hat{X}_\theta = \frac{1}{2} \left(e^{i\theta}\hat{a}^\dagger + e^{-i\theta}\hat{a} \right) \ . \tag{2.70}$$

For the moment I'll pretend as though there is no spontaneous emission just to simplify the equations. Then, in the limit of a very intense local oscillator, the stochastic Schrödinger equation (SSE) governing the evolution of the conditional state vector,

$|\psi_c\rangle$, is given by [48]

$$d|\psi_c\rangle = \left(-i\hat{H} - \kappa\hat{a}^\dagger\hat{a} + 2\kappa e^{-i\theta}\hat{a}\langle\hat{X}_\theta\rangle_c - \kappa\langle\hat{X}_\theta\rangle_c^2\right)|\psi_c\rangle dt+$$
$$+ \sqrt{2\kappa}\left(e^{-i\theta}\hat{a} - \langle\hat{X}_\theta\rangle_c\right)|\psi_c\rangle dW \ , \tag{2.71}$$

where dW is a Wiener increment [49] satisfying $\langle dW\rangle = 0$ and $\langle dW^2\rangle = dt$, and $\langle\cdot\rangle_c$ denotes the conditional expectation. I include this particular case here for posterity, since in many places [20, 50] the SSE for homodyne detection is written in an unnormalized form (which is fine), or even flat out incorrectly [35] (which is not fine). Of course, van Handel [48] gets it *just right* [51], and in particular the form 2.71 correctly reproduces the normalized stochastic master equation [45]

$$d\hat{\rho}_{tot} = d\left(|\psi_c\rangle\langle\psi_c|\right)$$
$$= d\hat{\rho} + d\hat{\rho}_{meas} \ , \tag{2.72}$$

where $d\hat{\rho}$ is just the increment from the unconditional master equation 2.24 and the measurement term is

$$d\hat{\rho}_{meas} = \sqrt{2\kappa}\left(e^{-i\theta}a\hat{\rho} + \hat{\rho}e^{i\theta}a^\dagger - 2\mathrm{Tr}[\hat{X}_\theta\hat{\rho}]\hat{\rho}\right)dW \ . \tag{2.73}$$

Incorporating the measurement of atomic spontaneous emission into the SSE leads to (after the obvious extension of 2.71),

$$\begin{aligned}
d|\psi_c\rangle = &-i\hat{H}|\psi_c\rangle dt \\
&+ \left(-\kappa\hat{a}^\dagger\hat{a} + 2\kappa e^{-i\theta_1}\hat{a}\langle\hat{X}_{\theta_1}\rangle_c - \kappa\langle\hat{X}_{\theta_1}\rangle_c^2\right)|\psi_c\rangle dt \\
&+ \sqrt{2\kappa}\left(e^{-i\theta_1}\hat{a} - \langle\hat{X}_{\theta_1}\rangle_c\right)|\psi_c\rangle dW_1 \\
&+ \left(-\gamma_\perp\hat{\sigma}_+\hat{\sigma}_- + 2\gamma_\perp e^{-i\theta_2}\hat{\sigma}_-\langle\hat{S}_{\theta_2}\rangle_c - \gamma_\perp\langle\hat{S}_{\theta_2}\rangle_c^2\right)|\psi_c\rangle dt \\
&+ \sqrt{2\gamma_\perp}\left(e^{-i\theta_2}\hat{\sigma}_- - \langle\hat{S}_{\theta_2}\rangle_c\right)|\psi_c\rangle dW_2 \ ,
\end{aligned} \tag{2.74}$$

with the Hamiltonian, $\hat{H}$, given in Eq. 2.5, and $\hat{S}_{\theta_2} = (e^{-i\theta_2}\hat{\sigma}_- + e^{i\theta_2}\hat{\sigma}_+)/2$. The measured homodyne photocurrents, $I_{hom_{1,2}} = \frac{dQ_{1,2}}{dt}$, which are, respectively, the ho-

modyne photocurrents associated with the cavity and atomic decay channels, can
then be calculated using

$$
\begin{aligned}
dQ_1 &= \sqrt{2\kappa\eta_\kappa}\left\langle 2\hat{X}_{\theta_1}\right\rangle dt + dW_1' \;, \\
dQ_2 &= \sqrt{2\gamma_\perp\eta_{\gamma_\perp}}\left\langle 2\hat{S}_{\theta_2}\right\rangle dt + dW_2' \;,
\end{aligned}
\tag{2.75}
$$

where $\left(dW_{1,2}, dW_{1,2}'\right)$ are independent Wiener increments, and $(\eta_\kappa, \eta_{\gamma_\perp})$ represent the
measurement efficiencies of each channel. Numerical integration of Equations 2.74
and 2.75 are performed using the stochastic integration routine incorporated in the
Quantum Optics Toolbox [52] for MATLAB.

In a real experiment, full measurement of the atomic spontaneous emission is not
actually feasible as this would require a detector covering nearly 4π steradians of
solid angle. Fortunately, the cavity-output homodyne photocurrent I_{hom_1} generated
by Monte Carlo integration of the above SSE (considered on its own without any ref-
erence to the corresponding I_{hom_2}) is sampled from the same law as the photocurrent
one would see in an experiment in which the atomic decay channel was not measured
at all [48]. Therefore I make use of such photocurrent simulations below and also in
Chapter 3 in the analysis of single-atom bistability and Hopf bifurcations.

It should be stressed that the conditional state $|\psi_c\rangle$ propagated by the SSE is
merely an internal variable of the Monte Carlo simulation, and not something that
could be reconstructed (in a recursive estimation sense) from the cavity-output pho-
tocurrent alone. The best we could do to estimate the system's state, without assum-
ing high-efficiency observation of the cavity decay channel, would be to utilize the
corresponding stochastic master equation [45] as an optimal quantum filter [47]. Even
in a purely theoretical discussion it's best to utilize the SME (as in Ref. [28]) to gener-
ate not only realistic photocurrent samples, but also the conditional quantum states
that one could in principle generate from them via recursive filtering. Unfortunately
such numerical procedures are very computationally intensive, which motivates the
use of the SSE here. In the remainder of this section I will plot conditional expecta-
tions as well as photocurrents, but this is primarily just to 'guide the eye' and verify
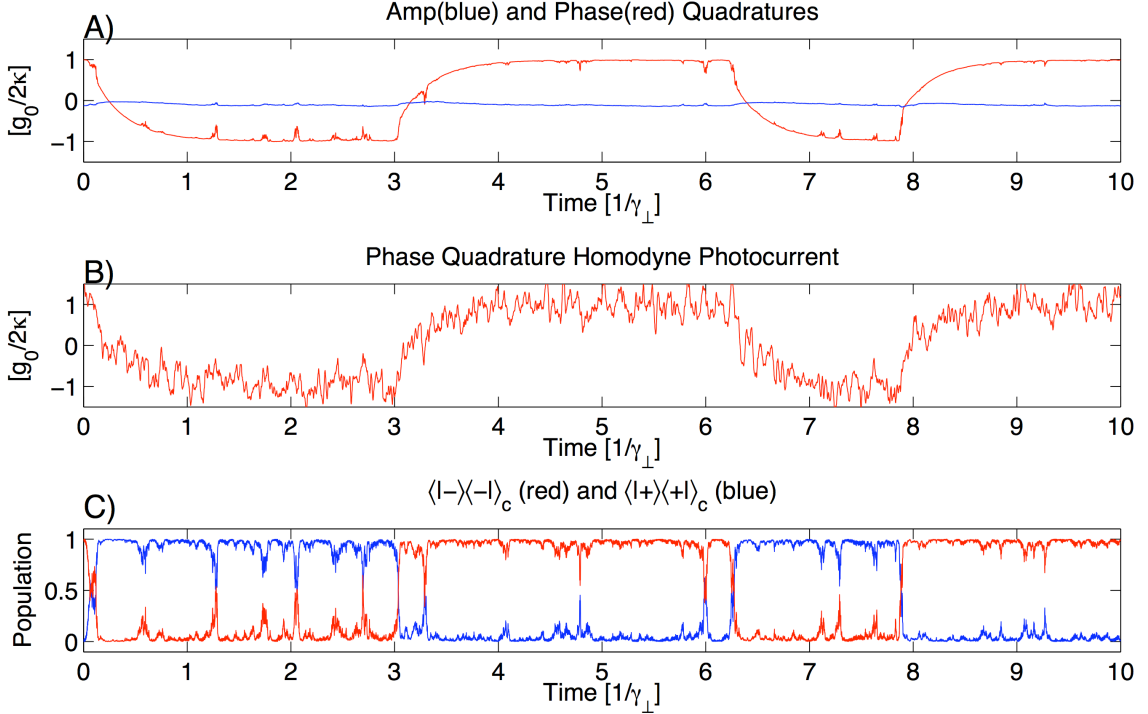
Figure 2.7: Quantum trajectory simulation for parameters of Figure 2.4B. A) The conditional amplitude(blue) and phase(red) quadratures of the field. Note that the amplitude quadrature has $\mathcal{E}/\kappa$ subtracted off to display on the same scale. B) Photocurrent generated from phase quadrature homodyne measurement of the cavity field assuming perfect detection efficiency. Photocurrent is displayed at an analog bandwidth, $f_{bw} = 5\kappa$. C) Probability of being in the $|-\rangle\langle-|$ (red) and $|+\rangle\langle+|$ (blue) atomic dressed states.

the intuition of Section 2.2.2. As we'll see here the dynamics underlying the bimodal Q-functions are generally well represented by the photocurrents alone.

2.2.5.2 Numerical results

The variations in photocurrent, for the case of phase bistability, are best captured by setting the measurement phase so that $\hat{X}_{\pi/2} = \hat{Y}$, where $\hat{Y}$ the phase quadrature field operator of Eq. 2.68. The results of a quantum trajectory simulation, in this case, for the parameters of Figure 2.4 are plotted in Figure 2.7. The simulated homodyne photocurrent in Figure 2.7B shows a clear hopping between two states separated by $\pm g_0/2\kappa$. Note, as will be the norm throughout the remainder of this thesis, the

displayed photocurrent, I_{disp}, is scaled so

$$I_{disp} = \frac{I_{hom}}{2\sqrt{2\kappa\eta_\kappa}} \frac{1}{g_0/2\kappa} \ , \tag{2.76}$$

and should therefore jump between the values ± 1 in the ideal case. Within the plotted time window we see four distinct switching events, consistent with the picture of spontaneous emission induced jumping between atomic dressed states[3]. And from extended simulations, we find that the the average rate of switching between the upper and lower field states is indeed $\gamma_\perp/2$. Furthermore, we see that the phase quadrature field switching displayed in 2.7A) is generally preceded by the atomic state jumps between the upper $|+\rangle$ and lower $|-\rangle$ dressed states in 2.7C). Comparing A) and C) it's immediately clear why the ratio $\gamma_\perp/2\kappa$ serves such an important role in the 'distinguishability' of the Q-function peaks: for every spontaneous emission induced atomic jump between dressed state manifolds, the cavity field needs at least a time $\tau \sim 1/\kappa$ to respond. That is, the intracavity field can not respond instantaneously; in general, it can only change as $\sim e^{-\kappa t}$. If the jumping rate $\gamma_\perp/2$ becomes faster than κ, the intracavity phase quadrature will not have enough time to fully switch between the values, $\pm g_0/2\kappa$. The steady state distribution will become smeared, reflecting the smaller fraction of time spent at the fixed points 2.66.

So far we've looked at an idealized set of parameters. In Figure 2.8 and 2.9 we plot the Q-function and quantum trajectory simulation, respectively, for an experimentally relevant parameter set, $\{g_0, \kappa, \gamma_\perp\}/2\pi = \{22, 8.0, 2.6\}$MHz. The values correspond to the maximal coupling strength for a Cesium atom interacting with circularly polarized light within the cavity described in Section 2.3.1. Note that in comparison to the 'ideal' values, this 'realistic' parameter set has the same ratio $\kappa/\gamma_\perp$, but the ratio g_0/κ is about three times smaller. The threshold behavior 2.8B is now not nearly as pronounced is in the ideal case 2.4B, nor is the high field splitting 2.8C, although two peaks can still be easily distinguished by eye. These peaks can also be distinguished quite easily in the simulated photocurrent presented in Figure 2.9B. Note, this simulated signal is displayed at the same bandwidth as that of Figure 2.7B, $f_{bw} = 5\kappa$, and
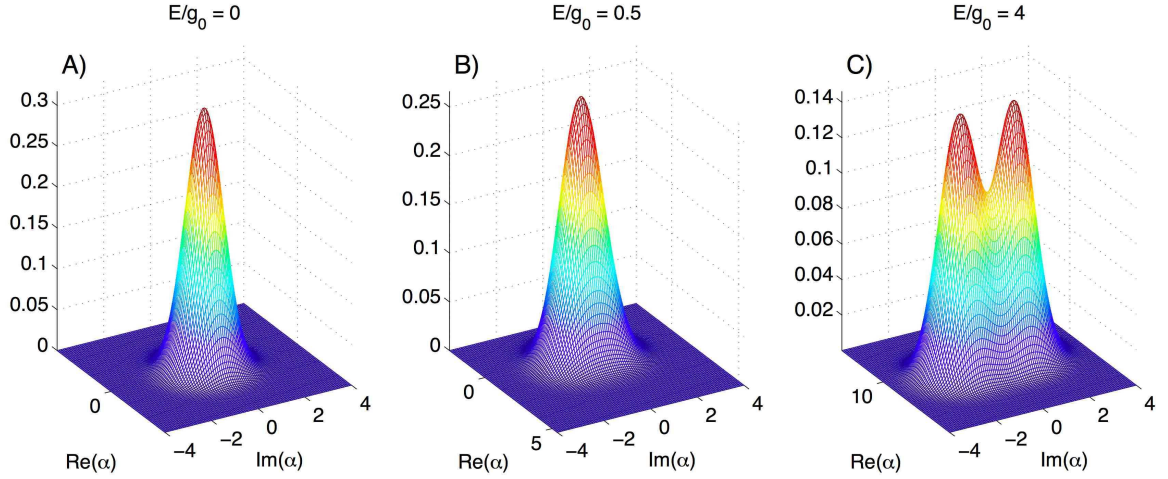
Figure 2.8: Steady-state Q function expected for the experimental parameters of Section 2.3. Parameters are $g_0/\kappa \approx 2.7$, $\kappa/\gamma_\perp \approx 3.2$, and the value of the drive term is A) $\mathcal{E} = 0$; B) $\mathcal{E} = g_0/2$; C) $\mathcal{E} = 4g_0$.

again with perfect detection efficiency. The smaller value of $g_0/2\kappa$ for these parameter means that the photocurrent signal appears more 'noisy'. That is, the conditional expectation term in the simulated photocurrent 2.75 now jumps between smaller field values, but the Wiener process remains unchanged.
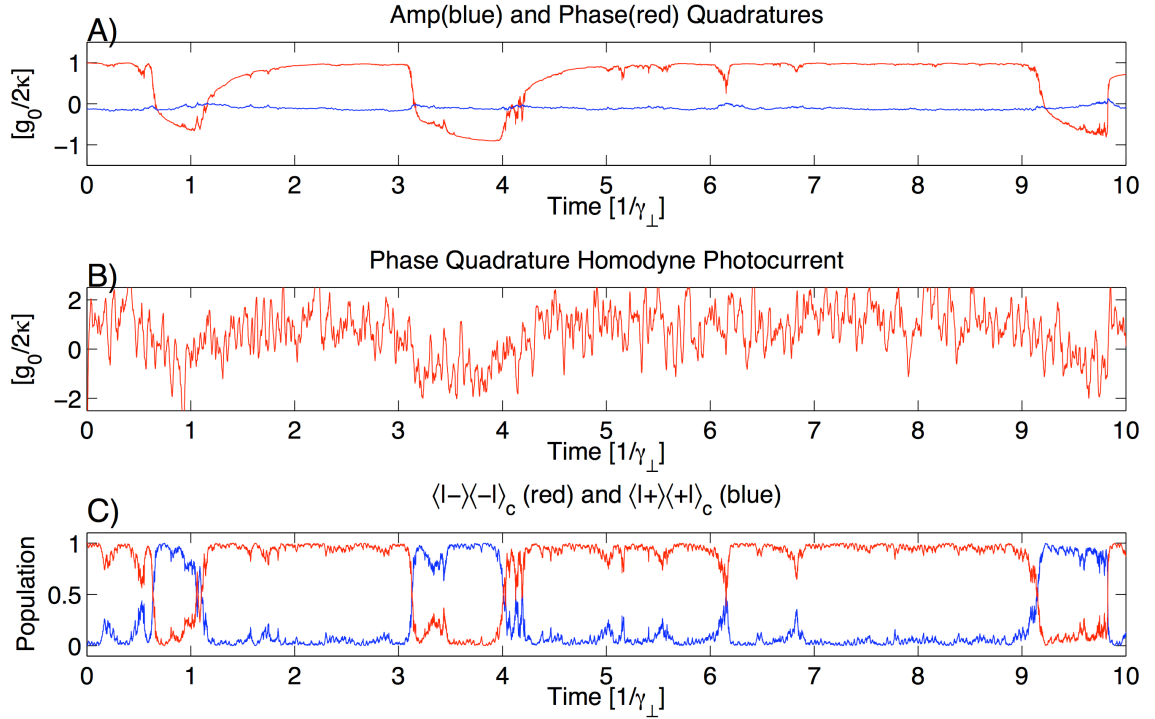
Figure 2.9: Quantum trajectory simulation for the expected experimental parameters of Section 2.3 and the driving field used in Figure 2.8C. A) The conditional amplitude(blue) and phase(red) quadratures of the field. Note that the amplitude quadrature has $\mathcal{E}/\kappa$ subtracted off to display on the same scale. B) Photocurrent generated from phase quadrature homodyne measurement of the cavity field assuming perfect detection efficiency. Photocurrent is displayed at an analog bandwidth, $f_{bw} = 5\kappa$. C) Probability of being in the $|-\rangle\langle-|$ (red) and $|+\rangle\langle+|$ (blue) atomic dressed states.

2.3 The experiment

The experimental procedure is conceptually quite straightforward. Within a vacuum chamber, a cold cloud of Cesium atoms is dropped onto a high finesse optical cavity about $\sim$ 8mm below. When a weak off-resonant probe, monitored through optical heterodyne detection, senses the presence of an atom, an electronic switch turns on an intense resonant drive. A homodyne measurement of the cavity's transmitted signal is digitized and stored for post processing.

2.3.1 The cavity

I'll begin by describing the single most important experimental component whose properties we have direct control over: the cavity. It was constructed, somewhat hastily, using what mirrors were lying around. Consequently, the cavity QED parameters that were obtained are somewhat marginal for a real-time demonstration of phase bistability, and are certainly short of state-of-the-art [53, 54].

2.3.1.1 The cavity QED parameters

When properly constructed, a Fabry-Perot cavity comprised of two spherical mirrors separated by a length l will support a fundamental TEM_{00} Gaussian mode of volume [34]

$$V_m = \frac{\pi}{4} w_0^2 l \tag{2.77}$$

where w_0 is the Gaussian waist of the mode. For mirrors of radius of curvature R_1 and R_2, this waist can be expressed as

$$w_0^2 = \frac{\lambda}{\pi l} \sqrt{\frac{h_1 h_2 (1 - h_1 h_2)}{(h_1 + h_2 - 2 h_1 h_2)^2}} \tag{2.78}$$

where $\lambda = 2\pi c / \omega$ is the wavelength of the light, and the h_i's above are given by

$$h_i = 1 - \frac{l}{R_i} \ . \tag{2.79}$$

This notation is different from that of Siegman [34] who denotes my h's using the variable g, as is customary in the laser physics community. For obvious reasons I choose not to do that here, and the reader is left with but a minor inconvenience. Provided that these parameters are well known, the atom-field coupling strength g_0 may be easily computed from

$$g_0 = d\sqrt{\frac{\hbar\omega}{2\epsilon_0 V_m}} \; , \tag{2.80}$$

where d is the dipole moment for the atomic transition in question.

Estimation of the cavity decay rate, κ, is rather straightforward through knowledge of the cavity linewidth, δf, defined, here, as the full width at half max for the intensity. The cavity field decay rate is computed from $\kappa = (2\pi \cdot \delta f)/2$. As additional knowledge of the cavity properties are required for proper calibration of the 'interesting' signals to be measured, I'll spend a moment discussing some key concepts and parameters. In particular, we'll need an estimate of each mirror's field reflectivity, r_i, as well as it's total absorptive and scattering losses (for intensity), A_i. As modern mirror coating and polishing techniques are quite impressive, mirrors can routinely be fabricated with $r \approx 1$, so it's generally convenient to express properties through the finesse

$$\mathcal{F} = \frac{\pi\sqrt{r_1 r_2 e^{-A_1/2}e^{-A_2/2}}}{1 - r_1 r_2 e^{-A_1/2}e^{-A_2/2}} \; , \tag{2.81}$$

which roughly measures the number of round trips a photon will make in an empty cavity before it exits. In the very high finesse limit, it's convenient to parameterize the reflectivity as, $r_i^2 = e^{-T_i}$, where T_i is the power transmission for mirror i. In this case, the finesse may be expressed as

$$\mathcal{F} = \frac{2\pi}{(T_1 + A_1) + (T_2 + A_2)} = \frac{2\pi}{L_{tot}} \; , \tag{2.82}$$

where L_{tot} is the total round trip loss. The finesse is related to the full width at half max and the cavity free spectral range, $FSR = c/2l$, through the convenient

expression

$$\mathcal{F} = \frac{FSR}{\delta f} \ . \tag{2.83}$$

For a laser incident on mirror 1, and matched to the cavity TEM_{00} mode with efficiency, ν, the ratios of reflected and transmitted powers to the incident power are [54]

$$\frac{P_r}{P_i} = (1 - \nu) + \nu \left(\frac{T_2 + A_2 + A_1 - T_1}{L_{tot}} \right)^2 \ , \tag{2.84}$$

and

$$\frac{P_t}{P_i} = \nu \frac{4T_1 T_2}{L_{tot}^2} \ . \tag{2.85}$$

Therefore, the mode matching efficiency can be eliminated from these equations by constructing the ratio

$$\frac{P_t}{P_i - P_r} = \frac{4T_1 T_2 / L_{tot}^2}{1 - [(A_1 + T_2 + A_2 - T_1)/L_{tot}]^2} \ , \tag{2.86}$$

which is quite conveniently measurable. It's not useful, however, unless we assume the cavity mirrors to be identical, so that $T_1 = T_2 = T$ and $A_1 = A_2 = A$, and the ratio reduces to

$$\frac{P_t}{P_i - P_r} = \frac{T^2}{(T + A)^2 - A^2} \ . \tag{2.87}$$

This quantity can be measured along with the finesse to determine the mirror transmission and scattering losses.

2.3.1.2 Measurements of the cavity properties

The cavity length is easy enough to determine with the aid of an optical wavemeter. On resonance, the optical wavelength must satisfy $m\lambda = 2l$, for integer m; therefore, by measuring the resonant wavelengths of adjacent axial modes, λ_1 and λ_2, we can compute[5]

$$l \approx \frac{1}{2} \frac{\lambda_1 \lambda_2}{|\lambda_1 - \lambda_2|} \ . \tag{2.88}$$

---

[5]Note, this expression is only approximate: the FSR is a "real" Fabry-Perot cavity is not constant, because light reflected off a real mirror experiences a *frequency-dependent* phase shift [34].

Using this procedure I obtained a nominal value of $l = 71.6\mu$m, implying an axial mode spacing, $FSR = 2.1$THz.

The cavity linewidth was measured by monitoring the transmitted intensity while sweeping, in time, the length of the cavity over a resonance. The sweep rate was calibrated by placing frequency sidebands on the laser, and the digitized transmission signal was fit with a Lorentzian. The obtained value was, $\delta f = 16$MHz, implying a cavity decay parameter, $\kappa = 2\pi \cdot 8$MHz, and a finesse, $\mathcal{F} = 130,000$. Assuming a symmetric cavity, this constrains the total losses to $T + A \approx 24$ppm. Since the cavity was mode matched to $> 95\%$, the mirror loss parameters were inferred through a measurement of the cavity transmission alone, Eq. 2.85. From the $\approx 20\%$ of the incident power that was measured exiting the cavity, I inferred the transmission and absorption losses to be $T \approx 10$ppm and $A \approx 14$ppm. This is quite unfortunate, as it implies that only a fraction $\eta_T \approx 0.2$ of the intracavity power makes it into the cavity output mode (*i.e.*, the mode that we measure.) It should be noted, however, that I made no attempts to characterize the optical scattering due to the (uncoated) vacuum chamber view ports, so that the quantity T is probably a bit larger than quoted above, while A is equally smaller. This fact is irrelevant, however, for determining the quantity κ. Furthermore, although η_T was estimated using only transmission measurements, subsequent analysis of the cavity reflection signal was found to be consistent with this value of η_T.

Finally, the cavity is comprised of two 25cm radius of curvature spherical mirrors; combined with the known length, this gives us a waist, $w_0 \approx 29\mu$m. Therefore, for dipole allowed transitions on the D2 manifold of Cesium 133 [55], we get a maximal atom-field coupling of $g_0 \approx 2\pi \cdot 22$MHz for circularly polarized transitions between the $(6S_{1/2}, F = 4, m_f = 4) \rightarrow (6P_{3/2}, F' = 5, m'_f = 5)$ states, or $g_0 \approx 2\pi \cdot 16$MHz for linearly polarized transitions between the $(6S_{1/2}, F = 4, m_f = 0) \rightarrow (6P_{3/2}, F' = 5, m'_f = 0)$ states.

2.3.1.3 Cavity construction and vibration isolation

In order to be useful, a high finesse optical cavity must have its length very well stabilized. If we require that the cavity's resonant frequency be stabilized to a fraction, ε, of its linewidth, then for a resonant wavelength, λ, the mirror separation must satisfy $\delta l_{rms} \leq \frac{\varepsilon \lambda/2}{\mathcal{F}}$. Making the conservative choice, $\varepsilon = 0.1$, the required RMS stability for our cavity is $\delta l_{rms} \leq 0.3$pm.

As our Fabry-Perot cavity is comprised of two macroscopic mirrors attached to a common surface, this RMS stability requirement is not intrinsically satisfied. In general, the mirror separation drifts due to low frequency thermal variations and fluctuates due to high frequency vibrations. To correct for the first problem each mirror is set atop a piezo transducer, as depicted in Figure 2.10C. The mirror itself rests within an aluminum mount which has been carefully machined such that its radius of curvature is ever-so smaller than that of the mirror; the mirror rests firmly within its clutches through a slight flexure of the (very thin) aluminum side walls. This mount is then glued on top of a shear mode piezo, which itself is attached to a gold-plated surface (the upper most component of Figure 2.10A) through a vacuum safe conductive epoxy [56]. The cavity is then formed by placing an identical assembly (mirror, aluminum mount, and piezo) opposite the first. The length of the cavity can be scanned by applying a high voltage difference between top and bottom surfaces of each piezo.

Unfortunately, the piezos can not be reliably used to correct for all of the high frequency vibrational disturbances to the cavity. The general problem is that mirror assemblies, such as the one described here, always exhibit low frequency mechanical resonances in the range $\sim (10-50)$kHz; these resonances are caused by a combination of mass loading effects and the poor mechanical rigidity imparted by the epoxy joints (for our cavity mount the first mechanical resonance is at ~ 15kHz.) Consequently, servo loop bandwidths are generally limited to $\lesssim 1$kHz by the (undesirable) coupling of electronic noise into the system through these mechanical resonances. This necessitates the use of passive vibration isolation to stop the native high frequency
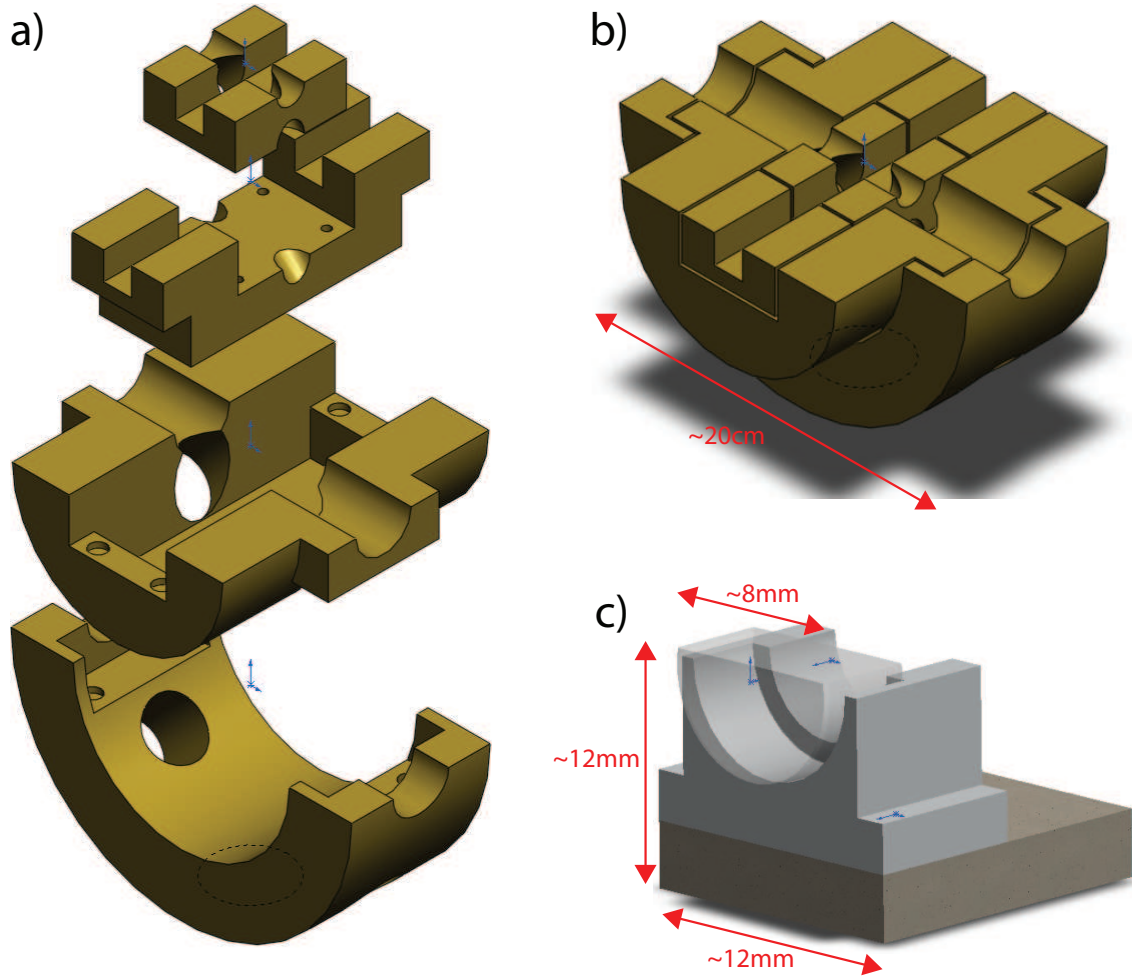
Figure 2.10:   Cavity construction and vibration isolation.

vibrations from coupling into the cavity.

The required vibration isolation was attained through an alternating stack [57, 58] of four copper masses (shown in Figure 2.10A) separated by rubber springs (not pictured). These masses were shaped so as to most efficiently fill the available volume within the vacuum chamber while still providing sufficient optical access for the experiment. The three lowest stages in Figure 2.10A rest atop RTV-615 [59] rubber bumpers, whereas the final stage that houses the cavity mounts rests atop Viton tabs. These rubber materials were chosen for the following reasons. First, they are both vacuum compatible and, in particular, are known to negligibly contaminate high finesse mirror surfaces through their outgassing [60]. Second, as rubber materials go RTV-615 has a relatively low elastic modulus and very low loss, meaning that it is
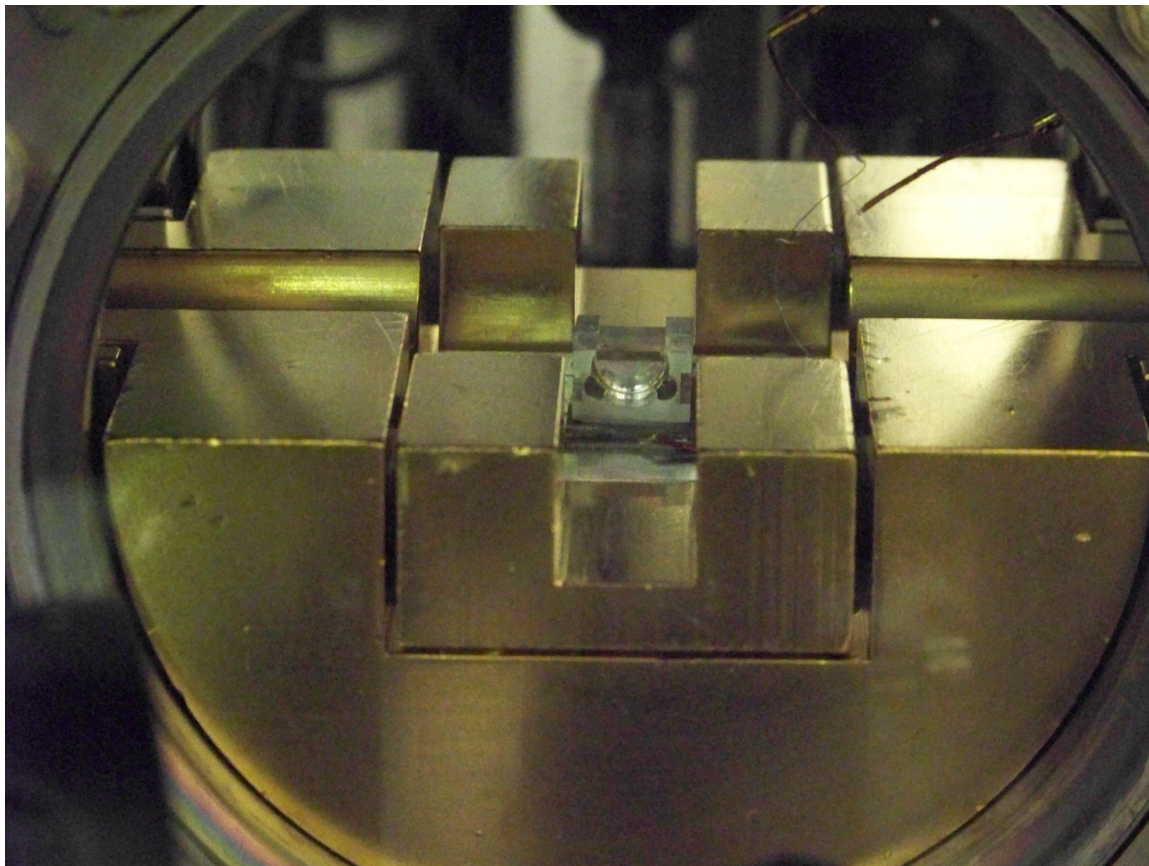
Figure 2.11: A photo of the cavity resting on the vibration isolation stack resting within the vacuum chamber. The lowest element of the vibration stack is not visible.

ideally suited for constructing an isolation system with high frequency vibration attenuation. Third, as Viton is relatively lossy it is well suited to act as a vibration damper in the final stage [61].

With properly sized rubber bumpers, the entire assembly fits together rather snugly (Figure 2.10B); it rests even more snugly within the vacuum chamber, as can be seen in Figure 2.11. Note, the lower-most element of the vibration isolation stack is not visible in this photo. As copper oxidizes quite readily, and therefore necessitates a rather nasty vacuum preparation procedure [62, 63], we had the entire stack plated with gold [64]. Also visible at the top right quadrant of the photo are two wires that carry the piezo control voltage. These are standard, commercially available UHV vacuum-grade wires, but with the outer Kapton sheath removed (using a razor) so that minimal vibrational energy is coupled into the cavity mount.
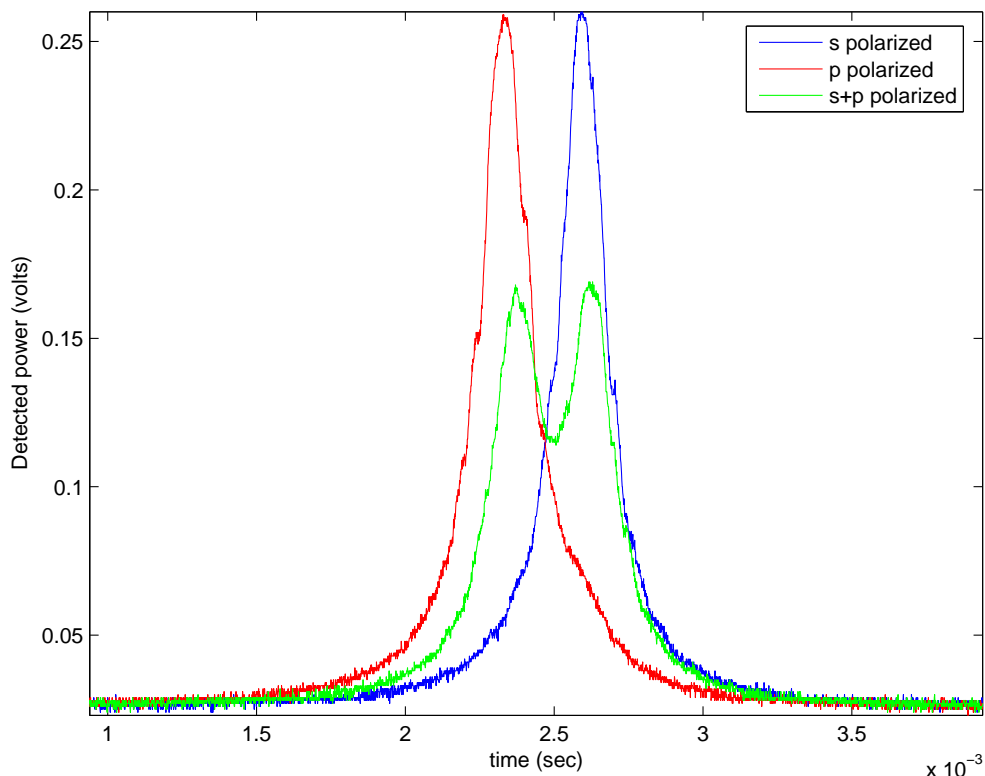
Figure 2.12: Cavity transmission for three different incident polarizations. As a point of reference, for a 'p'-polarized signal the electric field polarization is parallel to the top surface of the mirror shown in Figure 2.10C, and for 's'-polarized it is perpendicular.

Measuring (by eye) the vibrational characteristics of the assembled stack, I estimate that the normal modes lie in the range $\sim (5-20)$Hz, meaning that laboratory vibrational disturbances for frequencies greater than $f = 100$Hz are greatly attenuated at the cavity stage. In practice the cavity length is easily stabilized using piezo feedback with a servo unity-gain bandwidth $\lesssim 100$Hz, and even moderate disturbances to the optical table do not unlock it.

2.3.1.4 Cavity issues

Ah, sweet irony. The design of the aluminum 'flexure-mode' mirror mount in Figure 2.10C was motivated by a desire to minimize stress-induced birefringence that is ubiquitous in high finesse cavities assembled by directly gluing the mirrors into
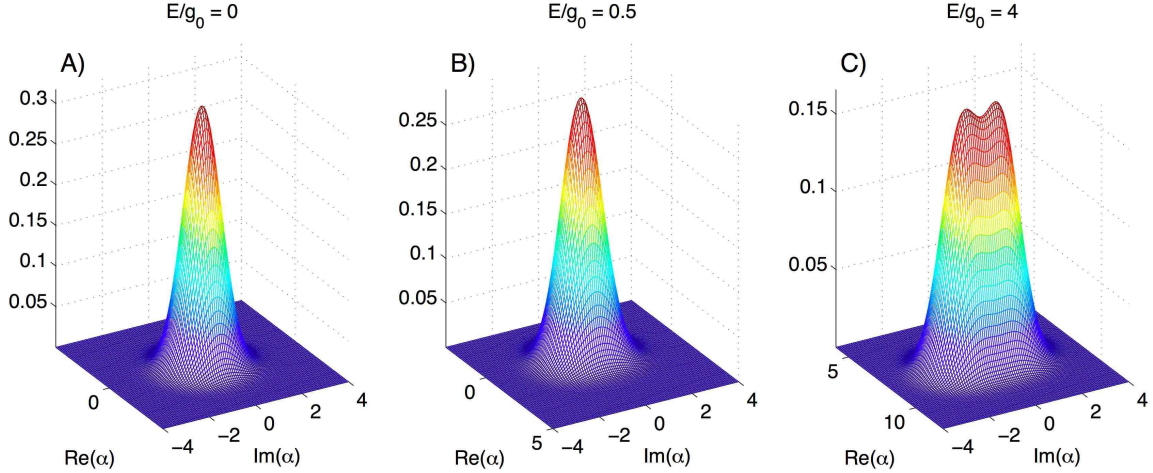
Figure 2.13: Steady-state Q function for the *realized* experimental parameters. The parameters are $\{g_0, \kappa, \gamma_\perp\} = 2\pi \times \{16, 8.0, 2.6\}$MHz. The drive strengths are A) $\mathcal{E} = 0$, B) $\mathcal{E} = g_0/2$, and C) $\mathcal{E} = 4g_0$.

place [39, 65]. Figure 2.12 indicates that the stresses induced by our glue-less technique are still considerable. The displayed data represents three successive measurements of the cavity transmission with the input polarization rotated from 's' (linear vertical) to 'p' (linear horizontal) in 45° increments. A double Lorentzian fit to the 's+p' signal (this fit is not displayed) confirmed that the modes are split by $\Delta f \approx 20$MHz, which is slightly larger than the cavity linewidth.

This mode splitting implies that the cavity only supports circularly polarized light, 's±ip', for a laser frequency situated directly between the cavity eigenmodes. As it turns out, the phase bistability (Figures 2.8 and 2.9) is lost for a detuning this large ($\Theta \approx 2.5\kappa$), implying that we must instead work with linearly polarized light and π-transitions in Cesium [55]. Not only does this give rise to complications due to optical pumping, as discussed in Section 2.3.7.2, but it also brings an unfortunate reduction in the atom-field coupling constant, $g_0 \rightarrow 2\pi \cdot 16$MHz. In this case, $g_0/2\kappa \approx 1$, and the mode splitting exhibited by the resulting Q-function, Figure 2.13, is less than impressive.
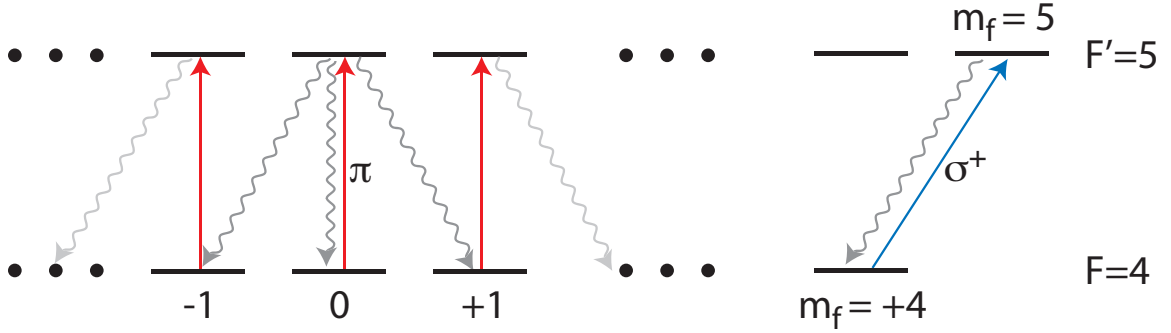
Figure 2.14: Schematic of Cesium $F = 4 \rightarrow F' = 5$ transitions excited by either circularly (blue) or linearly (red) polarized light.

2.3.1.5 Working with a birefringent cavity

The reduction in g_0 is not the only problem caused by our use of linearly-polarized interactions; additionally, we can no longer think of our atom as a closed two-level system. When using circularly polarized light, we can reduce the atomic system to the $F = 4, m_f = 4$ and $F' = 5, m'_f = 5$ hyperfine levels, because, in this case, the excited state can only decay back down to initial state (depicted in Figure 2.14). For linearly polarized transitions, however, spontaneous emission will couple adjacent levels in the $F = 4$ ground state manifold. Therefore, regardless of the initial atomic state, the linear cavity probe excitation will lead to some finite steady-state population in each m_f magnetic sublevel.

The second problem is the existence of the orthogonal cavity mode, detuned by $\approx 2.5\kappa$. While we do not excite this orthogonal mode, the atoms are still coupled to it. For the case of σ^+-polarized interactions between the $m_f = 4$ and $m'_f = 5$ levels, the presence of the undriven σ^--polarized mode is irrelevant, since the excited state can not couple to any state through σ^- transitions. But, for linearly polarized transitions, we are not so lucky. For example, the excited $F' = 5, m'_f = 0$ state couples through the orthogonal cavity mode to a superposition of the $F = 4, m_f = -1$ and $F = 4, m_f = +1$ states.

To deal with these problems, we use the formalism of Ref. [66] to model the multilevel atom, and the formalism of Ref. [65] to model the two-mode cavity. We restrict interactions to the $F = 4$ and $F' = 5$ hyperfine states of the Cesium D2

line [55]. We take the driven cavity mode to be $\hat{z}$-polarized, with the orthogonal mode $\hat{y}$-polarized. The Jaynes-Cummings Hamiltonian generalizes to

$$\hat{H}_{jc}^{(2)} = \Theta_z \hat{a}^\dagger \hat{a} + \Theta_y \hat{b}^\dagger \hat{b} + \Delta \hat{P}_5' + ig_0(\hat{a}^\dagger \hat{S}_z - \hat{a}\hat{S}_z^\dagger) + ig_0(\hat{b}^\dagger \hat{S}_y - \hat{b}\hat{S}_y^\dagger) \ . \tag{2.89}$$

Here, $\hat{a}$ and $\hat{b}$ are the field annihilation operators for the $\hat{z}$ and $\hat{y}$ modes, respectively. $\hat{S}_z$ and $\hat{S}_y$ are the multilevel extensions of the Pauli lowering operators for interactions between the $F = 4$ and $F' = 5$ levels using $\hat{z}$ and $\hat{y}$ polarized fields, respectively. In terms of the standard spherical basis, $\hat{S}_y = i(\hat{S}_+ + \hat{S}_-)/\sqrt{2}$, where $\hat{S}_\pm$ are the lowering operators for circularly polarized transitions. Here, $g_0 = 2\pi \cdot 22\text{MHz}$, and the lowering operators, $\hat{S}_{\pm,z}$, are normalized such that $\langle 4, 4|\hat{S}_+|5, 5\rangle = 1$. Θ_z and Θ_y are the cavity-probe detunings for the two modes, with the restriction $\Theta_y = \Theta_z + 2\pi \cdot 20\text{MHz}$ set by the mode birefringence. $\hat{P}_5'$ is the excited state projection operator. The Lindblad decay is generalized over the independent atomic decay channels and the additional cavity mode. In Figure 2.15 we plot, in red, the transmission spectrum for $\hat{z}$-polarized light coupled to this two-mode, multilevel system. For comparison, we also plot the ideal transmission spectrum for a two-level atom interacting with a single mode, with $g_0 = 2\pi \cdot 16\text{MHz}$ (this is the maximum π coupling strength, attained between the $m_f = 0$ and $m_f' = 0$ states). The atomic transitions and the $\hat{z}$ cavity mode (shown as the dashed black curve) are simultaneously resonant at frequency ω_0. The orthogonal mode, detuned by $\approx 2.5\kappa$, is represented as the dash-dot black curve.

In Figure 2.16 we plot the the steady-state Q-function, projected along the Im $[\alpha]$-axis, for three cases. The black curve represents the ideal two level case, with parameters in 2.13C. The blue curve (hidden behind the red) is the steady-state result for a single-mode cavity, but with all $F = 4$ and $F' = 5$ hyperfine levels included. The red curve is a two-mode analysis. In this case, however, only magnetic sublevels in the range $+3 \geq m_f \geq -3$ are included, due to numerical limitations imposed by the large state space. We see here that the inclusion of the full manifold of hyperfine states leads to only a minor narrowing of the (already narrow) 'bimodal' distribution. Fortunately, the addition of the orthogonal mode has only a small added effect. This
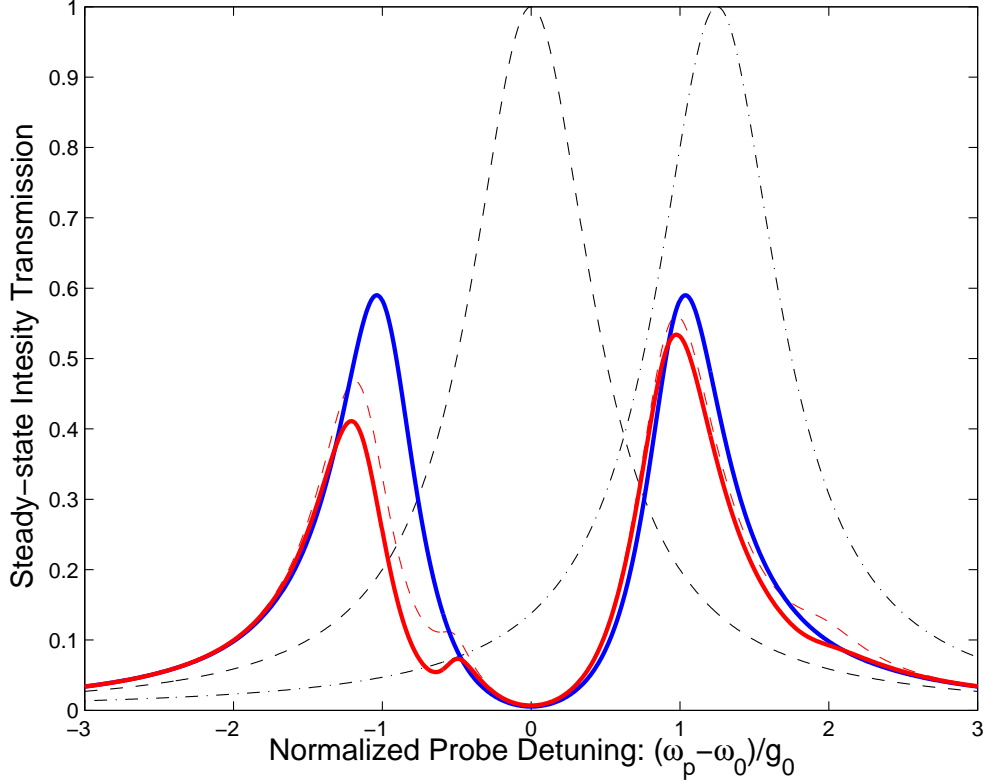
Figure 2.15:   Comparison between steady-state cavity transmissions, in the weak excitation regime. The idealized transmission for a two-level atom coupled to a single cavity mode, with $g_0 = 2\pi \cdot 16\text{MHz}$, is plotted in blue. The solid red curve is the $\hat{z}$-polarized transmission for the two-mode cavity with all Cesium $F = 4$ and $F' = 5$ levels included. The dashed red curve is the total transmission for the $\hat{z}$ and $\hat{y}$-polarized light. The dashed black curve shows the driven $\hat{z}$ polarized cavity resonance, and the dash-dot black curve is the orthogonal $\hat{y}$ mode. The atomic transitions and $\hat{z}$ mode are resonant, with frequency ω_0.

is probably because the birefringent splitting is relatively large when compared to the coupling strengths for the $\hat{y}$ interactions near $m_f = 0$. Note, however, that inclusion of the extended hyperfine states, *e.g.*, $m'_f = \pm 5$, will certainly modify the two-mode analysis, since these states couple strongly to σ^+ and σ^--polarized light.

I note here, before moving on, that all of the experimental analysis of Section 2.3.7.4 is performed using the idealized two-level atom model. As we will see, that model captures the essential features of the experimental data.
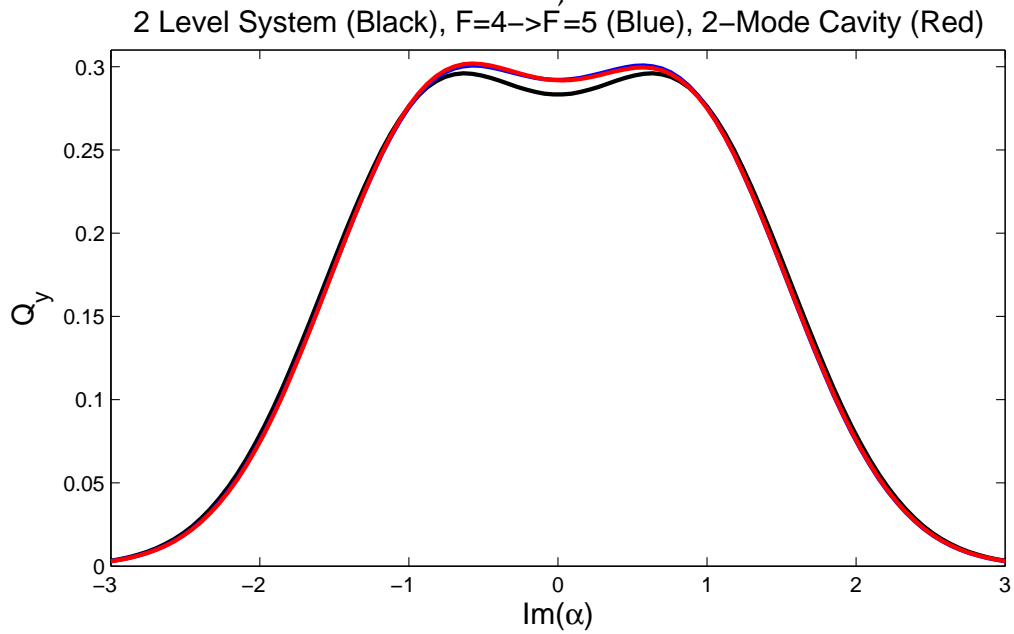
Figure 2.16: Comparison between steady-state Q-functions for a two-level system, a multilevel atom, and a multilevel atom and two-mode cavity. For clarity, only the cumulative distributions of the Q-functions along $\text{Im}\,[\alpha]$ are plotted here. The black curve is for a two-level atom. The blue curve is for a single mode cavity interacting with the entire $F = 4$ and $F' = 5$ states. The red-curve is for a two-mode cavity interacting with a multilevel atom, but only including magnetic sublevels up to $+3 \geq m_f \geq -3$.

2.3.2 The apparatus in brief

Figure 2.17 is a schematic representation of the experiment. Before, describing in detail the function of these various components, I will provide a brief overview of the apparatus as a whole. The vacuum chamber houses both the cavity and the atomic Cesium, and is the home for all of the important physics. In order to both excite and measure the atom-cavity system behavior, a probe beam is coupled into one side of the cavity, the 'input', with the other side, the 'output', measured by a balanced homodyne detector [16, 67]. This homodyne photocurrent is digitized and stored on a PC.

As the experiment necessitates the use of a weak probe ($\sim$ 10pW–1nW of CW power) that is rapidly modulated on and off, an auxiliary laser reference is used to stabilize the cavity length. To this end, light from a titanium-sapphire ring laser
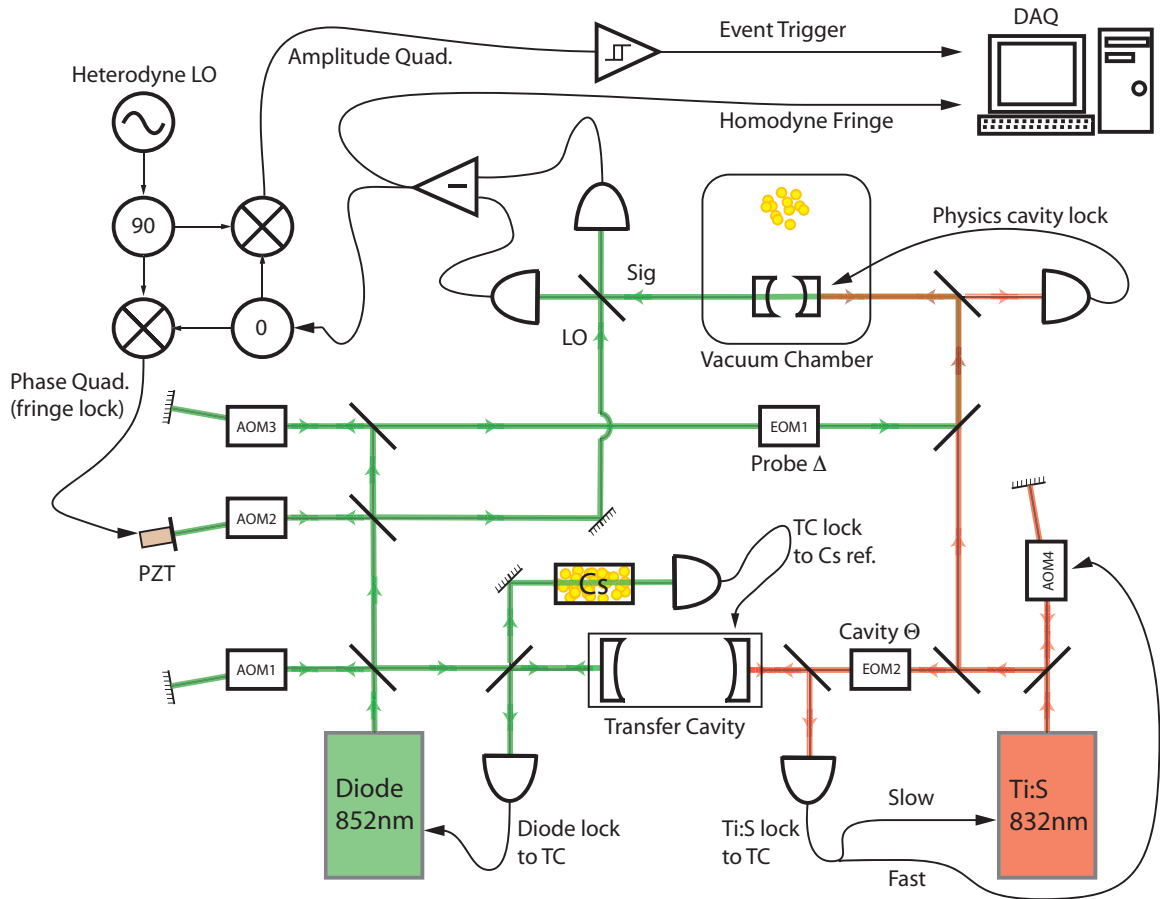
Figure 2.17: An experimental schematic focusing on the optical and electrical components that measure and control the lasers and cavities. For clarity, the components necessary for conditioning the atoms, *i.e.*, the laser cooling and trapping beams, *etc.*, have been omitted.

(Ti:S) is also coupled into the cavity; measurement of its reflected signal is used to stabilize the cavity length. Finally, a transfer cavity (distinct from the experimental cavity) is used to stabilize the frequency difference between the diode laser and the Ti:S.

2.3.3 Laser frequency generation and cavity stabilization

In this section I make repeated references to the components of Figure 2.17. I apologize if the following reads like stereo installation instructions, but I attempt to detail the numerous components concisely.

2.3.3.1 Probe generation

The probe beam is generated from a homemade grating-stabilized diode laser [68, 69] set up to operate near the nominal wavelength, $\approx 852.36\text{nm}$, of the Cesium D2 transition manifold [55]. A small portion, $\sim 1\text{mW}$, of this diode's output is double-passed through an acousto-optic modulator (AOM1), driven at $f_{A1} = 126.5\text{MHz}$, with the positive first-diffracted order selected out. Part of this light passes through an electro-optic phase modulator ('EOM3', not shown in Figure 2.17) and is coupled into a transfer cavity. The transfer cavity is approximately 19cm long and is comprised of two 25cm radius-of-curvature mirrors glued within a solid brass housing. It has a measured axial mode splitting, $FSR_{tc} = 797\text{MHz}$, and ring-down time, $\tau_{tc} = 16\mu\text{s}$, implying a linewidth, $\delta f_{tc} = 1/(2\pi\tau_{tc}) \approx 10\text{kHz}$, and a finesse, $\mathcal{F}_{tc} \approx 80,000$. EOM3 is driven by a radio-frequency (RF) signal so that small frequency-modulation (FM) sidebands are placed on the light. The Pound-Drever-Hall technique [70] of demodulating the cavity reflected signal is used to lock the diode laser's frequency to a cavity axial mode. This servo-loop consists of grating and current feedback with unity gain bandwidth $\sim 500\text{kHz}$.

Unfortunately, the transfer cavity lacks long-time frequency stability due to thermally induced variations to its length. Therefore, prior to passing through EOM3, a small fraction of AOM1's output is sent to a Cesium modulation transfer spectrometer [71, 72] which produces atomic line-shape signals that are nearly independent of the linear absorption coefficient. The error signal obtained from the $(6S_{1/2}, F = 4) \rightarrow (6P_{3/2}, F' = 5)$ transition is used to stabilize the transfer cavity length through actuation of a tube-piezo-mounted intracavity mirror, with a servo bandwidth $\sim 100\text{Hz}$. As the diode laser is already locked to the transfer cavity at DC, this feedback loop also imparts it with absolute frequency stability. By monitoring the size of the spectrometer's residual error signal in closed loop, I estimate an RMS frequency jitter of $\lesssim 100\text{kHz}$ (measured in a 10kHz bandwidth), which is negligible in comparison to the relevant experimental parameter, $\kappa/2\pi \approx 8\text{MHz}$.

Once the diode laser and transfer cavity are stabilized as described above, the

diode laser light itself (*i.e.*, what does not pass through AOM1) is detuned from the Cesium $F = 4 \rightarrow F' = 5$ transition by $-2f_{A1} = -253$MHz. Therefore, to generate the local oscillator required for homodyne and heterodyne detection, some (~ 10mW) of the diode's output is double passed through AOM2, with the positive first-order diffracted signal chosen again. For almost all experimental measurements, AOM2 is driven by the same RF sourcing AOM1, at $f_{A2} = f_{A1} = 126.5$MHz, so that its output is nominally resonant with the $F = 4 \rightarrow F' = 5$ transition. Some of the diagnostic measurements, however, require a detuning of the local oscillator over a range ± 40MHz from this nominal value. This is accomplished by generating a drive frequency $f_{A2} = f_{A1} \pm f_{OFF}$ through a phase-locked loop [73] that incorporates an offset frequency, f_{OFF}, generated by an independent RF synthesizer. As the frequency shift imparted by AOM2 is $2 \times f_{A2}$, the local oscillator offset from the Cesium transition is $2 \times f_{OFF}$.

The remainder ($\sim 100\mu$W) of the diode laser's output is double-passed through AOM3, which is driven at an RF frequency, $f_{A3} = 2 \times f_{A1}$, generated by frequency doubling the RF signal driving AOM1. In this case, the negative first-order diffraction peak is selected, thereby providing laser light that is nominally shifted 759MHz *red* of the Cesium $F = 4 \rightarrow F' = 5$ transition. AOM3's output then passes through a waveguided electro-optic modulator (EOM1) [74] that is driven at an RF frequency, $f_{E1} = 6 \times f_{A1} - \Delta/2\pi$. The upper sideband generated by EOM1 provides the atom-cavity probe with a detuning parameter $\Delta = \omega_a - \omega_p$, as in the Hamiltonian 2.7. Note that, in general, two RF synthesizers are used to drive EOM1: the first generates a weak heterodyne probe that may be monitored to sense the presence of an atom; the second generates the intense resonant signal that drives the atom-cavity system into the large excitation regime. The two signals are never on simultaneously, however (details in Section 2.3.6.3.)

2.3.3.2 The cavity locking beam

A titanium-sapphire (Ti:S) monolithic block resonator (Coherent Inc. MBR-110), operating at ≈ 832nm, sources the laser light that ultimately serves as the cavity sta-

bilization reference. Light from the Ti:S is double-passed through AOM4, nominally operating at $f_{A4} \approx 90\mathrm{MHz}$, and is then sent through another waveguided electro-optic modulator (EOM2), that imparts FM sidebands at RF frequency, f_{E2}. By phase modulating f_{E2}, one of these sidebands may be locked to the transfer cavity using the ubiquitous PDH technique. The servo loop accomplishing this has two branches: the first branch actuates the voltage-controlled oscillator generating f_{A4}, to provide fast frequency feedback in the range 10Hz–500kHz; the second loop, operating from DC-100Hz, provides low frequency stability through feedback to a Fabry-Perot cavity residing within the MBR-110 housing. A small fraction, $\sim 1\mu\mathrm{W}$, of the AOM4's output is then passed through yet another EOM (not pictured) before being coupled into the experimental cavity; its reflected signal is used to stabilize the cavity length through feedback to the shear mode piezos, with a servo bandwidth $\sim 100\mathrm{Hz}$, as described in Section 2.3.1.3. By tuning the RF frequency f_{E2} sourcing EOM2, the cavity-probe detuning parameter, Θ, may be adjusted.

In practice things are not so simple, since the experimental cavity's axial mode spacing, $FSR = 2.1\mathrm{THz}$, far exceeds both the sourcing range of f_{E2} and the response range of EOM2. In order to get all the frequencies "just right"[51] I employ the following procedure. First, the diode laser is prepared using the steps outlined above, and the probe transmission signal is monitored by manually adjusting the cavity length into resonance while it is being swept. The Ti:S wavelength is now manually adjusted until the diode probe and the Ti:S probe are simultaneously resonant with different cavity TEM_{00} modes. The cavity length is now locked to this Ti:S probe resonance. f_{E2} is tuned (over a range $FSR_{tc} = 800\mathrm{MHz}$) until a Ti:S transfer cavity resonance is found; the Ti:S frequency is now locked. Finally, fine adjustments to f_{E1} and f_{E2} set the experimental Δ and Θ parameters.

2.3.4 The atoms: cooling and delivery

I will provide a brief description of the laser cooling and trapping apparatus that provides the source of cold(-ish) atoms for the experiment. But since the techniques

employed in this experiment are industry standards [11, 14, 75–78], and since even more extravagant methods exist [15, 17, 79–81], I won't dwell on the basics here. But before moving on, I should point out that essentially *all* of the laser cooling and trapping hardware was made by Tony Miller. In particular, he designed and assembled all of the following: the vacuum chamber, the magnetic field coils, the immediate hardware used to create the fiber MOT, the tapered amplifier that sources the intense trapping beams, and the RF electronics responsible for controlling and shuttering these magneto-optical components (details may be found here [82]). I then swooped in and commandeered what was essentially his apparatus. I am greatly indebted to him; I may even thank him one day. Also, I would be remiss if I didn't thank Kevin McHale who, in a fit of procrastination, rapidly assembled the diode laser that sources the MOT repumping light.

Within the vacuum chamber at background pressure $\sim 10^{-9}$ Torr, light from six independent fiber-coupled beams [83], of $\sim$ 1cm diameter each, intersect approximately 8mm above the cavity axis. Anti-Helmholtz coils, configured such that their axis of symmetry is parallel to that of the cavity, provide a magnetic field gradient of about 15G/cm. Finally, a Cesium getter [84] driven with currents $\lesssim$ 3Amps sources enough atoms to form a bright MOT with a near Doppler limited temperature of $\sim 200\mu$K. During a typical experimental cycle, the MOT is loaded for $\sim$ 1sec, at which point the trapping beams and anti-Helmholtz coils are turned off, and a cold atomic cloud of $\lesssim 10^5$ atoms free-falls towards the cavity.

At no point was there any serious attempt made to achieve sub-Doppler cooling of the atoms. The reasons for this are as follows. Over an $\sim$ 8mm drop, an atom initially at rest is gravitationally accelerated up to $v_g \sim 40$cm/s by the time it reaches the cavity mode. The near-Doppler limited velocity of the MOT, $v_{dop} \sim 10$cm/s, is already significantly smaller than v_g. Furthermore, the free-fall limited atom-cavity transit time, $\tau = w_0/v_g \sim 100\mu$s, is already long enough to perform the phase bistability experiment (characteristic time $\sim 1/\gamma_\perp \approx 60$ns).

There is the minor complications of getting the atoms into the cavity, however. Once the MOT is turned off, the atoms fall and expand due to their non-zero initial

temperature. A doppler limited MOT cloud will expand to $\sim$ 5mm in size by the time it reaches the cavity. As the mirrors that form the cavity are nominally 7.75mm in diameter, and with a 25cm radius of curvature, there is but a 10μm gap for the atoms to fall through (note, this small gap is caused by the mirror sagittal depth of 'sag', and is distinct from the cavity length $\approx 70\mu$m). In this case, efficient atom delivery would require a delicate positioning of the MOT above the cavity and careful cancellation of stray magnetic fields. Furthermore, we would need to insure that the cavity mirrors are negligibly tilted relative to gravity. Instead of fussing with all that, we had the Stanford Crystal Shop lap down each mirror's edge by about 3mm. This 'flat-top' mirror geometry, displayed in Figure 2.10C, provides a $\approx 60\mu$m gap. From Monte-Carlo simulations of this system [65], I estimate that a MOT of $\lesssim 10^5$ atoms positioned 10mm above the cavity and within $\sim$ 1mm of the gap, will leave about one atom in the cavity mode per drop.

Finally, I'll briefly go over the chain of optical components that generate the MOT light. A fraction of the diode laser's direct output is double-passed through an AOM, which provides a net positive frequency shift in the range 160MHz to 220MHz. About 10μW of this light is used to seed a slave laser. Most of the slave laser's output power, $\sim$ 40mW, is directed into an homemade tapered amplifier. The output of this tapered amplifier receives yet another +40MHz shift through an AOM before being coupled into an optical fiber. The optical fiber passes through an inline six-way splitter, thus providing the MOT trapping beams. A separate diode laser, locked to the Cesium $F = 3 \rightarrow F' = 4$ transition, is coupled into the same six-way fiber splitter so as to provide the MOT repump light.

2.3.5   Homodyne detection and calibration

The light that exits the cavity first passes through a dichroic beamsplitter (not pictured in Figure 2.17) which reflects $> 95\%$ of the 852nm light and transmits $\approx 30\%$ of the 832nm locking light (which is measured to provide a monitor of the cavity lock.) The reflected probe is routed into a 50/50-beam splitter where it is combined with an
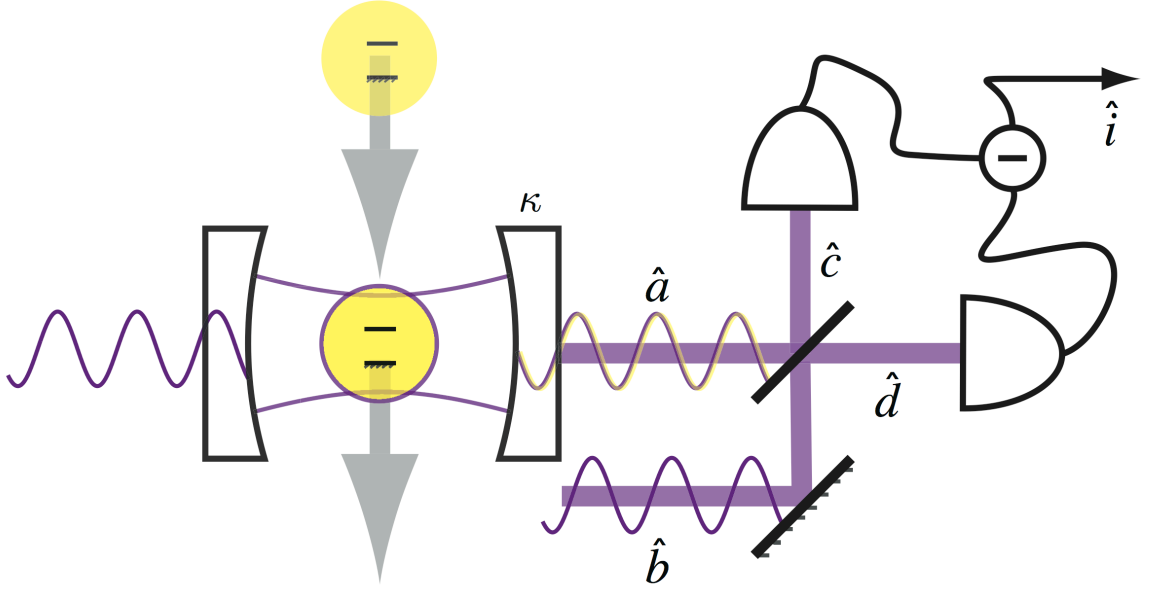
Figure 2.18: A schematic pictorial of the homodyne/heterodyne detection of an atom falling through the cavity field.

intense local oscillator. Photodetection of the two output modes of this beam splitter realize a homodyne measurement of the atom-cavity field [85]. Below, I briefly provide a sketch of the theoretical formalism behind this measurement in order to introduce the definitions and formulae that will be referred to later.

2.3.5.1 The measurement

Referring to the configuration in Figure 2.18, we have the operators

$$\hat{c} = (\hat{a} + \hat{b})/\sqrt{2} \,, \tag{2.90}$$

$$\hat{d} = (\hat{a} - \hat{b})/\sqrt{2} \,, \tag{2.91}$$

where $\hat{a}$ is the output field [35, 86] of our system (*i.e.*, atom + cavity) and $\hat{b}$ is the operator for the local oscillator mode. For (quasi-)monochromatic fields the photodetector response is proportional to the incident number operator [87, 88], so that the

measured signal in a balanced configuration will be proportional to

$$\hat{i} = \hat{c}^\dagger \hat{c} - \hat{d}^\dagger \hat{d} \tag{2.92}$$

$$= \hat{a}^\dagger \hat{b} + \hat{b}^\dagger \hat{a}. \tag{2.93}$$

Assuming the local oscillator is in a coherent state, we set $\hat{b} \to |\beta|e^{i\theta}$ and obtain

$$
\begin{aligned}
\hat{i}_\beta &= |\beta|(e^{i\theta}\hat{a}^\dagger + e^{-i\theta}\hat{a}) \\
&= 2|\beta|\hat{X}_\theta \ ,
\end{aligned}
\tag{2.94}
$$

where $\hat{X}_\theta$ is the field quadrature operator[6] defined by the angle θ (the standard convention is to define $\theta = 0$ as the 'amplitude' quadrature and $\theta = \pi/2$ as the 'phase' quadrature.) Eq. 2.94 is the key result in this (grossly simplified) picture of homodyne/heterodyne detection: it implies that if the local oscillator is in a well defined coherent state, the detected photocurrent is directly related to the signal field, fluctuations and all.

2.3.5.2 The 'signal' and the 'noise'

The first and second moments of this photocurrent operator are

$$\langle \hat{i} \rangle = 2|\beta|\langle \hat{X}_\theta \rangle \ , \tag{2.95}$$

and

$$
\begin{aligned}
\langle \Delta \hat{i}^2 \rangle &= \langle (\hat{i} - \langle \hat{i} \rangle)^2 \rangle = \langle \hat{i}^2 \rangle - \langle \hat{i} \rangle^2 \\
&= 4|\beta|^2 \langle \Delta \hat{X}_\theta^2 \rangle + \langle \hat{a}^\dagger \hat{a} \rangle \approx 4|\beta|^2 \langle \Delta \hat{X}_\theta^2 \rangle \ ,
\end{aligned}
\tag{2.96}
$$

where the final approximation is valid for an intense local oscillator: $|\beta|^2 \gg \langle \hat{a}^\dagger \hat{a} \rangle$. This analysis can easily be generalized for higher moments of $\hat{X}_\theta$, and we see that the

---

[6]Conventions vary for the normalization of the field quadrature operators. I use the convention $\hat{X}_\theta = \frac{1}{2}(e^{-i\theta}\hat{a} + e^{i\theta}\hat{a}^\dagger)$. However, most texts use either $\hat{X}'_\theta = (e^{-i\theta}\hat{a} + e^{i\theta}\hat{a}^\dagger)$ or $\hat{X}_\theta = \frac{1}{\sqrt{2}}(e^{-i\theta}\hat{a} + e^{i\theta}\hat{a}^\dagger)$.

local oscillator essentially acts as a multiplicative factor: it generates a large signal proportional to $\hat{X}_\theta$ which may be readily measured in the presence of extrinsic noise sources [67, 85].

To see this, we consider the case where the signal is in a coherent state, $\langle \hat{a} \rangle = |\alpha|e^{i\phi}$, and so $\langle \Delta \hat{X}_\theta^2 \rangle = 1/4$. For $|\beta|^2 \gg |\alpha|^2$ we have

$$\begin{aligned} \langle \hat{i} \rangle &= 2|\alpha||\beta| \cos (\phi - \theta) \ , \\ \langle \Delta \hat{i}^2 \rangle &\approx |\beta|^2 \ . \end{aligned} \tag{2.97}$$

In practice, the relative phase, $\phi - \theta$, may be controlled by changing the local oscillator optical path length leading to the 50/50 beamsplitter. This is accomplished through a piezo mounted mirror, as depicted in Figure 2.17. This way we realize phase, $\phi - \theta = \{\pm \pi/2\}$, and amplitude, $\phi - \theta = \{0, \pi\}$, quadrature measurements for an arbitrary signal.

The measurement signal-to-noise ratio is *independent* of the local oscillator

$$\frac{\mathcal{S}^2}{\mathcal{N}} = \frac{4|\alpha|^2|\beta|^2}{|\beta|^2} = 4|\alpha|^2 \ , \tag{2.98}$$

which simply serves to scale up the signal, making it visible in the presence of *extrinsic* noise sources. For example, assuming that our detector has a small amount of excess noise, ξ^2, the signal-to-noise generalizes to[7]

$$\frac{\mathcal{S}^2}{\mathcal{N}} = \frac{4|\alpha|^2|\beta|^2}{|\beta|^2 + \xi^2} \ . \tag{2.99}$$

In practice, if the shot-noise of the LO alone is much larger than the inherent noise of the detector, $|\beta|^2 \gg \xi^2$, then the homodyne/heterodyne measurement will essentially reflect an ideal measure of the signal field quadrature. In this case, the measurement is said to be 'shot-noise-limited'.[8]

---

[7]ξ could be the result of a number of independent noise sources: dark current through the photodiode, current and voltage noise generated by the detector electronics, Johnson noise from a transimpedance resistor, stray electric and magnetic field pick-up, *etc.*

[8]It should be noted, however, that in a quantum-optics theoretic sense this LO shot-noise is a measure of the 'vacuum' field that it is interfering with, since the noise terms actually reflect the

2.3.5.3   An experimentally useful form

Unfortunately, photodetectors don't provide signals in 'coherent state amplitude' units. Assuming both the signal and local oscillator are prepared in coherent states we can use the following expressions for 'real' photocurrents. For a local oscillator and signal with optical powers, P_L and P_S, respectively, the measured current is [85]

$$\mathcal{I} = 2\mathcal{R}\sqrt{P_L P_S}\cos\left(\phi - \theta\right) , \tag{2.101}$$

and the RMS variance in a time window τ is

$$\Delta\mathcal{I}_{rms}^2 = \frac{\hbar\omega\mathcal{R}^2 P_L}{\eta_q \tau} + \Delta i_n^2 . \tag{2.102}$$

Here, $\mathcal{R}$ is the detector responsivity, in [Amps/W], η_q is the detector quantum efficiency, ω is the optical frequency, and Δi_n^2 represents excess current noise. Assuming this excess noise is negligible, the signal-to-noise ratio is

$$\frac{\mathcal{S}^2}{\mathcal{N}} = \frac{\mathcal{I}_{max}^2}{\Delta\mathcal{I}_{rms}^2} = \frac{4\eta_q P_S \tau}{\hbar\omega} , \tag{2.103}$$

which is consistent with Eq. 2.98 if we assume perfect quantum efficiency and identify $|\alpha|^2 = P_S\tau/\hbar\omega$.

Finally, if the steady-state cavity field has mean photon number $\bar{n}$, the detected output photo-flux (in quanta per second) is $2\kappa\eta_T\bar{n}$, where η_T, discussed in Section 2.3.1.3, is the fraction of the intracavity power that makes it into the output mode. In this case, the detected interference fringe is

$$\mathcal{I} = 2\mathcal{R}\eta_L\eta_H\sqrt{2\hbar\omega\kappa\eta_T P_L\bar{n}}\cos\left(\phi - \theta\right) , \tag{2.104}$$

where η_H is the homodyne efficiency that characterizes the spatial overlap between

---

commutation relations

$$\langle\Delta\hat{i}^2\rangle = |\beta|^2[\hat{a}, \hat{a}^\dagger] + |\alpha|^2[\hat{b}, \hat{b}^\dagger] . \tag{2.100}$$

the signal and local oscillator [33], and η_L accounts for optical losses otherwise un-accounted for. In practice Eq. 2.104 is used to scale the measurement photocurrent into 'quadrature-amplitude units'

$$\bar{X}_\theta = \frac{\mathcal{V}}{2\mathcal{R}\mathcal{Z}\eta_L\eta_H \left(2\hbar\omega\kappa\eta_T P_L\right)^{1/2}} \; , \tag{2.105}$$

where $\mathcal{V} = \mathcal{Z}\mathcal{I}$ is the detected voltage and $\mathcal{Z}$ is the detector's transimpedance gain. Following this calibration a direct comparison to the theory of Section 2.2.5 can be made.

2.3.5.4 Homodyne noise and fringe calibration

The homodyne detector is a homemade balanced receiver [89, 90] consisting of two Hamamatsu silicon PIN photodiodes [91], each with an active area diameter of 1.5mm. The difference photocurrent of these photodiodes is converted into a voltage by a transimpedance amplifier, with transimpedance $\mathcal{Z} = 5.1\text{k}\Omega$. The detector's response bandwidth is approximately 30MHz, and its signal-to-noise bandwidth [89, 92] is greater than 10MHz for this local oscillator power.

Generally, the local oscillator power was fixed to $P_L = 3.5\text{mW}$. Setting $P_S = 0$, the optical shot noise level was measured using a spectrum analyzer. Over the frequency band 100kHz–10MHz the optical shot noise was approximately 100 times larger than the detector's electronic noise (the second term in Eq. 2.102). With the cavity probe on resonance and the homodyne fringe locked to zero (*i.e.*, measuring the signal phase quadrature) there was a negligible increase in this noise floor for a range $0 < \bar{n} < 100$ intracavity photons. As $\bar{n}$ was increased past 100 intracavity photons a mound of noise centered near ~ 500kHz could be seen in the photocurrent. This behavior is shown in Figure 2.19, where the measured homodyne photocurrent noise spectrum is displayed for different intracavity photon numbers. These measurements were performed with the homodyne fringe locked to zero using a low frequency feedback loop. The excess noise visible for $\bar{n} \approx 200$ is due, primarily, to phase noise on the RF signal that generates the cavity probe via EOM1.
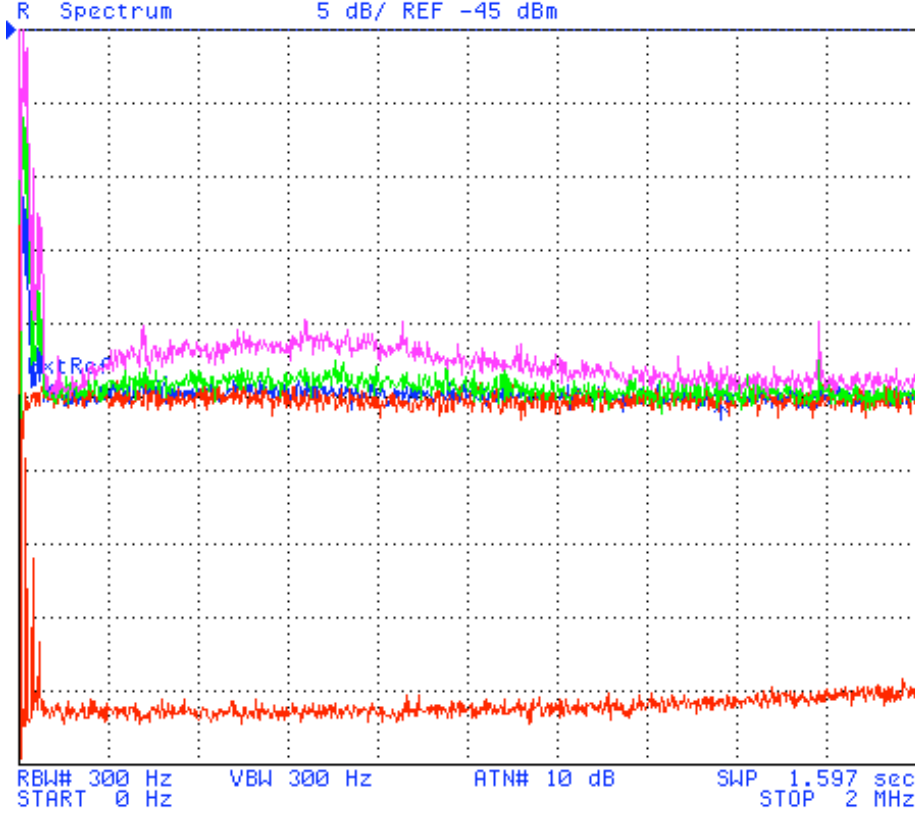
Figure 2.19:   Measured noise spectra of balanced homodyne photocurrents for a range of intracavity photon numbers. The frequency span is from DC-2MHz. The bottom red curve shows the detector noise with no incident light. The upper red curve is the shot noise level when only the local oscillator is present. The remaining curves are for cavity probe strengths corresponding to: $\bar{n} \approx 10$ (blue), $\bar{n} \approx 50$ (green), and $\bar{n} \approx 200$ (magenta). These measurements were performed using a low frequency servo to lock the homodyne fringe to zero.

The homodyne efficiency was determined as follows: the cavity probe strength was increased until the output power, measured *immediately* before the 50/50 beamsplitter, was raised to $\sim 1\mu$W and the local oscillator power was lowered to match. While sweeping the relative phase, $\phi - \theta$ in Eq. 2.101, I measured the fringe contrast

$$\eta_H = \frac{I_{max} - I_{min}}{I_{max} + I_{min}} , \tag{2.106}$$

where I_{max} and I_{min} are the maximum and minimum values of the homodyne photocurrent, respectively. The value so obtained was $\eta_H = 0.95$, which is quite good

indeed.

This leaves only the mysterious factor η_L. This factor most likely accounts for a combination of: losses at the dichroic mirror that separates 852nm and 832nm light; diffraction losses from numerous optical elements in the cavity output beam path (the beam waist is $\sim 5mm$ at the 50/50 beamsplitter); and electronic mis-calibration (for example, in the estimate of $\mathcal{R}$). Note that η_T would not account for any of these factors, since it was determined by measuring the cavity transmission *immediately* outside of the vacuum chamber. Independent calibration of the intracavity photon number, using the procedure discussed in Section 2.3.6.2, indicates that $\eta_L \approx 0.80$.

2.3.6 Heterodyne detection of the atoms

In addition to providing a homodyne measurement of the resonant probe, the balanced receiver detects the RF interference beatnote between the local oscillator and an off-resonant 'heterodyne' probe. This off-resonant probe is generated using an independent RF synthesizer driving EOM1 at a frequency $f'_{E1} = 759\text{MHz} - \Delta'/2\pi$ (note, I will use 'primes' to distinguish between heterodyne probe parameters and homodyne probe parameters.) In this case the detection phase, θ in Eq. 2.94 is oscillating at an RF frequency, $\theta = \theta(t) = \omega_{rf}t$. Subsequent sine and cosine transforms of the photocurrent can provide a 'psuedo-simultaneous' measurement of orthogonal field quadratures over coarse-grained time-scales (though *instantaneous* measurement of orthogonal quadratures is forbidden by stubborn quantum mechanical rules.) Defining x_φ and $y_\varphi = x_{\varphi+\pi/2}$ as these arbitrary orthogonal quadratures, a phase and amplitude quadrature measurement of the intracavity field may be accomplished by varying the local oscillator phase until the mean value of, say, y_φ is zero. In this case, we measure the quadratures

$$
\begin{aligned}
x_0 &= \frac{1}{2}\left(\alpha^* + \alpha\right) , \\
y_0 &= \frac{i}{2}\left(\alpha^* - \alpha\right) ,
\end{aligned}
\tag{2.107}
$$

where α^* is the complex amplitude of the transmitted optical field.

2.3.6.1 Atom transits

As an atom passes through the cavity mode, its interaction with the cavity field strongly influences the transmitted signal (as depicted in Figure 2.18.) In the case of very weak driving, such that $\bar{n}' \ll n_0$, the atom-cavity linear transmission function is

$$T \equiv \frac{\langle \hat{a} \rangle}{\mathcal{E}'/\kappa} = \frac{\kappa(\gamma_\perp + i\Delta')}{(\kappa + i\Theta')(\gamma_\perp + i\Delta') + g_0^2(r)} \ , \tag{2.108}$$

where $g_0(r)$ is the radially dependent atom-field coupling constant. Of course, this is a steady-state expression and is, in general, only valid for an atom fixed at position r. For the atomic transit analysis that follows, however, I ignore transient behavior in the master equation, and assume this steady-state response; this approximation should be valid for carefully filtered signals since the atomic transit time, $\sim 100\mu$s, is very long compared to the dissipative timescales, $\{\gamma_\perp, \kappa\}$. Therefore, I assume that the transmission is modified, in real-time, through the dependence of the spatially dependent coupling term, $g_0(r) = g_0(r(t))$, on the atoms position.

Noting the empty cavity transmission

$$T_0 = \frac{\kappa}{\kappa + i\Theta'} \ , \tag{2.109}$$

the quadratures defined above measure

$$\begin{aligned} x_0 &\propto \left(\frac{T^*}{T_0^*} + \frac{T}{T_0} \right) \ , \\ y_0 &\propto i \left(\frac{T^*}{T_0^*} - \frac{T}{T_0} \right) \ . \end{aligned} \tag{2.110}$$

As we generally work outside the linear regime, the steady-state transmission may be inferred from $\langle \hat{a} \rangle_{ss} = \text{Tr}[\hat{\rho}_{ss}\hat{a}]$. In this case, we have

$$\begin{aligned} x_0 &\propto \left(\frac{\langle \hat{a} \rangle_{ss}^*}{T_0^*} + \frac{\langle \hat{a} \rangle_{ss}}{T_0} \right) \ , \\ y_0 &\propto i \left(\frac{\langle \hat{a} \rangle_{ss}^*}{T_0^*} - \frac{\langle \hat{a} \rangle_{ss}}{T_0} \right) \ . \end{aligned} \tag{2.111}$$
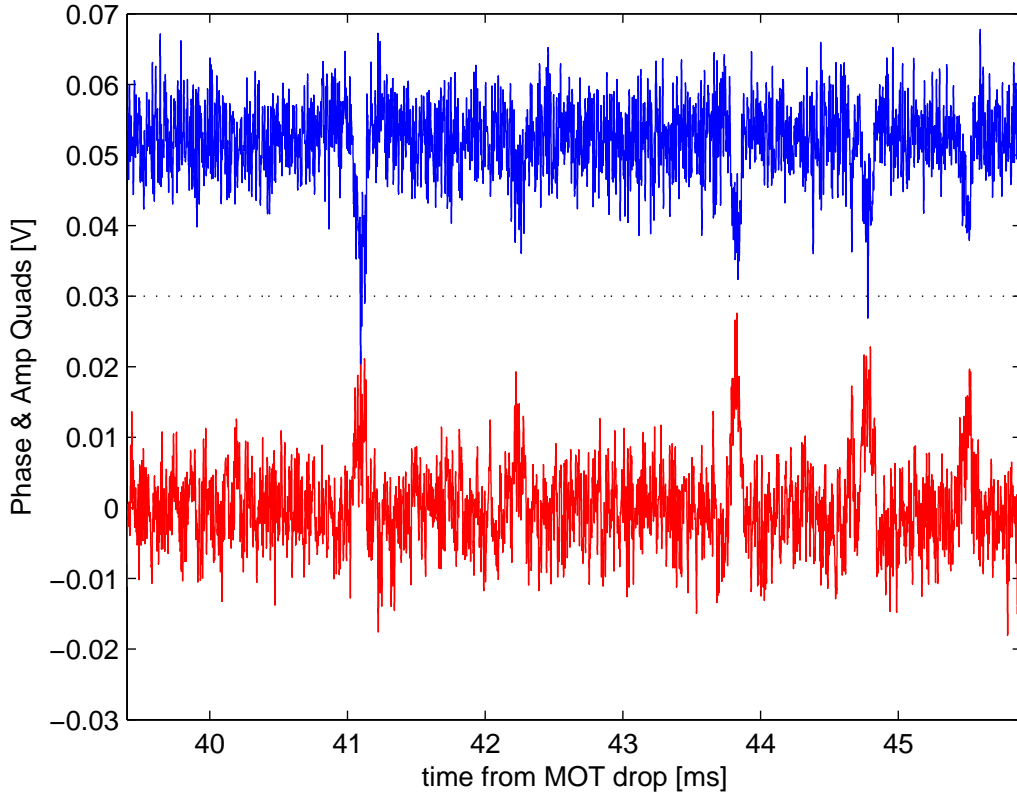
Figure 2.20:   Atomic transits monitored through heterodyne detection with linearly polarized light. A feedback loop stabilizes the phase quadrature(red) to zero. The x-axis notes the time after the MOT was turned off. The detection parameters are $\bar{n}' = 2$, $\Delta'/2\pi = 30\text{MHz}$, and $\Theta'/2\pi = 0$.

Figure 2.20 shows an example of this phase and amplitude quadrature data over $\sim 6\text{ms}$ time window centered approximately 43ms after the MOT is shut off. The data is displayed in a DC-300kHz bandwidth, and the detection parameters are $\bar{n}' = 2$, $\Delta'/2\pi = 30\text{MHz}$, and $\Theta'/2\pi = 0$. Here, five distinct atom transits are observed. In general these transits are accompanied by a sharp drop in the amplitude quadrature and an increase in the phase quadrature. Note that since the transits have only a $\sim 100\mu\text{s}$ temporal width, they interfere negligibly with the heterodyne fringe lock that has a unity-gain bandwidth of 1kHz.

2.3.6.2 Photon number calibration

Since the system response is, in general, nonlinear, these field quadrature measurements provide an independent means of calibrating the intracavity photon number [11]. Figure 2.21 shows the results of this calibration procedure. In each plot, a single atom transit is displayed as a phasor diagram: starting with the amplitude and phase quadrature data versus time, we plot the radius and angle

$$R = \sqrt{\tilde{x}_0(t)^2 + \tilde{y}_0(t)^2} \ ,$$
$$\psi = \tan^{-1}\left(\frac{\tilde{x}_0(t)}{\tilde{y}_0(t)}\right) \ ,$$

(2.112)

where $\tilde{x}_0(t)$ and $\tilde{y}_0(t)$ are the phase and amplitude quadratures normalized by the empty cavity transmission. The theoretical fit comes from steady-state solutions to the master equation with $\{\kappa, \gamma_\perp, \Delta, \Theta\}$ fixed, and the coupling constant $g_0(r)$ varied from its maximal value to zero, so as to simulate an atom moving through the cavity mode waist. The only fit parameter then is $\bar{n}'$, the intracavity mean photon number for an atom-less cavity. The utility of this approach is obvious: by plotting the phase and amplitude quadratures against each other we can remove time from the picture. Thus, complications due to peculiarities of the atomic motion through the Gaussian mode structure are largely avoided. It should be pointed out, however, that the fits are performed by selecting out the largest transits. This way we eliminate transits for which the atom grazes the cavity mode, and thereby insure that we are fitting data where a maximal coupling of $g_0/2\pi = 16\mathrm{MHz}$ is attained. Using these fits for the intracavity photon number, the calibration factor η_L was determined by comparing the measured homodyne fringe size, Eq. 2.104, to the value expected for $\eta_L = 1$.

2.3.6.3 Triggering the resonant probe

The heterodyne signal also serves as a real-time indication of an atom's arrival into the cavity. In particular, a homemade Schmitt trigger [73] monitors the amplitude quadrature photocurrent, and fires when this photocurrent dips below a predeter-
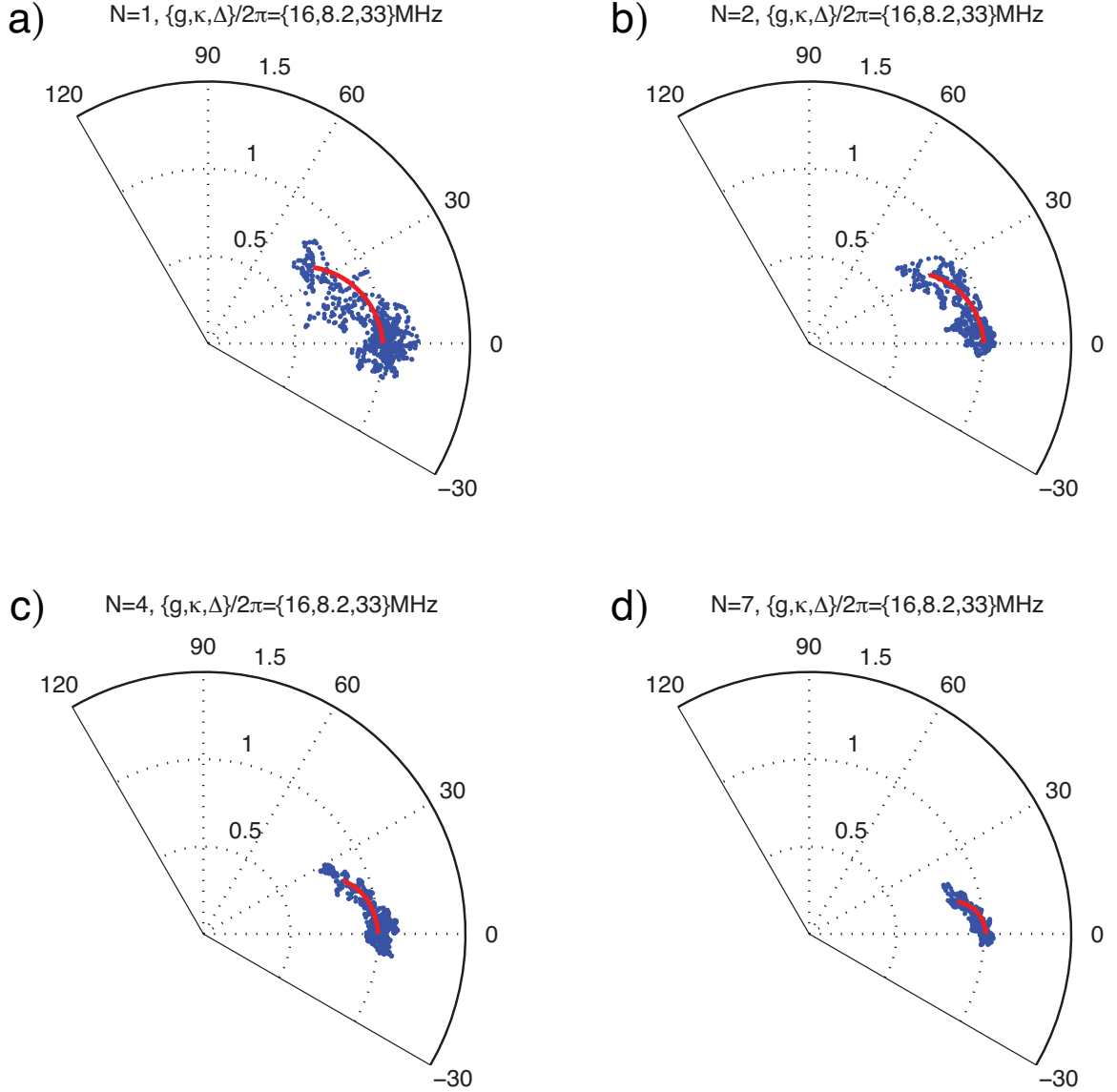
Figure 2.21: Calibration of the intracavity photon number through theoretical fits to the atom-transits. The data is presented as blue dots, while the theoretical fits are in red. For all plots, the we have $\{\Delta', \Theta'\}/2\pi = \{33, 0\}$MHz. The fit mean photon numbers are: a) $\bar{n}' = 1$; b) $\bar{n}' = 2$; c) $\bar{n}' = 4$; d) $\bar{n}' = 7$.

mined threshold. This threshold level is represented by the horizontal dotted line near 30mV in Figure 2.20. By setting the threshold sufficiently low we may selectively trigger off atomic transits for which the atom-field interaction is strong (*i.e.*, transits that pass through the center of the cavity mode.)

With this triggering scheme in place, a typical data acquisition cycle goes as follows. The resonant probe is initially off. While the MOT is loading, the heterodyne

probe is turned on and the demodulated component y_θ is locked to zero (thus defining the phase quadrature.) The MOT is turned off. Some 40ms later the Schmitt trigger, initially in a dormant state, is activated and measures the amplitude quadrature. A drop in the amplitude quadrature triggers the Schmitt output to high – this simultaneously switches the heterodyne probe off and the homodyne probe on. Furthermore, this trigger signal and the homodyne photocurrent are stored on a PC for post processing. Note, in general, the MOT number density is lower than the case of Figure 2.20 – typical densities lead to only $\sim$ one atom visible in the heterodyne photocurrent per drop. On average one triggering event occurs for every four MOT drops.

In order to assure that the homodyne measurement is of the phase quadrature, the homodyne fringe is phase locked to the demodulated signal, y_θ, that defines the heterodyne phase quadrature. Therefore, if y_θ is initially locked to zero, then the homodyne detector is measuring phase. In order to assure that the heterodyne fringe lock responds minimally to the atom transit, the general heterodyne detuning is $\Delta' = \Theta' = 2\pi \cdot 6\text{MHz}$; for these parameters, an atom induces a large dip in the amplitude quadrature but only a moderate change in the phase quadrature.

2.3.7 Results and Analysis

2.3.7.1 Triggered homodyne signals

Four examples of the atom-triggered phase quadrature homodyne measurements are shown in Figures 2.22 and 2.23. In all four figures, $t = 0$ corresponds to the Schmitt trigger event that heralds the arrival of an atom by simultaneously turning the homodyne drive on and turning the heterodyne probe off. To make this triggering event clear, 5μs of the 'dead time' prior to the trigger is also included. In each plot, the x-axis spans a 55μs window, and the data has been scaled into units of $g_0/2\kappa$ (using 2.105 and the known cavity QED parameters). Note, the drive strength increases between each of the four plots such that the intracavity photon number *for an empty cavity* is, respectively, $\bar{n} = \{9, 20, 37, 109\}$. For the data displayed in this section the
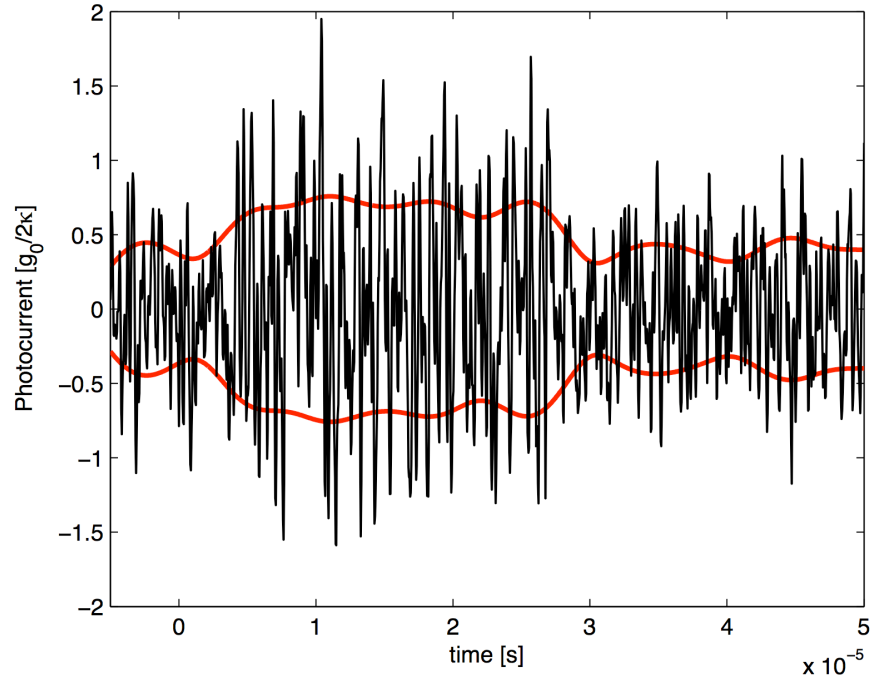
(a) $\bar{n} = 9$
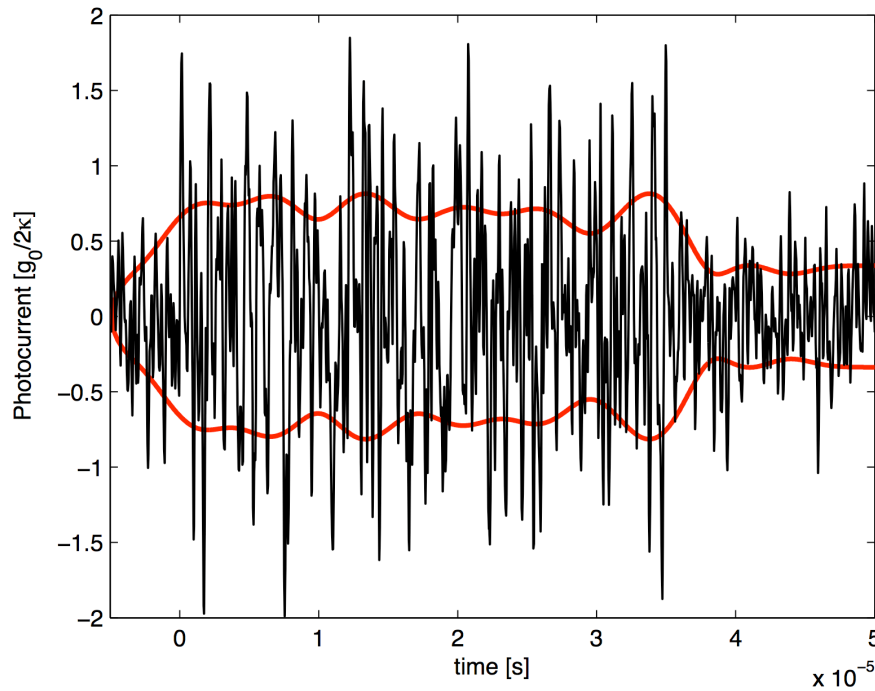
(b) $\bar{n} = 20$

Figure 2.22:   Triggered homodyne photocurrents for $\bar{n} = 9$ and 20. Both signals are displayed at an analog bandwidth of 100kHz-4MHz. The red curves show the photocurrent variance over time.
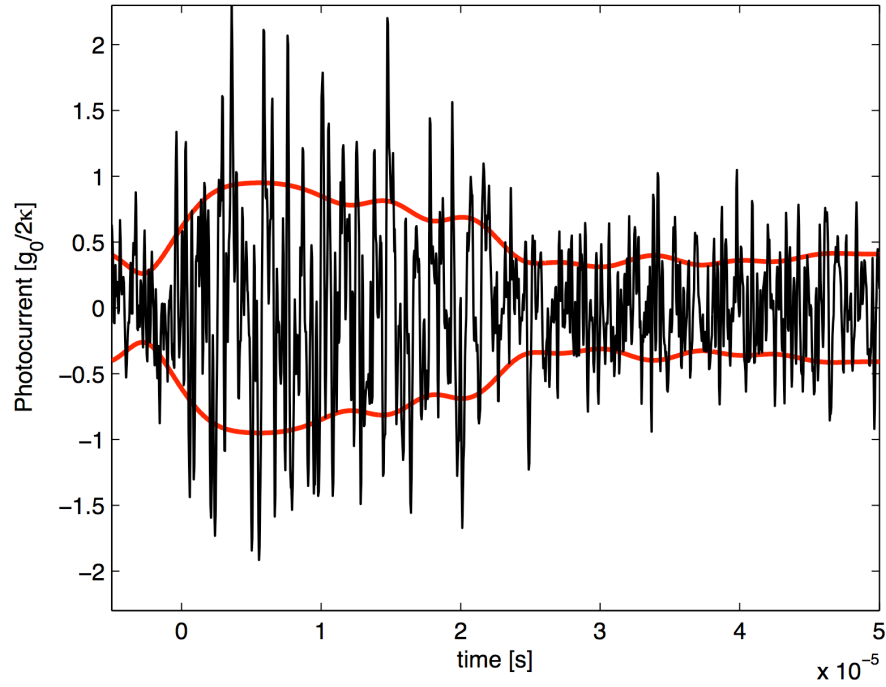
(a) $\bar{n} = 37$
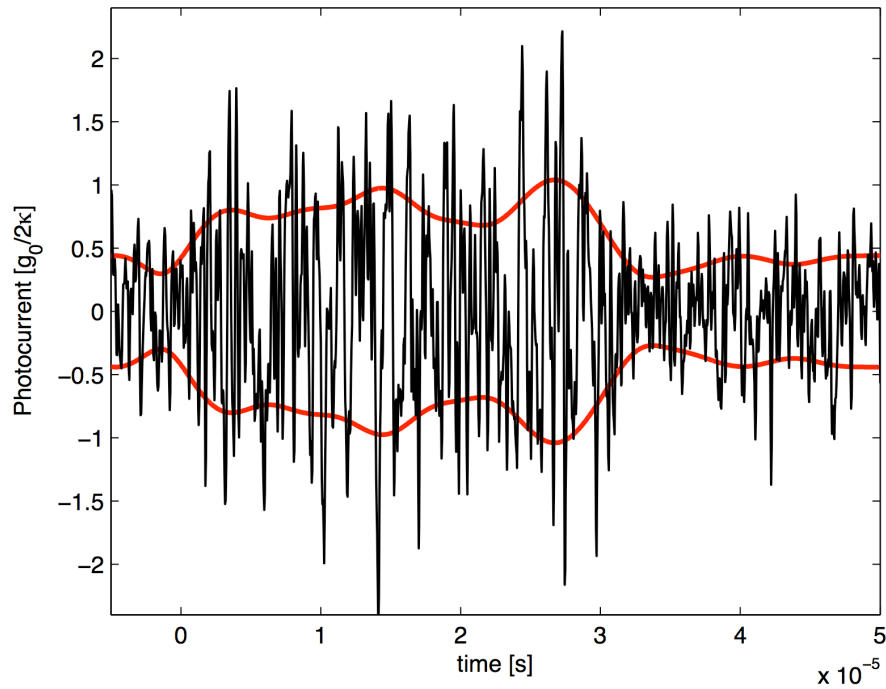
(b) $\bar{n} = 109$

Figure 2.23: Triggered homodyne photocurrents for $\bar{n} = 37$ and 109. Both signals are displayed at an analog bandwidth of 100kHz-4MHz. The red curves show the photocurrent variance over time.

probe strength is generally parametrized by the mean intracavity photon number that would be produced in an empty cavity; for $\bar{n} > 5$ the steady-state photon number with the atom present is $\sim \bar{n} - 1$, so that $\bar{n}$ is a good indicator of the mean photon number. As a point of comparison to the theory of Section 2.2, $\bar{n} = 9$ corresponds to $\mathcal{E} \approx 3g_0/2$, $\bar{n} = 20$ corresponds to $\mathcal{E} \approx 2g_0$, and so on with $\mathcal{E} \propto \bar{n}^{1/2}$.

The superimposed red curves represent the photocurrent standard deviation averaged in 2μs time windows. In each plot, the trigger event brings a period of increased photocurrent variation, typically lasting $\sim 25 - 35\mu$s, followed by a return to the shot noise level variance. In Figure 2.22b, for example, when the homodyne probe is turned on, the standard deviation jumps to ~ 0.75. It remains there until the atom abruptly disappears, at which point it returns to the shot noise level of ~ 0.35.

2.3.7.2   Optical pumping losses

These atoms disappear rather abruptly. For example, in Figures 2.22a, 2.22b, and 2.23b the photocurrent variance changes from a large and nearly constant value to the smaller shot noise level, in an almost step-like fashion. If the atom were simply moving through the Gaussian beam waist we would expect the photocurrent to smoothly decrease to the shot noise level. Only in Figure 2.23a does photocurrent variance decrease in this manner. In fact, the behavior displayed in Figure 2.23a is quite rare. Most of the homodyne photocurrent traces show precisely the opposite behavior: an atom, at the height of its coupling power, simply vanishes. Furthermore, the traces shown in Figures 2.22 and 2.23 are representative of the *longest* atom transits. Typically, the 'large variance' behavior is much shorter lived: for $10 \leq \bar{n} \leq 100$, the typical duration of this large variance behavior is only $\sim 10\mu$s; this problem is more pronounced as $\bar{n}$ grows, with many events lasting a duration $< 5\mu$s. This is significantly shorter than expected from the temporal width of typical heterodyne transit, for example, those of Figure 2.20.

The problem is optical pumping. For a linearly polarized field, the probe can always excite transitions from the $F = 4$ ground states to the $F' = 4$ excited states. For weak driving, however, this is hardly a problem: since the probe is nominally
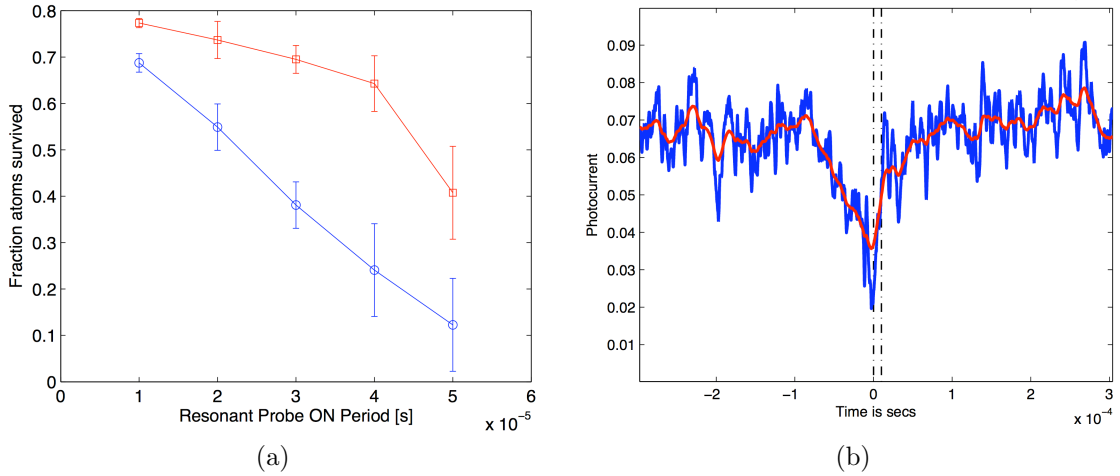
Figure 2.24: Measurement of optical pumping losses for a resonant probe with $\bar{n} = 50$. (a) Blue – fraction of atoms lost versus resonant probe duration. Red – same measurement but with a repumping field present. (b) A sample heterodyne transit with a resonant probe of 20μs duration turned on at $t = 0$ (duration denoted by dashed black vertical lines).

resonant with the $F = 4 \rightarrow F' = 5$ transition, the population of the $F' = 4$ states is largely suppressed by a ~ 250MHz detuning. However, as the Rabi frequency, $\Omega_r = \sqrt{\bar{n}}g_0/2$, approaches the magnitude of this detuning, the $F' = 4$ excited states become non-negligibly populated. These states can decay, via spontaneous emission, to the $F = 3$ ground state manifold, which is essentially decoupled from the rest of the system by a ~ 9GHz detuning.

Figure 2.24A shows evidence of this atomic loss mechanism is at work. The blue data points represent the fraction of atoms that survive interrogation by a resonant probe of mean photon number $\bar{n} \approx 50$. The duration, τ, of this resonant probe excitation is plotted along the x-axis for 10μs $\leq \tau \leq 50\mu$s. These measurements were performed using the same triggering procedure employed for acquisition of the phase quadrature homodyne photocurrents; this time, however, the heterodyne signal is kept on, and the resonant probe is only turned on for a predetermined duration. Figure 2.24B shows a representative heterodyne transit for the case of a 20μs resonant probe duration. The vertical dashed lines show the probe 'on' period. The data of Figure 2.24A was compiled by looking at transits similar to Figure 2.24B and

determining *by eye* whether the atom survived the encounter with the probe. Note, in the case of Figure 2.24B the atom is lost. The red data in Figure 2.24A represents the same measurement but with a repumping laser, resonant with the $F = 3 \rightarrow F' = 4$ transition, also exciting the cavity during the probing time. For short times, the presence of this repump laser largely suppresses atomic losses. For longer times the two measurements approach each other, since atoms are also lost because they simply fall through the mode. Also, the inferred error bars are $N^{1/2}$ deviations about the mean values, where N is the number of data points collected for each duration. I should point out that I don't have much faith in this data outside of its qualitative confirmation of optical pumping effects. Note, for example, that the slopes of these data do not appear to extrapolate to one for a probe of zero duration. Also, the decay does not appear to be exponential, as it should.

2.3.7.3 Single-shot analysis

A major technical limitation to the experiment is that all of the acquired data was sampled at an analog-to-digital conversion rate of 2.5×10^7 samples per second. This implies a maximum analog bandwidth of ≈ 12 MHz that is dangerously close to expected phase switching rate, $\gamma_\perp/2 \approx 8$MHz. Nevertheless, it is possible to utilize standard techniques for hidden Markov models to attempt to reconstruct two-state switching trajectories from individual photocurrent records. Figure 2.25a displays a homodyne photocurrent for $\bar{n} = 56$ intracavity photons. Note, the scale on the y-axis is the same as Figure 2.23b and the data is presented at an analog bandwidth of 4MHz. In this case the atom remains in the cavity until $t \approx 25\mu$s when, at the height of its coupling potential, it disappears. Figure 2.25b displays a zoomed in look at the final $\sim 12\mu$s of the transit, at a full analog bandwidth of 11MHz. The superimposed solid red curve is a reconstruction of the system's switching behavior using a hidden Markov model with posterior decoding to infer the underlying state sequence [93]. This analysis was provided by Dmitri Pavlichin. The model assumes that the system is jumping between hidden states, and attempts to reconstruct the state switching sequence through knowledge of the system's output channel (*i.e.*,
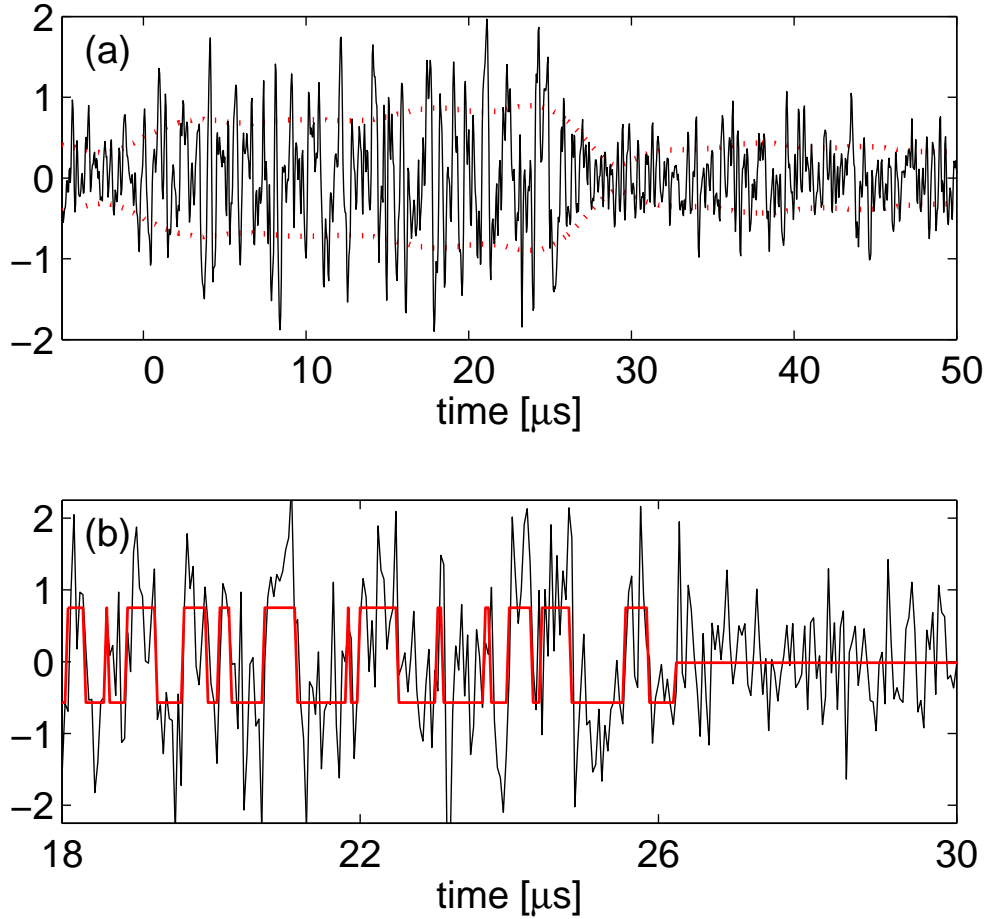
Figure 2.25: A) A phase bistability trajectory for an empty cavity photon number $\bar{n} = 56$. The displayed bandwidth is 4MHz. The red curve shows the photocurrent variance over time. B) A hidden Markov model reconstruction of switching behavior assuming three underlying states (provided by D. Pavlichin). The data is fit and displayed at full bandwidth.

the homodyne photocurrent). For this particular model, there are three internal system states; an initial guess is provided for the switching rates between the three states, and the Baum-Welch algorithm [93] is then used to train the inferred switching rates and the field values for each state. Remarkably, over the duration of the atom transit the model hops between high and low states, but shortly after $t = 26\mu$s it chooses the middle state. Furthermore, the trained switching rate, averaged over many trajectories, is ≈ 6MHz, which is within 30% of $\gamma_\perp/2$.
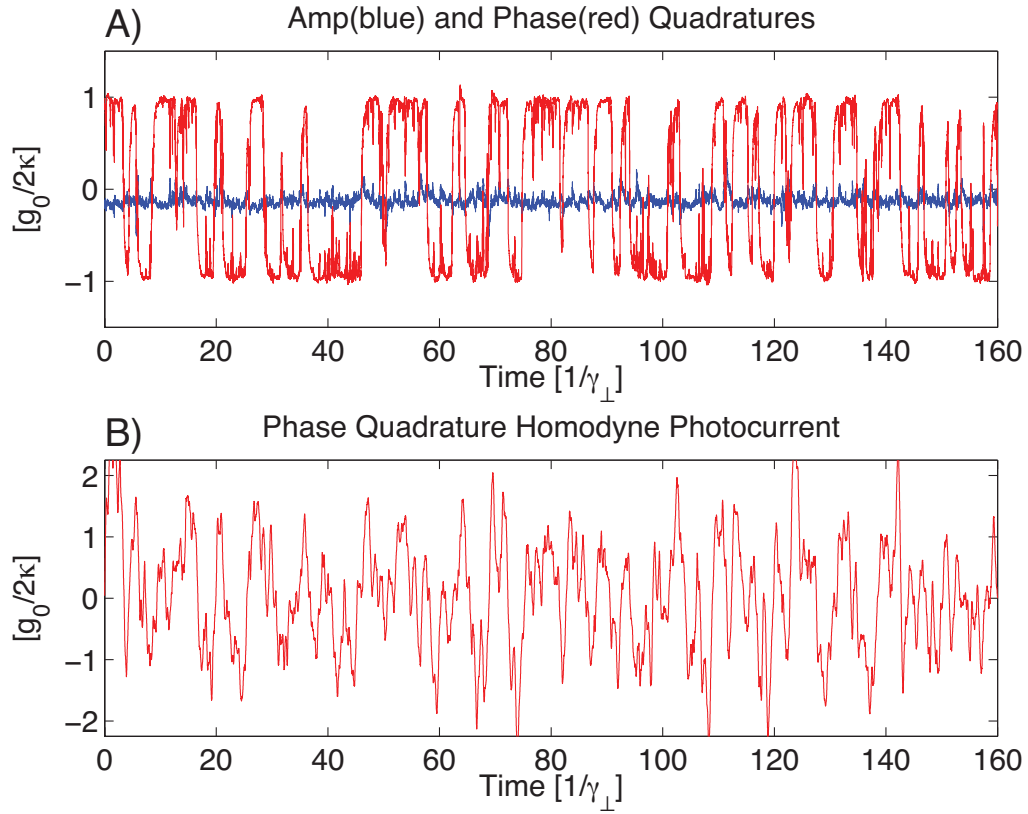
Figure 2.26: A quantum trajectory with a simulated phase quadrature homodyne photocurrent that accounts for the experimental measurement efficiency and the maximum analog bandwidth, 11MHz. Note, the x-axis scale correspond to $\approx 10\mu s$. A) The phase (red) and amplitude (blue) quadratures. B) The simulated phase quadrature photocurrent.

Clearly these data do not look like the nice theoretical trajectories plotted in Figures 2.7 and 2.9. Figure 2.26 displays a 'realistic' simulation in which the experimental efficiency and maximum analog bandwidth are accounted for. The x-axis spans a total time $\sim 10\mu s$. Dare I say, the resemblance of this simulated photocurrent to the data of 2.25B is haunting. Note, as a consequence of the low analog bandwidth, this simulated photocurrent tends to 'miss' jumps in the phase quadrature field. For example, near the end of the simulation the phase quadrature, shown in 2.26A, jumps between the high and low field values fairly rapidly; the photocurrent, however, reflects a low-passed version of this behavior, with but a small offset from zero reflecting the average phase quadrature amplitude over this time period.

2.3.7.4 Statistical analysis of the data

The modest signal-to-noise ratio of these measurements limits the amount of insight that can be gained through analysis of single-shot homodyne photocurrents. Sadly, we now turn to statistical analysis applied to the experimental data set. For the analysis described below, the data set was compiled by selecting out regions of the homodyne photocurrent where the phase fluctuations were largest. This way, we can compare the data to theoretical predictions that assume a maximal atom-field coupling, $g_0 = 2\pi \cdot 16$ MHz, and thereby sidestep *most* complications due to atomic motion within the cavity mode. This process of data selection was performed by eye, primarily to avoid accidental contamination of the data set with homodyne photocurrent event where the heterodyne fringe was unlocked. Such events are rare, but they do occur. Typically, these snippets of data are only $\lesssim 10\mu$s in duration, although for longer events, like those in Figures 2.22, longer time windows are chosen. For each value of $\bar{n}$, approximately 50 atom transits were inspected for regions of large phase fluctuations.

Histograms of these compiled data sets are displayed in Figure 2.27. The three rows of plotted histograms correspond to three choices of analog filtering bandwidth: in plot 2.27a the data is not filtered (beyond an analog anti-aliasing filter at 11MHz); in 2.27b the data is digitally filtered to 8MHz; and in 2.27c the data is digitally filtered to 2MHz. In addition, all data are first AC filtered at 200kHz to removed slow drifts in the homodyne fringe level that are caused by imperfections in the heterodyne servo lock. All histograms are normalized such that they integrate to unity, but note that the x-axis scale changes between the different filtering bandwidths. In general, the photocurrent distributions widen with increasing $\bar{n}$, although they do not possess any clear bimodal features. Note, however, that for large large $\bar{n}$, the 8MHz bandwidth histograms reveal a non-Gaussian distribution. In particular, for $\bar{n} = 56$ the histogram is distinctly flat-topped.

Superimposed on these histograms are theoretical predictions generated through quantum trajectory simulations for the experimental parameters. The simulated photocurrent, Eq. 2.75, is generated assuming a detection efficiency $\eta_\kappa = (\eta_L \eta_H)^2 \eta_T$,

(a) Full bandwidth (11MHz)

(b) 8MHz bandwidth
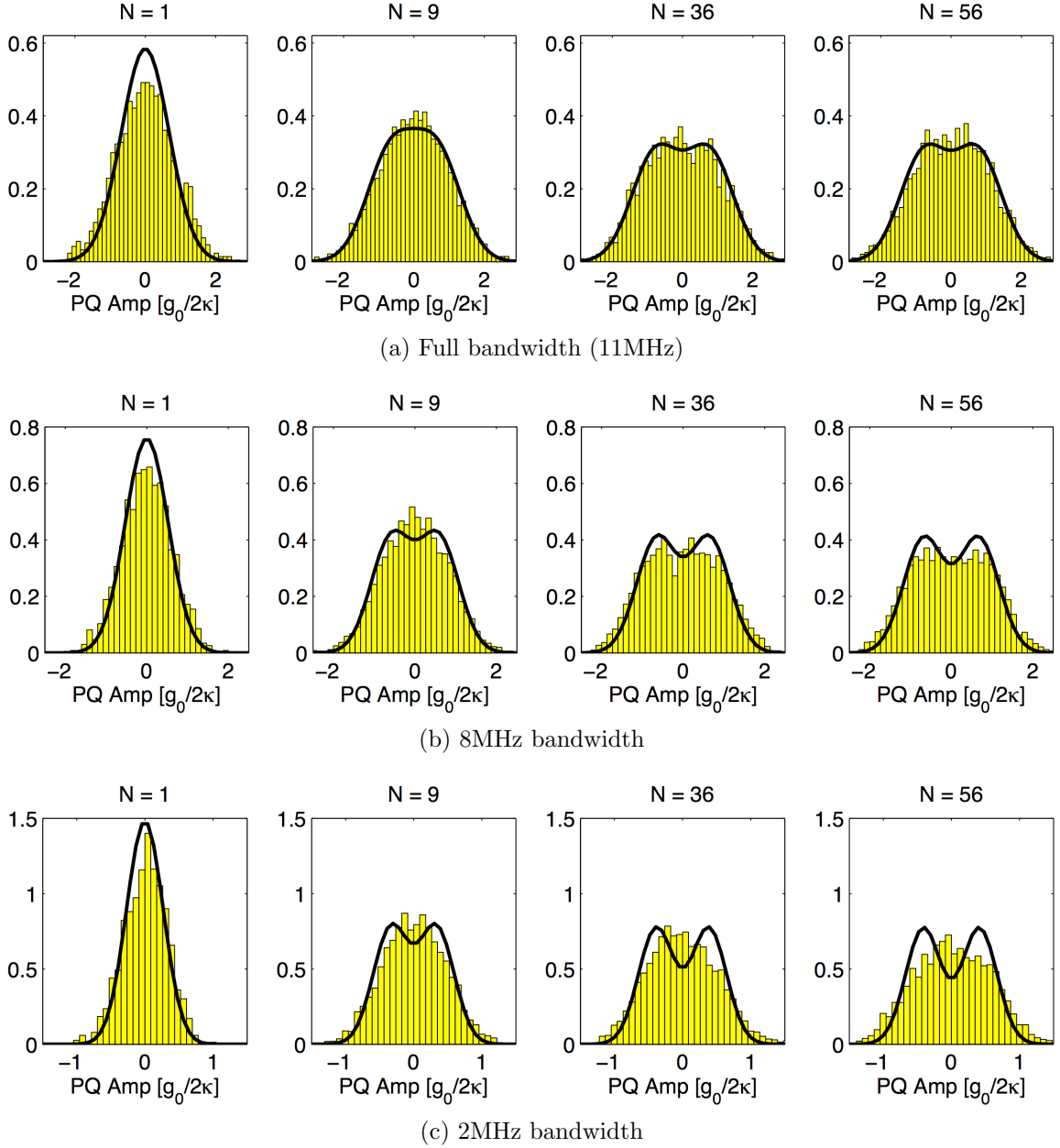
(c) 2MHz bandwidth

Figure 2.27: Photocurrent histograms and theoretical distribution for four values of $\bar{n}$. The analog filtering bandwidth for each row is: (a) 11MHz (set by the anti-aliasing filter); (b) 8MHz; (c) 2MHz..

which follows from the analysis of Section 2.3.5. The black curves in Figure 2.27 are then obtained as follows. The simulated photocurrents are digitally filtered and histograms are constructed by the same procedure used on the experimental data. These trajectory histograms are then fit with a (one-dimensional) double-Gaussian distribution, but with the standard deviation of each Gaussian constrained to one. There

are three fit parameters: the separation between Gaussian peaks, and the height of each peak. The displayed curves are these double-Gaussian fits. It should be noted, however, that because $\gamma_\perp$ is finite, the *expected* width of each bimodal peak is actually larger than one. That is, even in theory, the width of the two 'coherent-ish' states that comprise the bimodal Q-function for large $\bar{n}$ have additional noise due to spontaneous emission. For reasons of consistency that will become evident shortly, we fit the trajectories using this idealized width (*i.e.*, one, for coherent states). In going from full bandwidth to 2MHz, these theoretical distributions gain a more pronounced bimodal shape for large $\bar{n}$. This filtering effect can be understood as elimination of high frequency shot noise (dW in Eq. 2.75) that is outside of the relevant dynamical range set by $\gamma_\perp/2 \approx 8$MHz. Note, though, that the quality of this fit *to the simulated photocurrent* rapidly declines for lower high frequency cut-offs, since the rapid switching behavior will be averaged to zero. At 2MHz bandwidth, for example, the actual simulated distribution does not possess the bimodal shape indicated by the fit (however, for 8MHz the fit is still excellent).

The agreement between the data and the theoretical predictions is quite good at full bandwidth and 8MHz. In particular, for large $\bar{n}$ the widths of these experimental distributions are very well fit by the simulations. In general, however, the experimental distributions possess slightly fatter tails. There are two reasons for this. First, there is the problem of broadening due to a finite $\gamma_\perp$, as discussed above (this is also the cause of the poor fits for $\bar{n} = 1$.) Second, there is a contribution of low-frequency (*i.e.*, $1/f$) noise due to variations in the homodyne fringe level that are not entirely eliminated through the AC filtering. This effect is particularly pronounced in the 4MHz bandwidth data, since the lower frequencies now contribute a large fraction of the total bandwidth.

The bigger problem with these experimental histograms is that they are singly peaked. In general, the large $\bar{n}$ photocurrent histograms have more weight at zero than predicted by theory. No systematic attempt has been made to pinpoint the source of this problem, but the following are possible contributors. One likely candidate is atomic motion through the standing wave structure of the cavity. Motion through

a cavity node has the effect of 'resetting' the atomic dressed-state, as discussed in Section 2.1.2.2. This process leads to an effective increase of the phase switching rate. For a fixed bandwidth, then, more switching events will be averaged to zero, as discussed in regards to Figure 2.26. Furthermore, because of the low sampling rate, this problem could be even more pronounced. This explanation is somewhat questionable, however, since the overall width of these histograms does match the theory quite well. If atomic motion through the standing wave is problematic, then we should also see an effective reduction in the size of the coupling strength, which we do not. Another contributor to this single peaked-ness is the use of a linearly polarized cavity mode. In particular, the cavity supports an orthogonal (nominally unexcited) mode that the atoms are also coupled to, as discussed in Section 2.3.1.5. The presence of this mode and the multilevel nature of the atoms leads to a small reduction of the mode splitting. Finally, excess low frequency phase noise, from a great many conceivable sources, could smear out the underlying bimodal distribution.

Figure 2.28 is a summarized comparison between the experimental photocurrent distributions and theoretical predictions over a range of intracavity photon numbers. The data points represent the mode-splitting obtained from double-Gaussian fits to the experimental photocurrents. These experimental fits are performed with the same procedure outlined above, but with the standard deviation of each Gaussian constrained by the width of the *measured* shot noise distribution. The values plotted at each $\bar{n}$ are the centroids for the fit. The theoretical mode splitting is obtained by fitting a double-Gaussian to simulated photocurrents, as described above. In order to avoid cluttering the figure, I plot a smoothed fit through the theoretical mode splitting data points so obtained. In general the trajectory simulations fit the data quite well, particularly for smaller bandwidths. Not too much should be inferred from this trend though: with increased filtering both theoretical and experimental fluctuations tend to zero. Also displayed is the mode splitting predicted by the steady-state Q-function (dotted black curve). For large $\bar{n}$, this curve matches up quite nicely with the full bandwidth quantum trajectory splitting. To obtain this curve, the Q-functions were
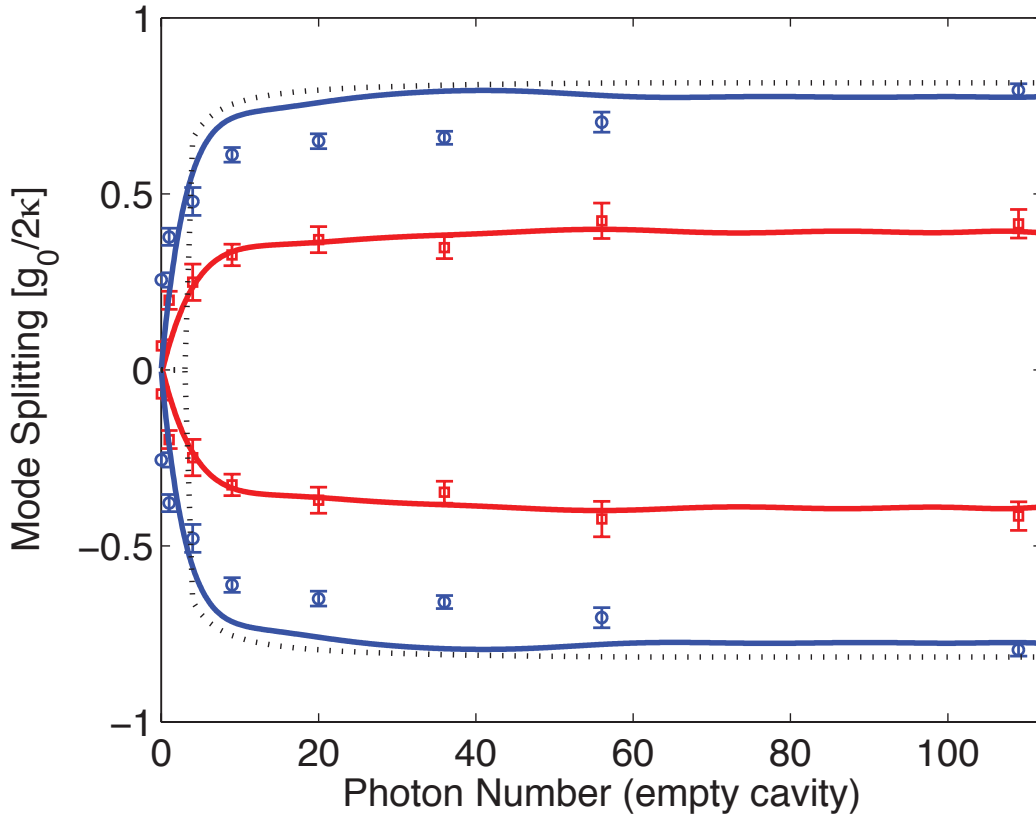
Figure 2.28: Comparison of experimental mode splitting to theoretical predictions for: 11MHz bandwidth (blue) and 2MHz (red). Data points represent experimental data whereas solid lines are quantum trajectory simulations. The dotted black curve is a represents the best fit centroid to steady-state Q-functions (similar to the ones plotted in Figure 2.13.)

also fit with a double Gaussian distributions. In this case, however, the width of the underlying Gaussians was also fit. The reason for this, as discussed earlier, is that the width of the underlying modes differ from the coherent state value of one because of spontaneous emission effects. Note that even the ideal Q-function splitting is less than $\pm g_0/2\kappa$. This is due to the modest size of the ratio $g_0/2\kappa \approx 1$.

Finally, in order to provide a dynamical comparison between the data and theory, we turn to autocorrelation functions. Figure 2.29 displays autocorrelation functions of the experimental photocurrent for a range of photon numbers (denoted in the legend). Before computing these autocorrelations, the data was AC filtered at 100kHz, to eliminate systematic offsets caused by low frequency fringe fluctuations. The theoretical
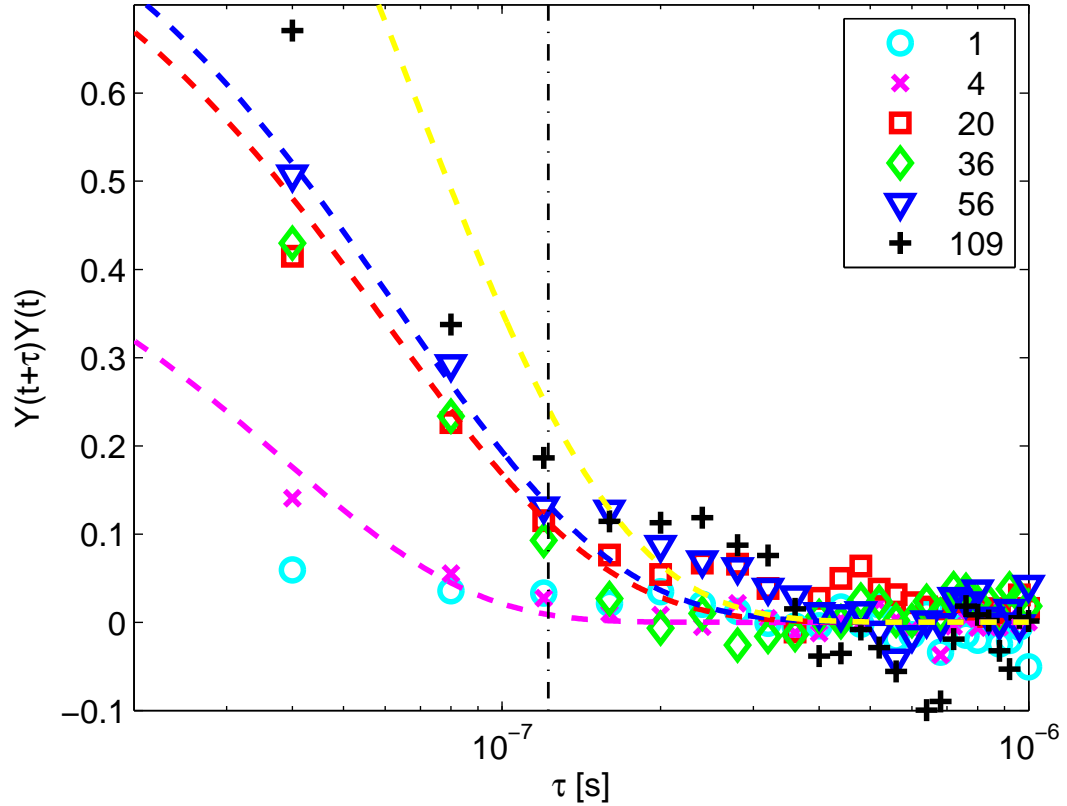
Figure 2.29: Comparison between photocurrent autocorrelations and theoretical predictions. The mean photon number is denoted in the legend. The dashed curves are theoretical predictions from the master equation. The vertical dashed line indicates the predicted average period between switching events, $2/\gamma_\perp$. As a point of contrast, the theoretical prediction for $g_0 = 2\pi \cdot 22\text{MHz}$ and $\bar{n} = 50$ is plotted in yellow.

curves are the expectations $\langle \hat{Y}(t + \tau)\hat{Y}(t)\rangle$ generated from the master equation 2.24 using the quantum regression theorem [44]. The vertical dashed line indicates the predicted average period between switching events, $2/\gamma_\perp$. For $1 \leq \bar{n} \leq 56$ the data matches up nicely with the theory, although it generally lies slightly lower than predicted. This could be due to a minor miscalibration of one of the scaling factors used in Eq. 2.105 to convert the experimental photocurrent into 'theory units'. This discrepancy could also be understood from a minor reduction in the effective coupling rate g_0, caused by atomic motion, for example. In either case the discrepancy is quite small since the autocorrelations are quadratic in these calibration factors. As a point of contrast, the theoretical prediction for $\bar{n} = 50$ and $g_0 = 2\pi \cdot 22\text{MHz}$ is plotted in

yellow. The slope of this curve differs significantly from the $\bar{n} \approx 56$ data. In fact, a ten percent decrease in the total calibration factor is all that is implied – such a change would go largely unnoticed in the mode-splitting analysis of Figure 2.28. Finally, the $\bar{n} = 109$ data lies *above* the theory. As discussed in Section 2.3.5, for this probe strength there is a noticeable increase in the phase-quadrature homodyne fringe noise, particularly around 500kHz. This excess phase noise is the most likely reason why the $\bar{n} = 109$ autocorrelation in Figure 2.29 is so large for small τ.

2.3.7.5 Photocurrent signals for a detuned atom

To further confirm that the photocurrent fluctuations were indeed related to atomic dressed state fluctuations, measurements were made with the cavity and probe detuned with respect to the atom. Specifically, the probe strength and detuning relative to the cavity were fixed such that, $\bar{n} = 20$ and $\Theta = 0$, but also detuned from the atoms by $\Delta/2\pi = \pm 40$MHz. For a nonzero Δ, the atomic state preferentially localizes on one of the two dressed states. Consequently, the steady-state cavity field distribution is no longer symmetric in phase. This effect is shown in Figure 2.30, where we plot the Q-function and simulated phase-quadrature photocurrent for $\bar{n} = 20$, $\Theta = 0$, and with $\Delta/2\pi = \{-40, 0, 40\}$MHz for the three rows. The simulated photocurrents are displayed at 11MHz bandwidth, but assuming perfect detection efficiency so that the effect can be clearly seen.

The experimental utility of working in this parameter regime is that this Δ-dependent offset in the phase quadrature signal can be verified through a lower bandwidth measurement. Furthermore, because of our limited digital-to-analog conversion rate, this effect should be more easy to see than phase switching at $\gamma_\perp/2$. Figure 2.31 shows two examples of measured homodyne photocurrents for this parameter set. The upper trace is for $\Delta/2\pi = +40$MHz and the lower trace is for $\Delta/2\pi = -40$MHz. In both cases, the atom transit, lasting approximately 25μs, brings an overall phase shift in the homodyne fringe, with the sign of this shift correlated with Δ. The display bandwidth, 20kHz-4Mhz, is chosen so that this effect is clearly visible to the eye. Note that because of an overall π-phase shift in the electronic photocurrent gain, the
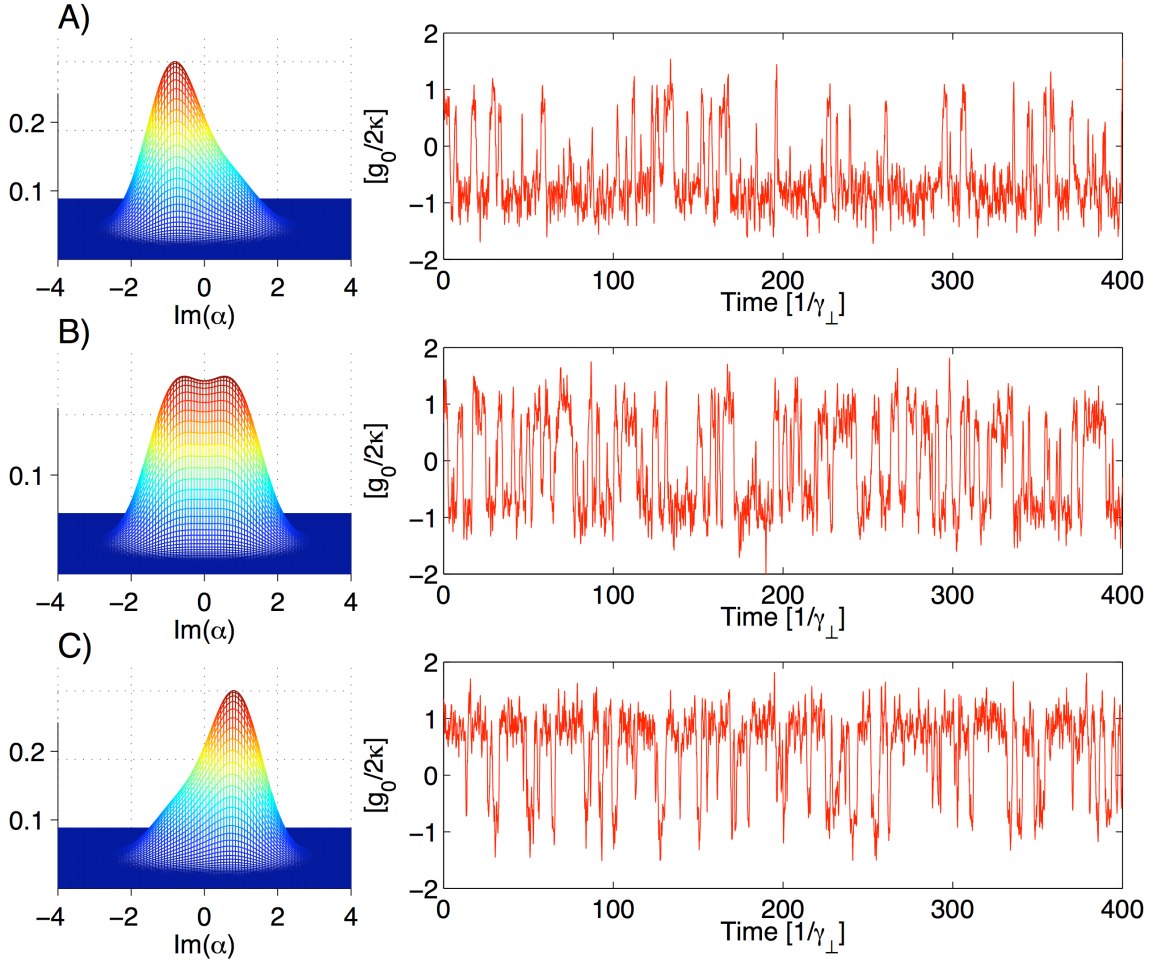
Figure 2.30: Steady-state Q-functions and simulated homodyne photocurrents for different atomic detunings, and $\bar{n} = 20$. The photocurrents are displayed at 11MHz bandwidth, and assuming perfect detection efficiency. The x-axis scale corresponds to about 25μs. A) $\Delta = -40$MHz; B) $\Delta = 0$MHz; C) $\Delta = +40$MHz.

sign of these signals is flipped relative to the quantum trajectory simulations above. Qualitatively, both signals match up nicely with the predictions in Figure 2.30A and C, aside from some low frequency noise. This noise is visible for these traces because of the conservative choice of AC filtering at 20kHz, which is necessary to preserve the size of the atom-induced phase shift.

Histograms of data taken in this parameter regime are displayed in Figure 2.32. This data was compiled using the same procedure described above with regards to the resonant histograms. In Figure 2.32, the black curves are simply double-Gaussian fits to the histograms with the standard deviation constrained by the measured pho-
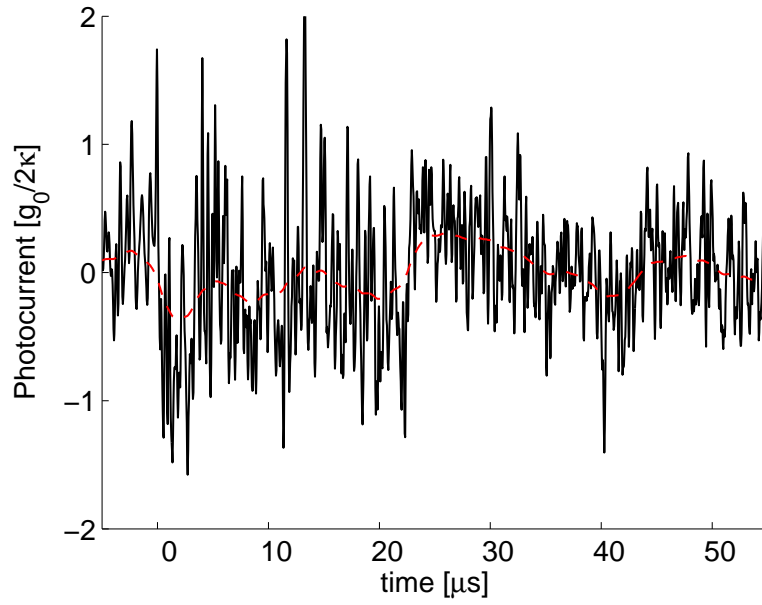
(a) $\{\Delta, \Theta\} / 2\pi = \{40, 0\}$MHz
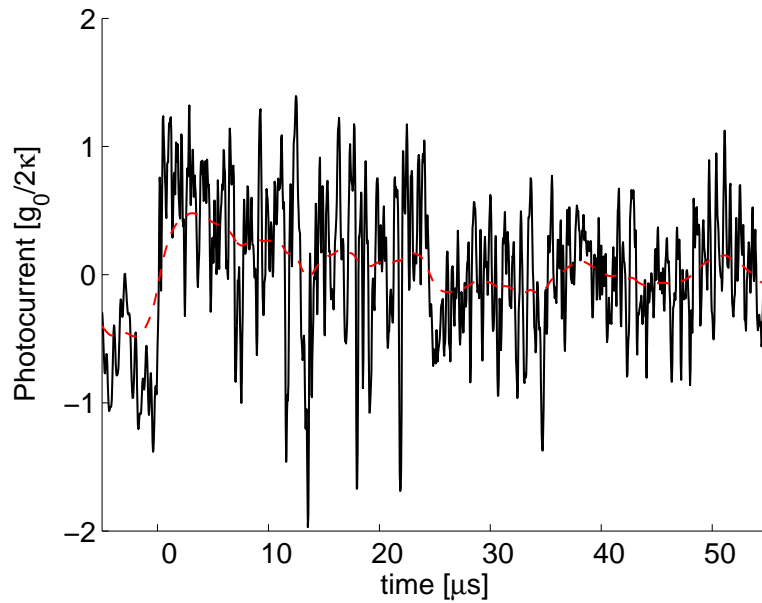
(b) $\{\Delta, \Theta\} / 2\pi = \{-40, 0\}$MHz

Figure 2.31: Phase quadrature homodyne signals for a detuned atom. Data is displayed in an analog bandwidth of 20kHz to 4MHz. The dashed red curve is the photocurrent low pass filtered at 100kHz. (a) $\{\Delta, \Theta\} / 2\pi = \{40, 0\}$MHz. (b) $\{\Delta, \Theta\} / 2\pi = \{-40, 0\}$MHz. Note, because of an overall π-phase shift in the electronic gain, there is a sign difference between this data and the simulated photocurrents in 2.30.
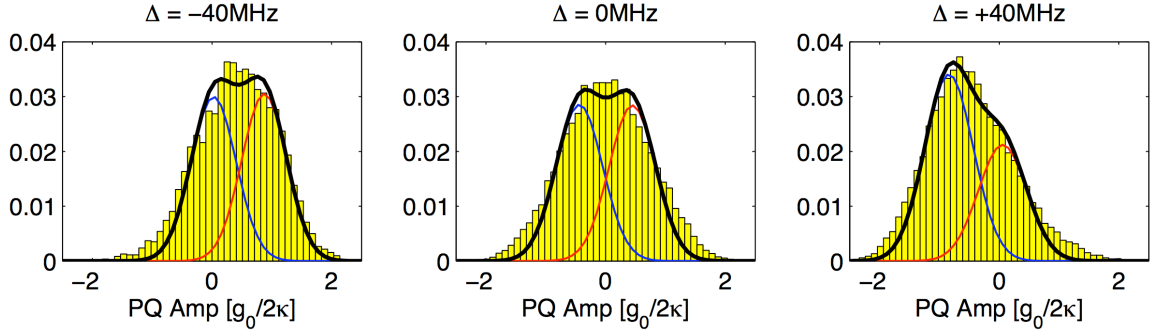
Figure 2.32: Photocurrent histograms for three different Δ. The black curves are double Gaussian fits to the distributions, with the width of the underlying Gaussians set by the measured shot noise. The analog filtering bandwidth is 20kHz-4MHz.

tocurrent (the red and blue curves are the underlying Gaussians). In moving from the $\Delta/2\pi = -40$MHz to the $\Delta/2\pi = +40$MHz data, there is a clear shift in the weight of the distribution from positive to negative phase. The $\Delta/2\pi = -40$MHz histogram, however, possesses significantly more weight at zero than the $\Delta/2\pi = +40$MHz histogram. The cause of this is most likely the large average repulsive force felt by the atom for this detuning, as discussed in Section 2.1.2.2. This repulsive force simultaneously channels atoms axially towards optical field nodes and repels them radially out of the cavity; the result is a reduction in the effective atom-field coupling strength. For $\Delta/2\pi = +40$MHz, however, the atom is actually bound to the cavity mode, and is, in general, funneled into regions of strong coupling. It should be noted that atomic transits of the length displayed in Figure 2.31B are *extremely* rare for $\Delta < 0$ case. In fact, they are so rare that the $\Delta/2\pi = -40$MHz plot presented here is literally the only atom transit for this detuning that lasted longer than $\sim 10\mu$s. For $\Delta/2\pi = +40$MHz, however, there are many examples that are as long as the one displayed in Figure 2.31A.

Finally, a comparison between experimental and theoretical autocorrelations for different Δ is shown in Figure 2.33. Before computing these autocorrelations, the data is AC filtered at 20kHz, to eliminate systematic offsets caused by low frequency fringe fluctuations while preserving the effects of atom-induced phase shifts. This particular choice was determined by choosing the lowest AC filter frequency such that the $\Delta = 0$ autocorrelation lined up (at zero value) with theory for large τ.
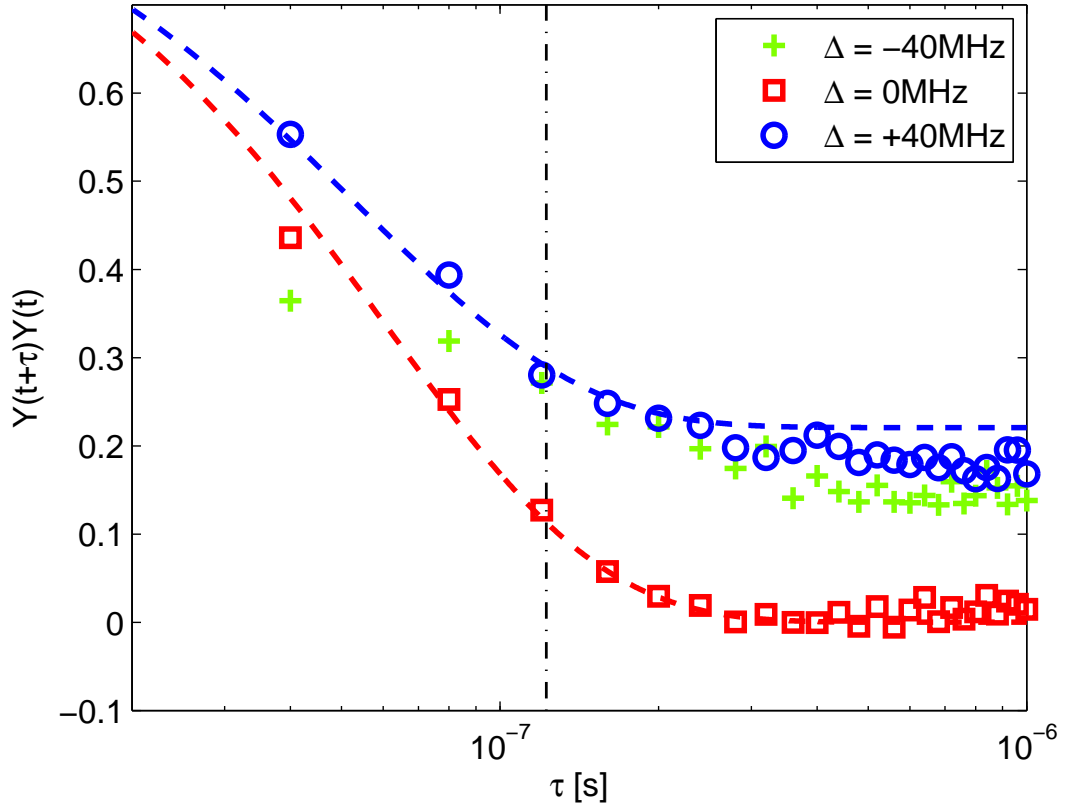
Figure 2.33: Photocurrent autocorrelations and theoretical predictions for $\bar{n} = 20$ and different atomic detunings. The signals are first AC filtered at 20kHz. The plot parameters are denoted in the legend. The dashed curves are theoretical predictions from the master equation. The vertical dashed line indicates the expected average period between switching events for $\Delta = 0$.

The vertical dashed line indicates the predicted average period between switching events, $2/\gamma_\perp$, for the case $\Delta = 0$. The theoretical curves are again computed from the master equation 2.24 using the quantum regression theorem. The plateau in the $\Delta/2\pi = +40$MHz autocorrelation reflects the nonzero average phase quadrature signal. The $\Delta/2\pi = -40$MHz data does not follow the expected theoretical trend very well. This is, again, most likely due to the repulsive forces acting on the atom in this case – these forces lead to a reduction in the average coupling strength. Furthermore, the statistics for this data are quite poor, as few atomic transit events of length $\gtrsim 5\mu$s were observed.

Chapter 3

Bifurcations and bistability in cavity QED

3.1 Introduction

My principal aims in this chapter are to illustrate a systematic approach (building upon Refs. [31, 32]) to expanding the known inventory of bifurcation-type phenomena in single-atom cavity QED, and to highlight some conspicuous predictions of the fully quantum model as compared to the semiclassical Maxwell-Bloch Equations. In so doing I hope to begin to illumine a more comprehensive picture of the quantum-classical transition in cavity nonlinear optics [21, 94], bridging what is generally known about linear-gaussian [95] and chaotic [96] open quantum systems [97]. While previous theoretical [4, 43, 98] and experimental [99] investigations of single-atom bistability have largely focused on steady-state observables of the transmitted optical field, I will here follow the spirit of Refs. [3, 100] in studying transient signals and stochastic jumps observable in the broadband photocurrent generated in individual experimental trials. I look in particular at a case of absorptive bistability, a supercritical Hopf bifurcation, and a subcritical Hopf bifurcation, all of which occur with mean intracavity photon numbers of order ten.

3.2 The master equation revisited

In Chapter 2, a simple version of the cavity QED master equation was presented that was adequate for the discussion of phase bistability. In particular, non-radiative dephasing and multiple-atom couplings were not considered. Here, I introduce a form of the master equation appropriate for more general system behavior. Using this new description I derive a form of the Maxwell-Bloch equations more amenable to numerical and analytical analysis. Note, in this chapter, I break with the convention (of Chapters 1 and 2) of denoting quantum mechanical operators with a 'hat'. I do this to simplify otherwise cluttered expressions.

3.2.1 Quantum dynamical description

We consider the driven Jaynes-Cummings Hamiltonian [6] which models the interaction of a single mode of an optical cavity having resonant frequency ω_c, with a two-level atom, comprised of a ground state $|g\rangle$ and an excited state $|e\rangle$ separated by a frequency ω_a. For an atom-field coupling constant g_0 and a drive field amplitude $\mathcal{E}$, the Hamiltonian written in a frame rotating at the drive frequency ω_l is given by [$\hbar = 1$]:

$$\mathcal{H} = \Theta a^\dagger a + \Delta \sigma_+ \sigma_- + i g_0 (a^\dagger \sigma_- - a \sigma_+) + i \mathcal{E}(a^\dagger - a) , \qquad (3.1)$$

where $\Delta = \omega_a - \omega_l$ and $\Theta = \omega_c - \omega_l$. In Eq. 3.1, a is the field annihilation operator and $\sigma_- = |g\rangle\langle e|$ is the atomic lowering operator. In addition to the coherent dynamics governed by 3.1 there are two dissipative channels for the system: the atom may spontaneously emit into modes other than the preferred cavity mode, at a rate $\gamma_\parallel$, and photons may pass through the cavity output coupling mirror, at a rate 2κ. Furthermore, we model the case of non-radiative dephasing (at rate γ_{nr}) between the atomic ground and excited states. In the analysis to follow, we will be concentrating solely on the situation where $\gamma_{nr} = 0$, *i.e.*, purely radiative damping; however, γ_{nr} is included here to indicate that we are not restricted to this case (in particular, the parameterization employed in section 3.3 will imply a variable dephasing.) The un-

conditional master equation describing this driven, damped, and dephased evolution is

$$
\begin{aligned}
\dot{\rho} &= -i[\mathcal{H}, \rho] + \kappa(2a\rho a^\dagger - a^\dagger a\rho - \rho a^\dagger a) \\
&+ \gamma_\parallel/2(2\sigma_-\rho\sigma_+ - \sigma_+\sigma_-\rho - \rho\sigma_+\sigma_-) \\
&+ \gamma_{nr}/2(\sigma_z\rho\sigma_z - \rho)
\end{aligned}
\tag{3.2}
$$

where $\sigma_z = [\sigma_+, \sigma_-]$ measures the population difference between the excited and ground states.

While g_0 measures the coherent coupling rate between the atom and the cavity, the rates $\gamma_\parallel$, γ_{nr}, and κ characterize processes which tend to inhibit the build up of coherence. The qualitative nature of the dynamics 3.2 may be determined by two dimensionless parameters which measure the relative strengths of the coherent and incoherent processes: the critical photon number

$$
n_0 = \frac{\gamma_\parallel \gamma_\perp}{4g_0^2} \; ,
\tag{3.3}
$$

and the critical atom number

$$
N_0 = \frac{2\gamma_\perp \kappa}{g_0^2} \; ,
\tag{3.4}
$$

where $\gamma_\perp$ is the transverse relaxation rate given by $\gamma_\perp = \gamma_\parallel/2 + \gamma_{nr}$. The critical photon number provides a measure of the number of photons needed to saturate the response of a single atom, and in the regime $n_0 < 1$ a single photon inside the resonator can induce a nonlinear system response. Similarly, the critical atom number roughly quantifies the number of atoms required to drastically change the resonant properties of the cavity. When $N_0 < 1$, a single atom inserted into the cavity will have a dramatic effect on the cavity output. The so-called "strong coupling regime" of cavity QED, which is usually used to denote the regime where the coherent coupling dominates over dissipation, is reached when the condition $(n_0, N_0) < 1$ holds.

The master equation 3.2 may be used to find the time evolution for any operator acting on the system Hilbert space. In particular, it will be useful to know the

dynamical equations for $\langle a \rangle$, $\langle \sigma_- \rangle$, and $\langle \sigma_z \rangle$ in order to make concrete comparisons with the semiclassical results that follow. Using the fact that $\langle \dot{O} \rangle = \text{Tr}[O\dot{\rho}]$ for a system operator O, we obtain

$$
\begin{aligned}
\langle \dot{a} \rangle &= -\kappa(1 + i\theta)\langle a \rangle + g_0\langle \sigma_- \rangle + \mathcal{E} \\
\langle \dot{\sigma}_- \rangle &= -\gamma_\perp(1 + i\Lambda)\langle \sigma_- \rangle + g_0\langle a\sigma_z \rangle \\
\langle \dot{\sigma}_z \rangle &= -\gamma_\parallel(\langle \sigma_z \rangle + 1) - 2g_0(\langle a^\dagger \sigma_- \rangle + \langle \sigma_+ a \rangle) \,,
\end{aligned}
\tag{3.5}
$$

with $\gamma_\perp = \gamma_\parallel/2 + \gamma_{nr}$, $\theta = (\omega_c - \omega_l)/\kappa$, and $\Lambda = (\omega_a - \omega_l)/\gamma_\perp$.

It should be noted that these formulae may be easily generalized to the case of N non-interacting atoms each coupled to the same mode of the electromagnetic field, with coupling constant g_0. In this case, the Hamiltonian becomes

$$
\mathcal{H} = \Theta a^\dagger a + \sum_{j=1}^{N} \Delta \sigma_+^j \sigma_-^j + \sum_{j=1}^{N} ig_0(a^\dagger \sigma_-^j - a\sigma_+^j) + i\mathcal{E}(a^\dagger - a) \,,
\tag{3.6}
$$

and the new master equation is

$$
\begin{aligned}
\dot{\rho} &= -i[\mathcal{H}, \rho] + \kappa(2a\rho a^\dagger - a^\dagger a\rho - \rho a^\dagger a) \\
&\quad + \gamma_\parallel/2 \sum_{j=1}^{N}(2\sigma_-^j \rho \sigma_+^j - \sigma_+^j \sigma_-^j \rho - \rho \sigma_+^j \sigma_-^j) \\
&\quad + \gamma_{nr}/2 \sum_{j=1}^{N}(\sigma_z^j \rho \sigma_z^j - \rho) \,,
\end{aligned}
\tag{3.7}
$$

where σ_-^j is the lowering operator for the jth atom and $[\sigma_+^j, \sigma_-^k] = \delta_{jk}\sigma_z^j$. The equations of motion for the operator expectations become

$$
\begin{aligned}
\langle \dot{a} \rangle &= -\kappa(1 + i\theta)\langle a \rangle + g_0 \sum_{j=1}^{N}\langle \sigma_-^j \rangle + \mathcal{E} \\
\langle \dot{\sigma}_-^j \rangle &= -\gamma_\perp(1 + i\Lambda)\langle \sigma_-^j \rangle + g_0\langle a\sigma_z^j \rangle \\
\langle \dot{\sigma}_z^j \rangle &= -\gamma_\parallel(\langle \sigma_z^j \rangle + 1) - 2g_0(\langle a^\dagger \sigma_-^j \rangle + \langle \sigma_+^j a \rangle) \,.
\end{aligned}
\tag{3.8}
$$

If we define $\sigma_- = \sum_{j=1}^{N} \sigma_-^j$ and $\sigma_z = \sum_{j=1}^{N} \sigma_z^j$ as the collective pseudo-spin operators, we arrive at the following set of dynamical equations

$$
\begin{aligned}
\langle \dot{a} \rangle &= -\kappa(1 + i\theta)\langle a \rangle + g_0 \langle \sigma_- \rangle + \mathcal{E} \\
\langle \dot{\sigma_-} \rangle &= -\gamma_\perp(1 + i\Lambda)\langle \sigma_- \rangle + g_0 \langle a\sigma_z \rangle \\
\langle \dot{\sigma_z} \rangle &= -\gamma_\parallel(\langle \sigma_z \rangle + N) - 2g_0(\langle a^\dagger \sigma_- \rangle + \langle \sigma_+ a \rangle) .
\end{aligned} \tag{3.9}
$$

Therefore, we may think of Eq. 3.9 as a description of the operator expectation dynamics for either a single-atom (with $N = 1$) or multi-atom system. In either case, the coupled equations 3.9 are not closed, as they contain expectation values of operator products. Therefore, we also need the dynamical equations for the higher order moments, of which there are an infinite number. For purely optical systems, order parameters can often be identified so that a system size expansion can yield a finite, closed set of equations which are valid in the "low-noise" limit (when the order parameter is large). Unfortunately, for coupled atom-field systems, there exists no suitable choice of system scaling parameters which would justify a system size expansion [6]. Furthermore, it is known that the quantum fluctuations produced by optical bistability can be non-classical even when $N \gg 1$ [9], and therefore would not fit into the classical mold which is the basis of a system size expansion. Nevertheless it has been demonstrated [101] that the Maxwell-Bloch equations, which will be derived from 3.9 below, can be brought with some refinements into close agreement with experiments on absorptive optical bistability in a multi-atom system. Indeed said equations are generally accepted as a canonical, though somewhat phenomenological, model for cavity nonlinear optics outside the strong coupling regime [37, 94].

3.2.2 Semiclassical description

An *ad hoc* (and somewhat crude) approach to obtaining a closed set of equations from 3.9 is to simply factorize the operator products, *e.g.*, $\langle a^\dagger \sigma_- \rangle \rightarrow \langle a^\dagger \rangle \langle \sigma_- \rangle$. While there is no formal basis for this procedure in general, the intuition behind it is that

for a large system with many weakly-excited atoms, the atom-field correlations will tend to zero, allowing for expectations of operator products to be factorized [22, 37]. But it should be noted that this approximation is not justified in the case of strong driving and certainly not for a single atom. This factorization yields

$$
\begin{aligned}
\langle \dot{a} \rangle &= -\kappa \left(1 + i\theta\right) \langle a \rangle + g_0 \langle \sigma_- \rangle + \mathcal{E} \\
\langle \dot{\sigma}_- \rangle &= -\gamma_\perp \left(1 + i\Lambda\right) \langle \sigma_- \rangle + g_0 \langle a \rangle \langle \sigma_z \rangle \\
\langle \dot{\sigma}_z \rangle &= -\gamma_\parallel \left(\langle \sigma_z \rangle + N\right) - 2g_0 (\langle a^\dagger \rangle \langle \sigma_- \rangle + \langle \sigma_+ \rangle \langle a \rangle)
\end{aligned}
\tag{3.10}
$$

which are the well known the Maxwell-Bloch equations, used to describe the semi-classical evolution of a classical field coupled to an atomic medium. The atom-field correlations which were discarded in performing the factorization above will tend to contribute "noise" on top of the mean field evolution described by Eq. 3.10. To put these equation into a more common form, we make the following definitions:

$$
z \doteq \langle a \rangle, \quad v \doteq \frac{2}{N} \langle \sigma_- \rangle, \quad m \doteq \frac{1}{N} \langle \sigma_z \rangle.
\tag{3.11}
$$

so that 3.10 becomes

$$
\begin{aligned}
\dot{z} &= -\kappa(1 + i\theta)z + (Ng_0/2)v + \mathcal{E} \\
\dot{v} &= -\gamma_\perp(1 + i\Lambda)v + 2g_0 zm \\
\dot{m} &= -\gamma_\parallel(m + 1) - g_0(z^* v + v^* z) .
\end{aligned}
\tag{3.12}
$$

A computationally more practical form of (3.12), which will prove useful in the bifurcation analysis to follow, may be obtained by transforming it into a dimensionless set of equations. We first make the following change of variables

$$
z \to \sqrt{n_0}\, x, \quad v \to -\sqrt{\frac{\gamma_\parallel}{\gamma_\perp}}\, p, \quad m \to -D,
\tag{3.13}
$$

followed be a re-scaling of time

$$t \rightarrow t'/\gamma_\perp \ , \tag{3.14}$$

so that we are left with the dimensionless Maxwell-Bloch equations [37]:

$$
\begin{aligned}
\dot{x} &= -k\left[(1+i\theta)x + 2Cp - y\right] \\
\dot{p} &= -(1+i\Lambda)p + xD \\
\dot{D} &= -\gamma\left[D - 1 + (x^*p + p^*x)/2\right]
\end{aligned}
\tag{3.15}
$$

where the complex variables x and p represent the amplitude of the intra-cavity field and the normalized atomic polarization, respectively, D is the (real) atomic population inversion, and y is the amplitude of the external drive field. The cooperativity parameter, C, measures the strength of the collective atom-field interaction, while k and γ are, respectively, the cavity field decay and atomic spontaneous emission rates, scaled by the atomic transverse relaxation rate, $\gamma_\perp$:

$$\gamma = \frac{\gamma_\parallel}{\gamma_\perp}, \quad k = \frac{\kappa}{\gamma_\perp}, \quad C = \frac{Ng_0^2}{2\kappa\gamma_\perp}, \quad y = \frac{\mathcal{E}}{\kappa\sqrt{n_0}} \ . \tag{3.16}$$

The two detuning parameters θ and Λ are the same as in Eq. (3.5). Although there is no way to express the steady-state solutions for the dependent variables x, p, and D in terms of the independent variables, we can find a simple set of equations relating the stationary solutions of the problem:

$$
\begin{aligned}
y &= |x_{ss}| \left\{ \left[1 + \frac{2C}{1 + \Lambda^2 + |x_{ss}|^2} \right]^2 \right. \\
&\qquad \left. + \left[\theta - \frac{2C\Lambda}{1 + \Lambda^2 + |x_{ss}|^2} \right]^2 \right\}^{1/2} ,
\end{aligned}
\tag{3.17}
$$

$$p_{ss} = \frac{(1 - i\Lambda)x_{ss}}{1 + \Lambda^2 + |x_{ss}|^2} \ , \tag{3.18}$$

$$D_{ss} = \frac{1 + \Lambda^2}{1 + \Lambda^2 + |x_{ss}|^2} \ . \tag{3.19}$$
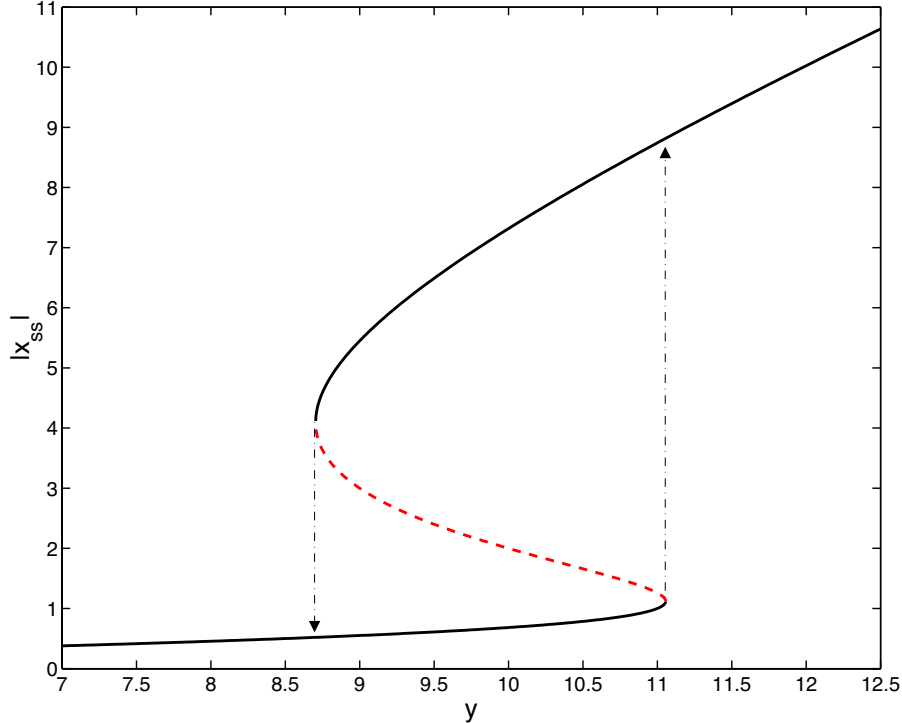
Figure 3.1: Semiclassical calculation of the intracavity steady-state field magnitude $|x_{ss}|$ versus drive field y. The dashed portion of the curve is unstable. The parameter values are: $C = 10, k = 0.1, \gamma = 2, \theta = 0$, and $\Lambda = 0$. Arrows indicate the evolution of the steady-state solution when the drive field y is swept smoothly through a bifurcation point: the state originally on the lower (upper) branch moving through the bifurcation point $y \approx 11.1$ ($y \approx 8.7$) is attracted to the upper (lower) branch.

In Figure 3.1 we plot a typical input-output curve generated using Eq. (3.17). Note that in the range $8.7 \lesssim y \lesssim 11.1$ the curve displays absorptive bistability, with the lower and upper branches of the 'S'-shaped curve supporting stable solutions (the dashed portion of the curve is unstable). It is important to note that the above equations depend upon g_0 and N only through the cooperativity parameter, C. Thus, identical behavior is predicted for a range of systems with varying atom number and $g_0 = \sqrt{2\kappa\gamma_\perp C/N}$. Of course, one expects that the quantum fluctuations and atom-field correlations that are disregarded in the derivation of the Maxwell-Bloch equations should begin to matter as N approaches 1. A direct comparison of 'system behavior' according to (3.15) versus the master equation (3.2) with the quantities $\{\gamma, k, C, y, \theta, \Lambda\}$ held fixed can thus be construed as a case study

in quantum-(semi)classical correspondence. The question of course is exactly what 'system behavior' should be compared and how; the strategy in what follows will be to focus on photocurrent properties near bifurcation points of the semiclassical model. We thus next discuss a systematic approach to finding interesting points in the bifurcation set of the Maxwell-Bloch equations, and then review a standard monte carlo approach to simulating photocurrents according to the quantum model. After presenting some numerical results, we conclude with a discussion of some interesting features of the quantum-semiclassical comparison that suggest directions for further research.

3.3 Bifurcation set of the mean-field equations

In this section we delineate the process used to find and classify bifurcations in the mean-field dynamics described by Eq. 3.15. In particular, in Sec. 3.3.1 we characterize both saddle-node bifurcations and Hopf bifurcations. We further differentiate between super- and subcritical Hopf bifurcations in Sec. 3.3.2. In the former case, the bifurcation will destabilize a (typically) fixed point with a *local* (small amplitude) limit cycle born about the prior steady-state. In the latter case, *no local* limit cycle is created about the destabilized steady-state solution, and the system will move to a new (possibly distant) attractor. For this reason, subcritical Hopf bifurcations often lead to qualitatively more radical results, including regions of multi-stability.

3.3.1 Linearization about steady-state

In order to determine the parameter values that lead to bifurcations, we return to Eq. 3.15, and linearize the system dynamics about steady-state. We consider small fluctuations $\delta x, \delta p$, and δD about steady-state, and set $x = x_{ss} + \delta x$, $p = p_{ss} + \delta p$, *et*

cetera. After eliminating terms that are second order in the small fluctuations,

$$
\begin{pmatrix} \dot{\delta x} \\ \dot{\delta x^*} \\ \dot{\delta p} \\ \dot{\delta p^*} \\ \dot{\delta D} \end{pmatrix} = \mathbf{J} \begin{pmatrix} \delta x \\ \delta x^* \\ \delta p \\ \delta p^* \\ \delta D \end{pmatrix}
\tag{3.20}
$$

where the Jacobian $\mathbf{J}$ is given by

$$
\mathbf{J} = \begin{pmatrix} -k(1+i\theta) & 0 & -2Ck & 0 & 0 \\ 0 & -k(1-i\theta) & 0 & -2Ck & 0 \\ D_{ss} & 0 & -(1+i\Lambda) & 0 & x_{ss} \\ 0 & D_{ss} & 0 & -(1-i\Lambda) & x^*_{ss} \\ -\gamma p^*_{ss}/2 & -\gamma p_{ss}/2 & -\gamma x^*_{ss}/2 & -\gamma x_{ss}/2 & -\gamma \end{pmatrix}.
\tag{3.21}
$$

The associated characteristic equation will have the form

$$
\lambda^5 + a_1\lambda^4 + a_2\lambda^3 + a_3\lambda^2 + a_4\lambda + a_5 = 0
\tag{3.22}
$$

with coefficients given by the following expressions:

$$
\begin{aligned}
a_1 &= 2 + \gamma + 2k \ , \\
a_2 &= k^2(1 + \theta^2) + (2\gamma + 1 + \Lambda^2 + \gamma|x_{ss}|^2) \\
&\quad + 2k(\gamma + 2) + 4kCD_{ss} \ , \\
a_3 &= \gamma(1 + \Lambda^2 + |x_{ss}|^2) + 2k(2\gamma + 1 + \Lambda^2 + \gamma|x_{ss}|^2) \\
&\quad + k^2(1 + \theta^2)(\gamma + 2) + 4kCD_{ss}(\gamma + k + 1) \\
&\quad - \gamma kC(p_{ss}^* x_{ss} + p_{ss} x_{ss}^*) \ , \\
a_4 &= 2k\gamma(1 + \Lambda^2 + |x_{ss}|^2) \\
&\quad + k^2(1 + \theta^2)(2\gamma + 1 + \Lambda^2 + \gamma|x_{ss}|^2) \\
&\quad + 2kCD_{ss}[2k(1 - \Lambda\theta) + 2\gamma(k + 1) + \gamma|x_{ss}|^2] \\
&\quad + \gamma kC\left[i(\Lambda + k\theta)(p_{ss}^* x_{ss} - p_{ss} x_{ss}^*)\right. \\
&\quad \left. - (k + 1)(p_{ss}^* x_{ss} + p_{ss} x_{ss}^*)\right] + 4k^2C^2 D_{ss}^2 \ , \\
a_5 &= \gamma k^2\{4C^2 D_{ss}[D_{ss} - (p_{ss}^* x_{ss} + p_{ss} x_{ss}^*)2] \\
&\quad + (1 + \theta^2)(1 + \Lambda^2 + |x_{ss}|^2) \\
&\quad + 4CD_{ss}(1 - \Lambda\theta)\} \ .
\end{aligned}
\tag{3.23}
$$

These coefficients may be further simplified by using the form of D_{ss} found in 3.17 and the relations

$$
\begin{aligned}
i(p_{ss} x_{ss}^* - p_{ss}^* x_{ss}) &= -2\Lambda|x_{ss}|^2/(1 + \Lambda^2 + |x_{ss}|^2) \\
(p_{ss} x_{ss}^* + p_{ss}^* x_{ss}) &= 2|x_{ss}|^2/(1 + \Lambda^2 + |x_{ss}|^2) \ ,
\end{aligned}
$$

so that the a's found in the characteristic equation are written explicitly in terms of six parameters: $C, k, \gamma, \theta, \Lambda$, and $|x_{ss}|$.

Needless to say, it is impossible to solve for the eigenvalues of this system analytically. However, other methods that provide analytic tests of stability do exist. Most notably, the Routh-Hurwitz criterion provides a set of inequalities based on combinations of the a's that can be used to determine stability. Unfortunately, this procedure is simply too general, and it is ill suited for the purpose of determining the boundaries of instability in terms of our controllable parameters. We can, however,

make use of the Routh-Hurwitz criteria to find the following *necessary* conditions for stability [102, 103]

$$a_1, \ a_2, \ a_3, \ a_4, \ a_5 \ > \ 0 \ .$$

Furthermore, at a Hopf bifurcation the system must have a pair of pure imaginary eigenvalues, $\lambda_{1,2} = \pm i\omega$. Demanding that the characteristic equation support these solutions establishes the following critical condition for a Hopf bifurcation

$$f = (a_1 a_2 - a_3)(a_3 a_4 - a_2 a_5) - (a_1 a_4 - a_5)^2 = 0 \quad , \tag{3.24}$$

with $f > 0$ providing another necessary condition for stability.

For the purpose of delineating the instability boundaries, the six inequalities

$$a_1, \ a_2, \ a_3, \ a_4, \ a_5, \ f \ > \ 0 \tag{3.25}$$

are not equally important. Starting from a stable region of the parameter space, there are only two ways for the steady-state solution to become unstable: (i) a single real eigenvalue passes through the origin and becomes positive; (ii) a pair of complex conjugate eigenvalues cross the imaginary axis (starting from the LHP). For case (i) the coefficient a_5 must change signs first, whereas for case (ii) it is f that first changes sign. Therefore, if the goal is to determine the conditions for a known *stable* state to become unstable, there is no need to consider the other necessary conditions and all focus may be placed on a_5 and f. Furthermore, if we are only interested in Hopf Bifurcations, we can also ignore the $a_5 > 0$ condition, which determines the boundary for saddle-node bifurcations where the steady-state curve displays a turning point (this can be seen by noting that $d(y^2)/d(|x_{ss}|^2) \propto a_5$, so that $a_5 < 0$ indicates bistability.)

It should be noted again, that the inequalities 3.25 are only necessary conditions for stability, they are not sufficient. For example, the system could have one real negative eigenvalue, and two pairs of complex eigenvalues each with positive real parts, and still have $a_1, a_2, a_3, a_4, a_5, f > 0$. However, the stability condition $f > 0$

can be made sufficient for a given region in parameter space if we can show that this region is 'connected' to a known stable region of the space (two regions of parameter space are 'connected' if there exists a continuous variation of the parameters that moves the system from one region, while retaining the sign of a_1, a_2, a_3, a_4, a_5, and f through the entire path.) Thus, if we know that a particular region of parameter space (with $a_1, a_2, a_3, a_4, a_5 > 0$) is connected to a stable region, we know that f can serve as a necessary and sufficient condition for the steady-state solution to undergo a Hopf bifurcation. Practically, all this means is that starting from a stable state, the first crossing of a surface $a_5 = 0$ ($f = 0$), will drive the system unstable through a saddle-node (Hopf) bifurcation. Furthermore, the stability condition $f > 0$ is quite reliable in practice, even when we can't show connectedness to a stable region.

3.3.2 Super- and subcritical Hopf bifurcations

In order to determine whether a Hopf bifurcation is super- or subcritical, the eigenvalues and eigenvectors about the bifurcation point must first be found. Among the possible reasons for seeking one or the other kind are that supercritical Hopf bifurcations can be used for resonant nonlinear amplification of small periodic signals [104], and subcritical Hopf bifurcations are likely to indicate the presence of limit cycles that coexist with other attractors. The latter type of scenario may give rise to observable 'quantum jumps' among non-fixed point attractors, which would be an interesting generalization of the predictions of Refs. [3, 28]. We thus believe that the theory for distinguishing super- and subcritical Hopf bifurcations merits an extended discussion. Note that our expressions below correct some apparent misprints in Ref. [31], with minor changes of notation.

At a Hopf bifurcation, the linearized system 3.21 has a pair of pure imaginary eigenvalues $\lambda_{1,2} = \pm i\omega$, with the frequency ω determined by

$$\omega^2 = \frac{a_1 a_4 - a_5}{a_1 a_2 - a_3}.$$

(3.26)

Thus, the characteristic equation 3.22 can be factored as

$$(\lambda^2 + \omega^2)(\lambda^3 + a_1\lambda^2 + b_2\lambda + b_3) = 0 \tag{3.27}$$

with

$$b_2 = a_4/\omega^2, \quad \text{and} \quad b_3 = a_5/\omega^2. \tag{3.28}$$

Solving for the other three eigenvalues yields

$$
\begin{aligned}
\lambda_3 &= \nu w - p/(3\nu w) - a_1/3 \\
\lambda_4 &= \nu^* w - p/(3\nu^* w) - a_1/3 \\
\lambda_5 &= w - p/(3w) - a_1/3
\end{aligned}
\tag{3.29}
$$

where the variables

$$
\begin{aligned}
\nu &= (-1 + i\sqrt{3})/2 \\
w &= \left\{ q/2 + \sqrt{(q/2)^2 + (p/3)^3} \right\}^{1/3} \\
q &= -2a_1^3/27 + a_1 b_2/3 - b_3 \\
p &= -a_1^2/3 + b_2
\end{aligned}
\tag{3.30}
$$

are determined from the solution to the cubic equation embedded in 3.27. Following the approach in [31] (and noting several corrections), the system eigenvectors, $\alpha_{\mathbf{i}}$, may be found in terms of the λ_i by solving the linearized dynamics

$$\mathbf{J}\alpha_{\mathbf{i}} = \lambda_i \alpha_{\mathbf{i}} \tag{3.31}$$

where $\mathbf{J}$ is the Jacobian in 3.21. Expressing the results in terms of the λ_i, one arrives

at

$$\alpha_{\mathbf{i}} = \begin{pmatrix} \exp\left(i\phi_i\right) \\ \exp\left(-i\phi_i\right) \\ -\exp\left(i\phi_i\right)\left[k(1+i\theta)+\lambda_i\right]/(2Ck) \\ -\exp\left(-i\phi_i\right)\left[k(1-i\theta)+\lambda_i\right]/(2Ck) \\ -\exp\left(i\phi_i\right)\left\{2CD_{ss}k+(1+i\Lambda+\lambda_i)\left[k(1+i\theta)+\lambda_i\right]\right\}/(2Ckx) \end{pmatrix} \tag{3.32}$$

where the phase factor, $\exp\left(i\phi_i\right)$, is chosen to preserve symmetry in the components and is given by

$$e^{i\phi_i} = \sqrt{\frac{x\left\{2CD_{ss}k+(1-i\Lambda+\lambda_i)[k(1-i\theta)+\lambda_i]\right\}}{x^*\left\{2CD_{ss}k+(1+i\Lambda+\lambda_i)[k(1+i\theta)+\lambda_i]\right\}}}. \tag{3.33}$$

The set of eigenvectors, $\{\alpha_{\mathbf{i}}\}$, define a linear transformation of variables such that dynamical equations about steady-state contain no linear cross couplings. The old variables are related to the new variables through the relation

$$\delta\mathbf{q} = \widetilde{\alpha}\,\mathbf{z} \tag{3.34}$$

where $\widetilde{\alpha} = [\alpha_{\mathbf{1}}\ \alpha_{\mathbf{2}}\ \alpha_{\mathbf{3}}\ \alpha_{\mathbf{4}}\ \alpha_{\mathbf{5}}]$ is the transformation matrix comprised of the system eigenvectors, and $\delta\mathbf{q} = \{\delta x,\ \delta x^*,\ \delta p,\ \delta p^*,\ \delta D\}^T$ are the fluctuations about steady-state. Starting from the dynamical equations for the fluctuations about steady-state

$$\begin{aligned} \dot{\delta x} &= -k\left[(1+i\theta)\delta x + 2C\delta p\right] \\ \dot{\delta x^*} &= (\dot{\delta x})^* \\ \dot{\delta p} &= -(1+i\Lambda)\delta p + \delta x\delta D \\ &\quad + \{\delta x D_{ss} + x_{ss}\delta D\} \\ \dot{\delta p^*} &= (\dot{\delta p})^* \\ \dot{\delta D} &= -\gamma\left[\delta D + (\delta x^*\delta p + \delta p^*\delta x)/2\right] \\ &\quad + \{\gamma/2(\delta x^* p_{ss} + x_{ss}^*\delta p + p_{ss}^*\delta x + \delta p^* x_{ss})\}, \end{aligned} \tag{3.35}$$

the transformation of coordinates $\mathbf{z} = \widetilde{\beta}\,\delta\mathbf{q}$, with $\widetilde{\beta} = \widetilde{\alpha}^{-1}$, eliminates any linear coupling between variables

$$
\begin{aligned}
\dot{z}_j &= \lambda_j z_j + \beta_{j3}\delta x \delta D + \beta_{j4}\delta x^* \delta D \\
&\quad - \gamma\beta_{j5}(\delta x^* \delta p + \delta x \delta p^*)/2 \ .
\end{aligned} \tag{3.36}
$$

Finally, after utilizing the transformation 3.34, this equation may be expressed in terms of the "diagonalized" coordinates alone:

$$
\begin{aligned}
\dot{z}_j &= \lambda_j z_j + \sum_{k,l=1}^{5} [\beta_{j3}\alpha_{1k}\alpha_{5l} + \beta_{j4}\alpha_{2k}\alpha_{5l} \\
&\quad - \gamma\beta_{j5}(\alpha_{2k}\alpha_{3l} + \alpha_{1k}\alpha_{4l})/2]\, z_k z_l \ .
\end{aligned} \tag{3.37}
$$

Having converted the system into the form 3.37, the dynamics about a Hopf bifurcation may be reduced onto a center manifold [105]: since the system dynamics will be dominated by the "slow" variables, z_1 and z_2, the flow of the differential equation may be locally approximated on the surface generated by z_1 and z_2, with the "fast" variables, $z_{j=3,4,5}$, represented by a local graph $z_j = A_j(z_1, z_2)$. Furthermore, the local graph, $A_j(z_1, z_2)$, may be approximated by a power series expansion

$$
z_j = a_{20}(j)z_1^2 + a_{11}(j)z_1 z_2 + a_{02}(j)z_2^2 + \dots, \ j = 3, 4, 5 \ , \tag{3.38}
$$

so that the reduced dynamics may be approximated by

$$
\dot{z}_j \approx 2i\omega a_{20}(j)z_1^2 - 2i\omega a_{02}(j)z_2^2 + \dots, \ j = 3, 4, 5 \ . \tag{3.39}
$$

The coefficients in 3.38 are determined by substituting equations 3.38 and 3.39 into the exact dynamics 3.37 and equating like powers in $z_1^n z_2^m$.

With aid of the local graph 3.38, the dynamics may be reduced onto the center coordinates associated with eigenvalues having zero real part:

$$
\dot{z}_1 = i\omega z_1 + b_{20}(1)z_1^2 + b_{11}(1)z_1 z_2 + b_{02}(1)z_2^2 + b_{21}(1)z_1^2 z_2 + \dots \tag{3.40}
$$

with $z_2 = z_1^*$ near the Hopf bifurcation. Writing $z_1 = u + iv$, with $\{u, v\} \in \mathbb{R}$, the reduced dynamics of the complex variable z_1 may be expressed by a set of real coupled equations

$$
\begin{aligned}
\dot{u} &= -\omega v + F(u, v) \\
\dot{v} &= \omega u + G(u, v)
\end{aligned}
, \tag{3.41}
$$

with F and G comprised of terms nonlinear in u and v. It can be shown [105] that there exists a smooth change of variables which will put Eq. 3.41 into the normal form

$$
\begin{aligned}
\dot{r} &= \eta_3 r^3 + \eta_5 r^5 + ... \\
\dot{\zeta} &= \omega + \epsilon_2 r^2 + \epsilon_4 r^4 + ...
\end{aligned}
, \tag{3.42}
$$

with the stability of the bifurcation governed by the sign of η_3. For $\eta_3 < 0$ the bifurcation is supercritical, and a stable, small amplitude limit cycle is born about the newly destabilized steady-state. For $\eta_3 > 0$, the bifurcation is subcritical, and no such small amplitude cycle is created. In this case, the system may be thrown far away from the steady-state solution, onto either a limit cycle, a different branch of the steady-state curve, or some other attractor.

3.3.3 Calculation of η_3

The critical parameter η_3 can be expressed explicitly [105] in terms of the coefficients in 3.40 and the bifurcation frequency ω

$$
\eta_3 = \text{Re}[b_{21}(1)] - \frac{1}{\omega}\text{Im}[b_{20}(1)b_{11}(1)] . \tag{3.43}
$$

As the calculations for the relevant coefficients are rather tedious and time consuming, they are included here for posterity:

$$
\left.
\begin{aligned}
a_{20}(j) &= b_{20}(j)/(2i\omega - \lambda_j) , \\
a_{11}(j) &= -b_{11}(j)/\lambda_j ,
\end{aligned}
\right\} j = 3, 4, 5 \tag{3.44}
$$

where

$$b_{20}(j) = \beta_{j3}\alpha_{11}\alpha_{51} + \beta_{j4}\alpha_{21}\alpha_{51} - \gamma\beta_{j5}(\alpha_{21}\alpha_{31} + \alpha_{11}\alpha_{41})/2 \ ,$$

$$b_{11}(j) = \beta_{j3}\left(\alpha_{11}\alpha_{52} + \alpha_{12}\alpha_{51}\right) + \beta_{j4}\left(\alpha_{21}\alpha_{52} + \alpha_{22}\alpha_{51}\right) \tag{3.45}$$

$$- \gamma\beta_{j5}\left[\alpha_{21}\alpha_{32} + \alpha_{22}\alpha_{31} + \alpha_{11}\alpha_{42} + \alpha_{12}\alpha_{41}\right]/2 \ .$$

Inserting 3.38, with coefficient $a_{20}(j)$ and $a_{11}(j)$ given by 3.44, into the diagonalized equation 3.37 for $j = 1$ yields a heinous expression for the last required coefficient

$$
\begin{aligned}
b_{21}(1) \ = \ & \beta_{13}[a_{20}(3)\left(\alpha_{12}\alpha_{53} + \alpha_{13}\alpha_{52}\right) + a_{20}(4)\left(\alpha_{12}\alpha_{54} + \alpha_{14}\alpha_{52}\right) + \\
& a_{20}(5)\left(\alpha_{12}\alpha_{55} + \alpha_{15}\alpha_{52}\right) + a_{11}(3)\left(\alpha_{11}\alpha_{53} + \alpha_{13}\alpha_{51}\right) + \\
& a_{11}(4)\left(\alpha_{11}\alpha_{54} + \alpha_{14}\alpha_{51}\right) + a_{11}(5)\left(\alpha_{11}\alpha_{55} + \alpha_{15}\alpha_{51}\right)] \\
+ \ & \beta_{14}[a_{20}(3)\left(\alpha_{22}\alpha_{53} + \alpha_{23}\alpha_{52}\right) + a_{20}(4)\left(\alpha_{22}\alpha_{54} + \alpha_{24}\alpha_{52}\right) + \\
& a_{20}(5)\left(\alpha_{22}\alpha_{55} + \alpha_{25}\alpha_{52}\right) + a_{11}(3)\left(\alpha_{21}\alpha_{53} + \alpha_{23}\alpha_{51}\right) + \\
& a_{11}(4)\left(\alpha_{21}\alpha_{54} + \alpha_{24}\alpha_{51}\right) + a_{11}(5)\left(\alpha_{21}\alpha_{55} + \alpha_{25}\alpha_{51}\right)] \\
- \ & \tfrac{\gamma}{2}\beta_{15}[a_{20}(3)\left(\alpha_{22}\alpha_{33} + \alpha_{23}\alpha_{32} + \alpha_{12}\alpha_{43} + \alpha_{13}\alpha_{42}\right) + \\
& a_{20}(4)\left(\alpha_{22}\alpha_{34} + \alpha_{24}\alpha_{32} + \alpha_{12}\alpha_{44} + \alpha_{14}\alpha_{42}\right) + \\
& a_{20}(5)\left(\alpha_{22}\alpha_{35} + \alpha_{12}\alpha_{45} + \alpha_{25}\alpha_{32} + \alpha_{15}\alpha_{42}\right) + \\
& a_{11}(3)\left(\alpha_{21}\alpha_{33} + \alpha_{11}\alpha_{43} + \alpha_{23}\alpha_{31} + \alpha_{13}\alpha_{41}\right) + \\
& a_{11}(4)\left(\alpha_{21}\alpha_{34} + \alpha_{11}\alpha_{44} + \alpha_{24}\alpha_{31} + \alpha_{14}\alpha_{41}\right) + \\
& a_{11}(5)\left(\alpha_{21}\alpha_{35} + \alpha_{11}\alpha_{45} + \alpha_{25}\alpha_{31} + \alpha_{15}\alpha_{41}\right)] \ .
\end{aligned}
\tag{3.46}
$$

3.4 Numerical results

For the numerical analysis to follow, we make repeated use of the steady-state Q-function and quantum trajectory simulations. These numerical tools are described in sections 2.2.3 and 2.2.5, respectively.

3.4.1 Absorptive bistability

In Figure 3.1 we plot the steady-state intra-cavity field magnitude vs. drive field predicted by the (dimensionless) semiclassical equations 3.17 for the case of purely
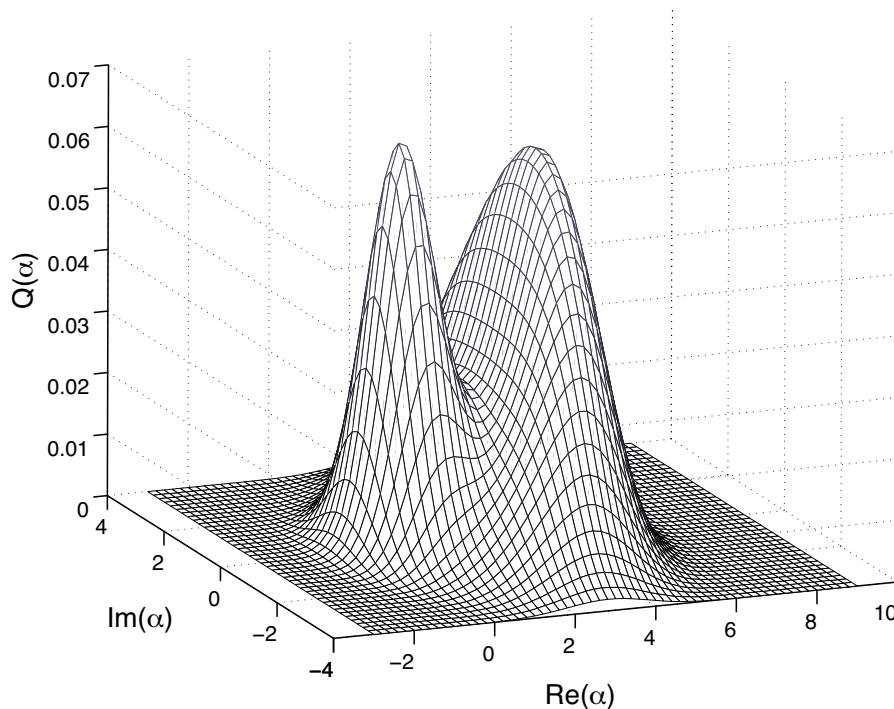
Figure 3.2: Steady-state $Q(\alpha)$ for the parameter values in Figure 3.1, and drive field $y = 11.3$.

absorptive bistability ($\theta = \Lambda = 0$). These parameter values correspond to $g = 1.41, \kappa = .1, \gamma_\parallel = 2, \Delta = 0, \Theta = 0$, in the master equation 3.2, and a saturation photon number, $n_0 = 0.25$. In Figure 3.2 we plot the bimodal Q-function obtained from the steady solution to the master equation for a drive field $y = 11.3$ ($\mathcal{E} = 0.565$), chosen such that the integrated probabilities in each mode of the Q-function are approximately equal. While this Q-function indicates that the quantum dynamics show bistable behavior, it is interesting to note that the master equation produces this bimodal distribution for a drive field where the mean-field equations do not predict bistability (the lower branch in Figure 3.1 disappears at $y \approx 11.1$). In fact, the Q-function distributions over most of the semiclassically bistable region are not bimodal, and only become so for $11 \lesssim y \lesssim 11.5$.

In Figure 3.3 we plot the photocurrent 2.75 corresponding to a measurement of the amplitude quadrature of the cavity output field. As expected, the field localization brought about by the continuous homodyne measurement causes the signal amplitude
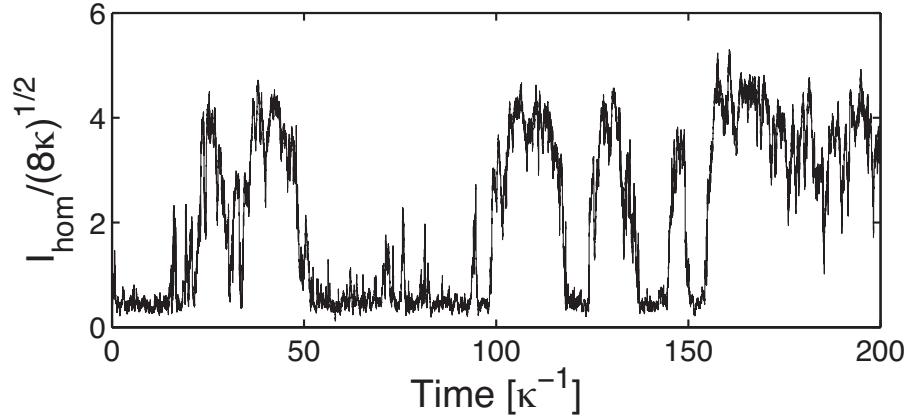
Figure 3.3: Homodyne photocurrent from quantum trajectory simulation for parameter values in Figure 3.2.

to switch, at stochastic intervals, between values consistent with the two peaks in $Q(\alpha)$.

3.4.2 Supercritical Hopf bifurcation

In Figure 3.4 we plot the equilibrium attractors of the mean-field dynamics 3.15 for a case where the steady-state fixed points predicted in 3.17 undergo supercritical Hopf bifurcations. Starting on the lower (upper) branch of the steady-state curve, as the drive field y is swept through the critical point CP_1 (CP_2) the fixed point is destabilized by a small amplitude limit cycle, LC_1, which grows in amplitude, peaking at $y \approx 2800$, until finally recombining with and restabilizing the fixed point at CP_2 (CP_1). To represent the oscillatory solution that is born out of the bifurcation, we plot the steady-state *maximum* field magnitude for a state localized on the stable limit cycle, and denote this as LC_1. Thus, the plotted curve LC_1 essentially represents the amplitude *plus* mean value of the limit cycle.

The parameter values used in Figure 3.4 correspond to $g = 1, \kappa = .01, \gamma_\parallel = 2, \Delta = 1.25, \Theta = -6$ in Eq. 3.2, and a saturation photon number $n_0 = 0.5$. Using these values, we compute $Q(\alpha)$ for $y = 2800$ ($\mathcal{E} = 19.8$), where the limit cycle amplitude is maximal. The result is plotted in Figure 3.5. The ring-like shape of the distribution is consistent with oscillation of a coherent state in the intracavity field. This interpreta-
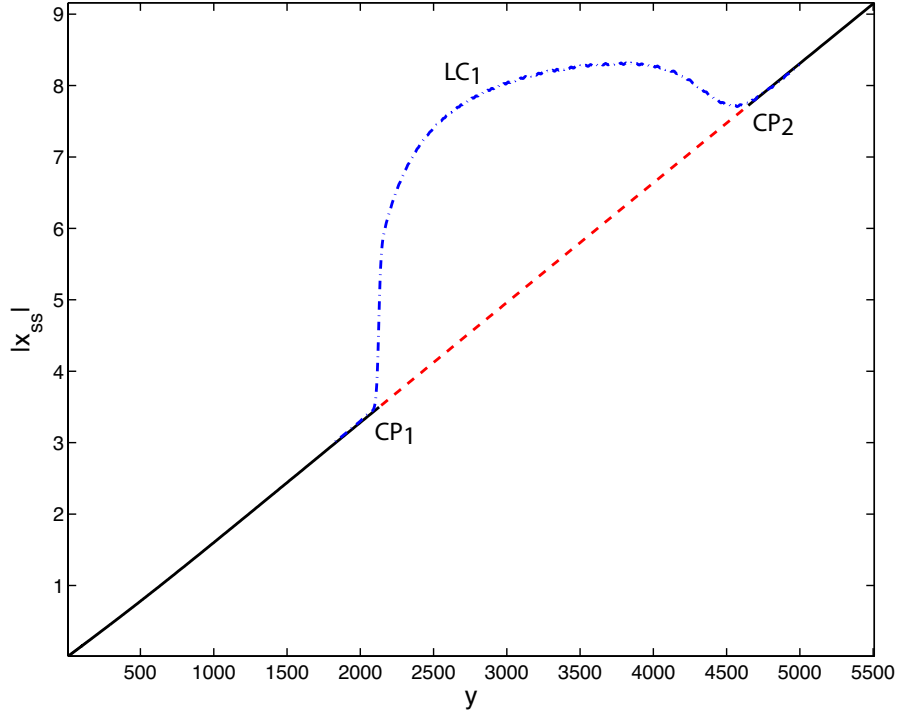
Figure 3.4: Semiclassical calculation of the intracavity steady-state field magnitude $|x_{ss}|$ versus drive field y for: $C = 50, k = .01, \gamma = 2, \theta = -600$, and $\Lambda = 1.25$. The upper dashed-dotted curve (LC_1)represents the steady-state oscillation maximum (steady-state magnitude plus mean value) associated with the limit cycle formed when the fixed point becomes unstable due to a Hopf bifurcation (at CP_1 and CP_2). The lower dashed curve is unstable.

tion is further supported by the inset in Figure 3.6, where we plot the autocorrelation function $G_Y^{(1)}(\tau) = \langle Y(\tau)Y(0)\rangle - \langle Y(0)\rangle^2$, computed using the quantum regression theorem [35], where $Y = \frac{i}{2}(a^\dagger - a)$ is the phase quadrature amplitude operator of the intracavity field. In addition, Figure 3.6 displays the coherence time of the steady-state quantum oscillations over a range of drive fields. The results indicate that the coherence times depend strongly on the amplitude of the limit cycle, LC_1, which is again consistent with the idea of an oscillating coherent state for the intracavity field.

It can be seen clearly from the inset of Figure 3.6 that the limit cycle comprises an oscillation of the intracavity field at a frequency much higher than κ. It should thus be difficult to see the oscillation directly in the broadband photocurrent generated by
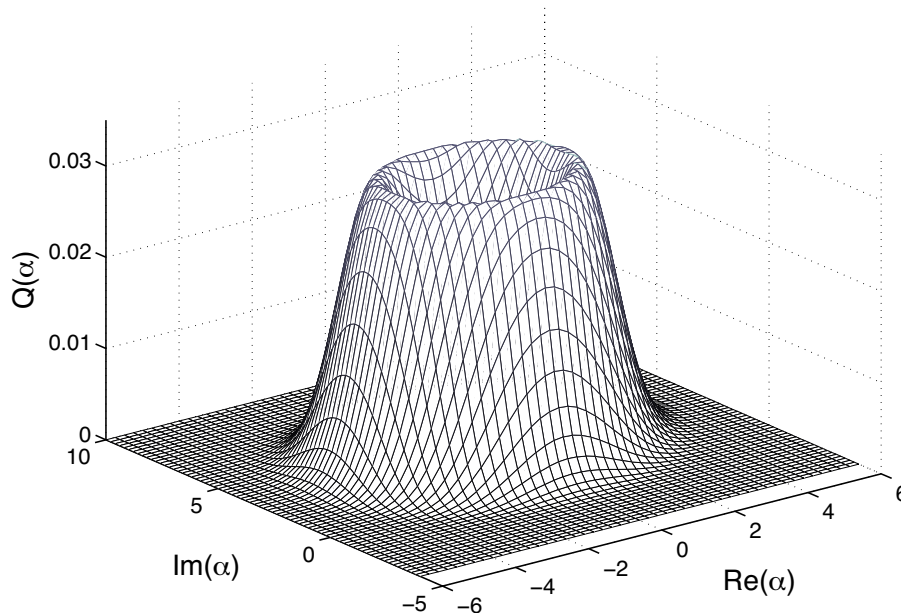
Figure 3.5: Steady-state $Q(\alpha)$ for the parameter values in Figure 3.4, and drive field $y = 2800$.

amplitude-quadrature homodyne detection of the cavity output field. In Figure 3.7 however we plot several power spectra of photocurrent records generated in quantum trajectory simulations. For $y = 1000$ (below CP_1 in Figure 3.4) the spectrum shows little or no sign of a coherent peak, but for $y = 2800$ we see that homodyne detection of the field amplitude reveals clear evidence of the limit-cycle oscillation. This demonstrates at least a basic correspondence with the semiclassical predictions shown in Figure 3.4. At $y = 5000$ (above CP_2 in Figure 3.4), however, we see that the quantum model still exhibits strong oscillations even though the semiclassical model predicts a fixed point solution. This persistence of the oscillatory behavior at both higher and lower driving fields can also be seen in Figure 3.6.

3.4.3 Subcritical Hopf bifurcation

In Figure 3.8 we plot the steady-state solutions for a parameter regime where the mean-field equations predict a subcritical Hopf bifurcation. The solid (dashed) curve corresponds to the stable (unstable) fixed points predicted by Eq. 3.17, whereas the attractor LC_2 (plotted dashed-dotted) corresponds to a stable limit cycle. Beginning
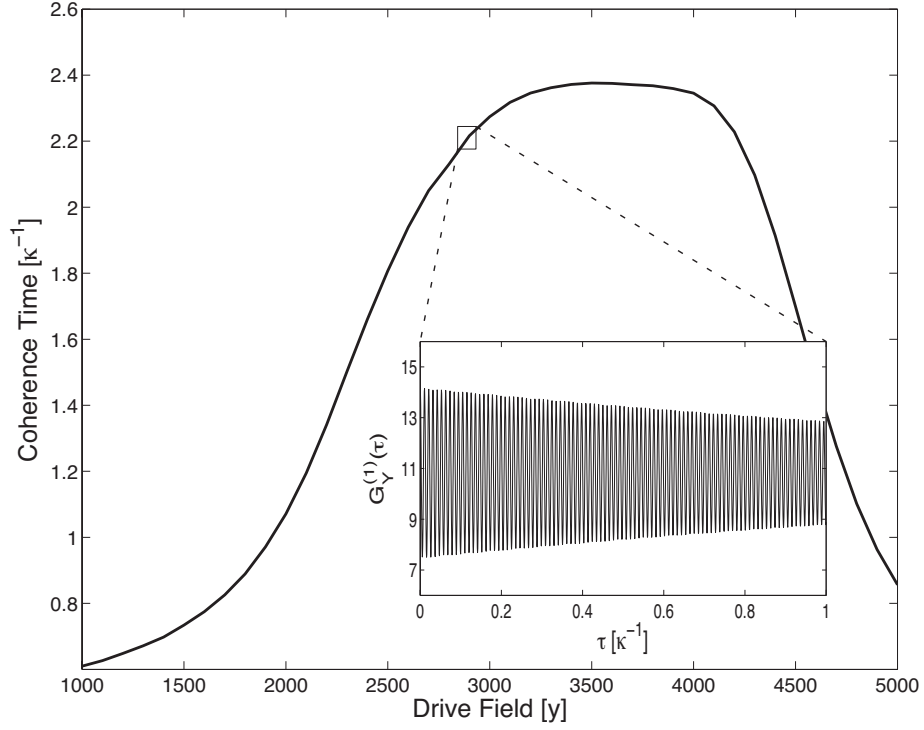
Figure 3.6: Coherence times calculated from steady-state autocorrelation function, $G_Y^{(1)}(\tau)$, of the quantum mechanical phase quadrature. Parameter values same as in Figure 3.4. The coherence time is estimated by fitting a damped sinusoid to $G_Y^{(1)}(\tau)$. Inset: simulated $G_Y^{(1)}(\tau)$ for the drive field in Figure 3.5.

on the upper stable branch of fixed points, as the drive field is swept through the critical point CP_4, the system undergoes a subcritical Hopf bifurcation. In the range $475 \lesssim y \lesssim 925$, the semiclassical equations predict coexistence of a stable fixed point and limit cycle, which is a common signature of subcritical bifurcations. Note that at $y \approx 925$ the limit cycle LC_2 is destabilized but the fixed point is not. The two arrowed lines in Figure 3.8 do not represent solutions to the equations, but simply indicate which attractor a destabilized state will seek.

The parameter values used in Figure 3.8 correspond to $g = 4.47, \kappa = .05, \gamma_{\parallel} = 2, \Delta = 2, \Theta = -2.75$, and a saturation photon number $n_0 = 0.025$. The small size of n_0 indicates that the qualitative behavior of steady-state solutions to the master equation will be dominated by quantum fluctuations (over the dynamics implied by the mean field equations.) We see that this interpretation is justified by the plot of $Q(\alpha)$ in Figure 3.9, at a drive field $y = 1000$, near the amplitude maximum of LC_2.
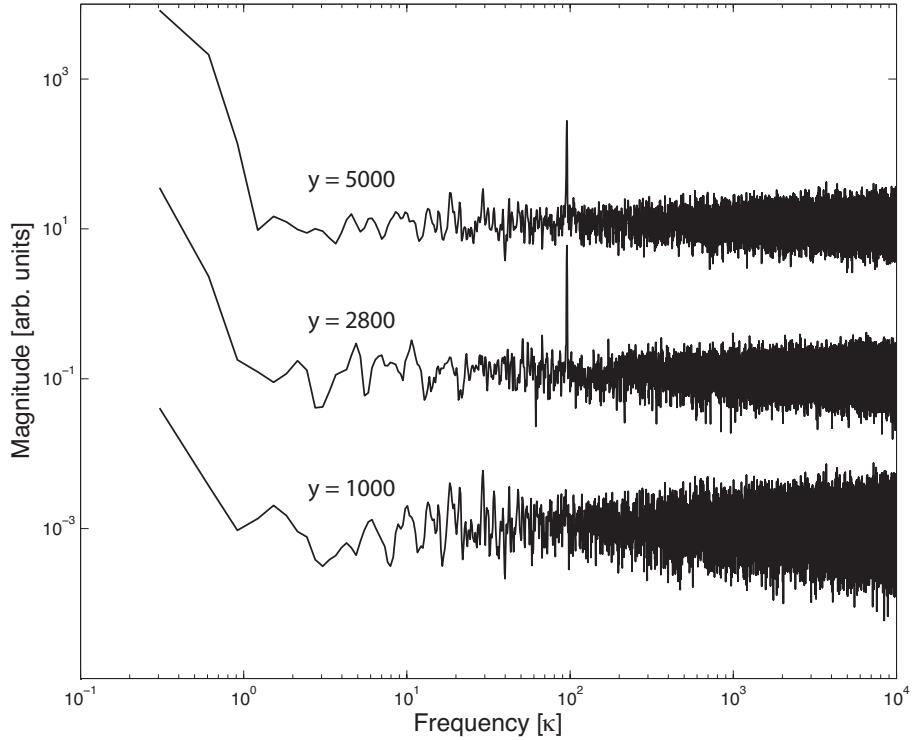
Figure 3.7: Power spectra computed from simulated photocurrents for amplitude-quadrature homodyne detection of the cavity output field, using parameter values as in Figure 3.4. Lowest plot: $y = 1000$, below the bifurcation point; middle plot: $y = 2800$, where the classical oscillation amplitude is maximal; upper plot: $y = 5000$, where the semiclassical model no longer predicts a limit cycle.

The features in the surface plot (Figure 3.9a) are hardly profound. The contour plot in Figure 3.9b is somewhat more elucidating, and shows signs of the coexistence of oscillatory, albeit asymmetric, and fixed coherent states. These 'blurry' results are not surprising, as the small n_0, and relation 3.13, imply that, in the quantum case, the structure implied by the limit cycle and fixed points in Figure 3.8 should be heavily affected by fluctuations.

Figure 3.10 suggests, however, that the field localization provided by continuous homodyne measurement of the phase quadrature can reveal signatures of bistability in the photocurrent. In particular, in Figure 3.10b we plot a typical trajectory for a drive field $y = 1000$, as in Figure 3.9. While the contrast is marginal, as it would have to be given the discussion above, the qualitative appearance of this simulated photocurrent record is that of oscillations interrupted by brief periods of stationary
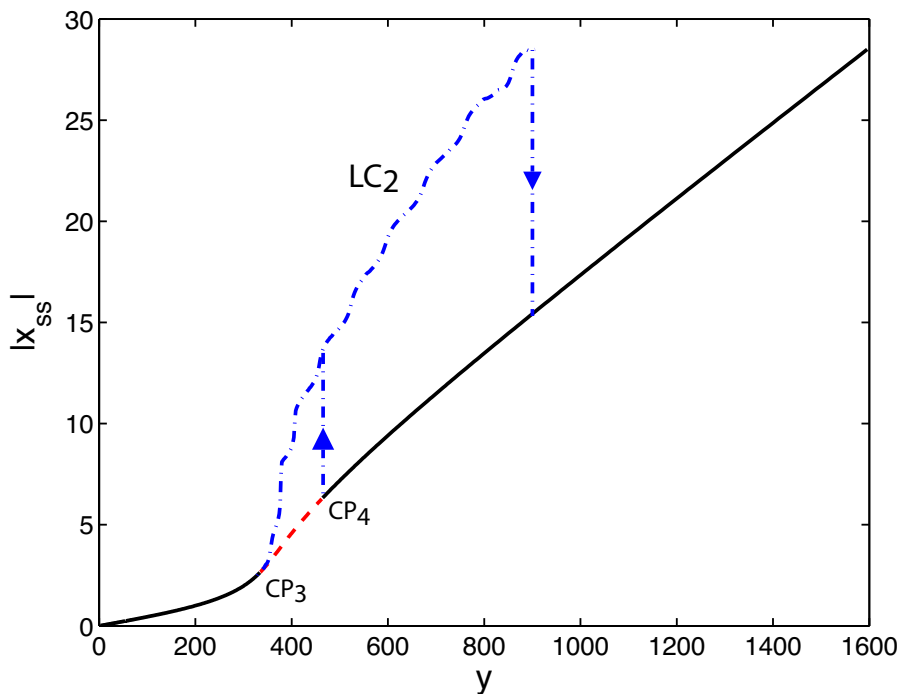
Figure 3.8: Semiclassical calculation of the intracavity steady-state field magnitude $|x_{ss}|$ versus drive field y. The parameter values are: $C = 200, k = .05, \gamma = 2, \theta = -55$, and $\Lambda = 2$. The upper dashed-dotted curve (LC_2) represents the steady-state oscillation maximum (steady-state magnitude plus mean value) associated with the limit cycle formed when the fixed point becomes unstable due to a Hopf bifurcation. The critical point CP_3 is supercritical, whereas the point CP_4 is subcritical. Note the coexistence of a stable fixed point and limit cycle in the range $475 \lesssim y \lesssim 925$. The lower dashed curve is unstable.

noise (which one could attribute to transient localization on the fixed point). Such intermittency can also be seen in Figure 3.10c, which corresponds to a drive field, $y = 1400$, well past the semiclassical region of multi-stability.
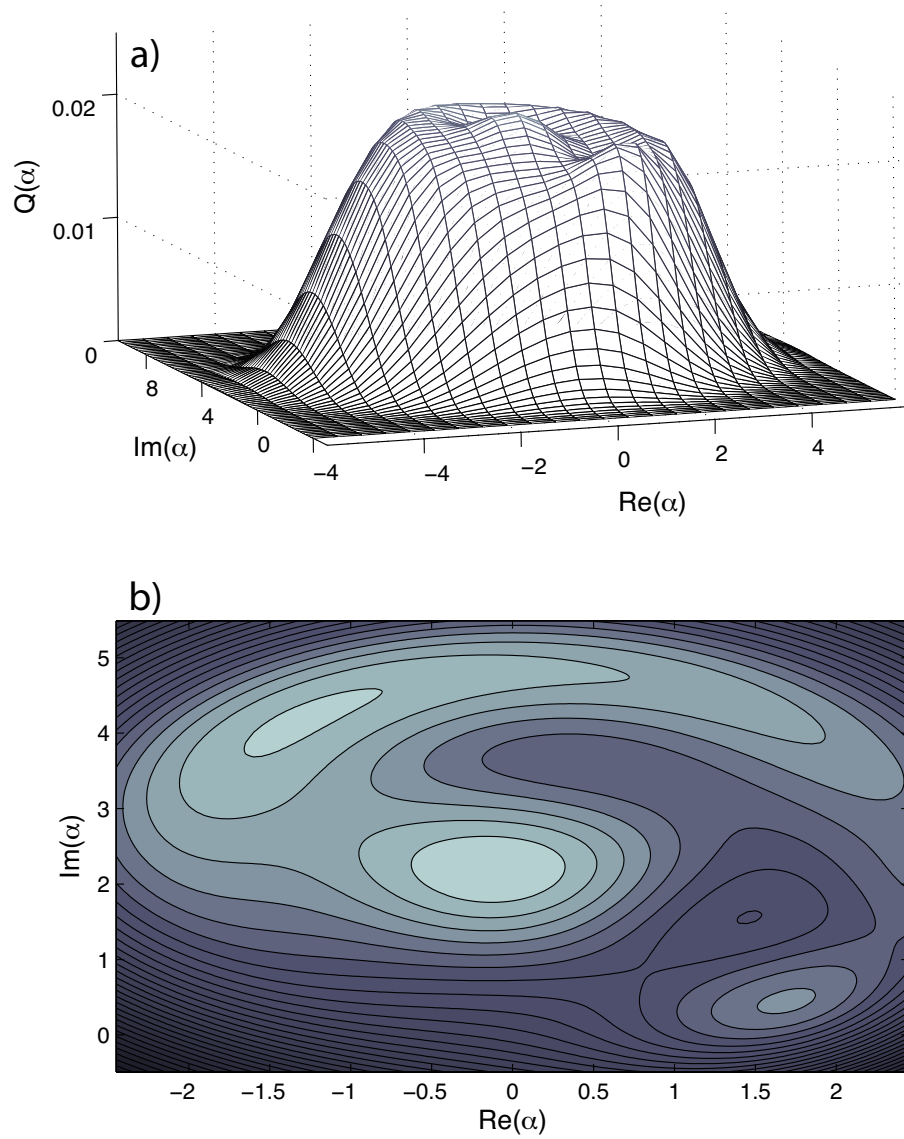
Figure 3.9: Steady-state surface (a) and contour plots (b) of $Q(\alpha)$ for the parameter values in Figure 3.8, and drive field $y = 1000$.
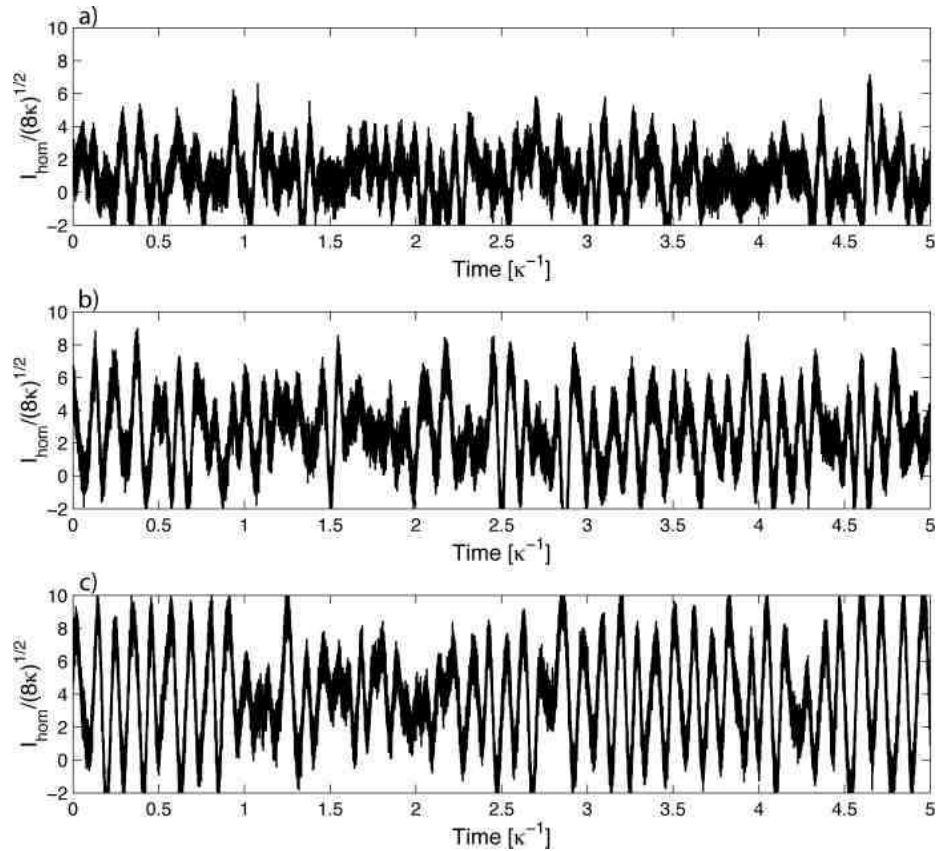
Figure 3.10:   Homodyne photocurrent from quantum trajectory simulations with parameter values in Figure 3.8. (a) drive field $y = 500$, near the subcritical bifurcation point; (b) for drive field $y = 1000$, near the oscillation amplitude maximum; (c) for drive field $y = 1400$, beyond the region of semiclassical bistability.

Bibliography

[1] R. J. Thompson, G. Rempe, and H. J. Kimble, "Observation of normal-mode splitting for an atom in an optical cavity," *Phys. Rev. Lett.*, vol. 68, p. 1132, 1992. vi, 1, 6

[2] K. M. Birnbaum, A. Boca, R. Miller, A. D. Boozer, T. E. Northup, and H. J. Kimble, "Photon blockade in an optical cavity with one trapped atom," *Nature*, vol. 436, p. 87, 2005. vi, 1, 6

[3] P. Alsing and H. Carmichael, "Spontaneous dressed-state polarization of a coupled atom and cavity mode," *Quantum Opt.*, vol. 3, p. 13, 1991. vi, 1, 8, 30, 40, 92, 104

[4] S. Y. Kilin and T. B. Krinitskaya, "Single-atom phase bistability in a fundamental model of quantum optics," *J. Opt. Soc. Am. B*, vol. 8, no. 11, p. 2289, 1991. vi, 8, 92

[5] H. Mabuchi and A. C. Doherty, "Cavity Quantum Electrodynamics: Coherence in Context," *Science*, vol. 298, p. 1372, November 2002. 1

[6] H. Carmichael, *An Open Systems Approach to Quantum Optics.* Berlin: Springer, 1993, vol. m18. 1, 2, 4, 8, 10, 22, 36, 93, 96

[7] E. T. Jaynes and F. W. Cummings, "Comparison of quantum and semiclassical radiation theories with application to the beam maser," *Proc. IEEE*, vol. 51, p. 89, 1963. 1, 5

[8] M. G. Raizen, R. J. Thompson, R. J. Brecha, H. J. Kimble, and H. Carmichael,

"Normal-Mode Splitting and Linewidth Averaging for Two-State Atoms in an Optical Cavity," *Phys. Rev. Lett.*, vol. 63, no. 3, p. 240, 1989.

[9] G. Rempe, R. J. Thompson, R. J. Brecha, W. D. Lee, and H. J. Kimble, "Optical Bistability and Photon Statistics in Cavity Quantum Electrodynamics," *Phys. Rev. Lett.*, vol. 67, no. 13, p. 1727, 1991. 24, 96

[10] Q. A. Turchette, C. J. Hood, W. Lange, H. Mabuchi, and H. J. Kimble, "Measurement of conditional phase shifts for quantum logic," *Phys. Rev. Lett.*, vol. 75, p. 4710, 1995.

[11] H. Mabuchi, J. Ye, and H. J. Kimble, "Full observation of single-atom dynamics in cavity QED," *Appl. Phys. B*, vol. 68, p. 1095, 1999. 1, 15, 60, 71

[12] G. Nogues, A. Rauschenbeutel, S. Osnaghi, M. Brune, J. M. Raimond, and S. Haroche, "Seeing a single photon without destroying it," *Nature*, vol. 400, p. 239, 1999.

[13] W. P. Smith, J. E. Reiner, L. A. Orozco, S. Kuhr, and H. M. Wiseman, "Capture and Release of a Conditional State of a Cavity QED System by Quantum Feedback," *Phys. Rev. Lett.*, vol. 89, p. 133601, 2002. 1

[14] E. L. Raab, M. Prentiss, A. Cable, S. Chu, and D. E. Pritchard, "Trapping of neutral Na atoms with radiation pressure," *Phys. Rev. Lett.*, vol. 59, p. 2631, 1987. 1, 60

[15] P. D. Lett, R. N. Watts, C. I. Westbrook, W. D. Phillips, P. L. Gould, and H. J. Metcalf, "Observation of atoms laser cooled below the Doppler limit," *Phys. Rev. Lett.*, vol. 61, p. 169, 1988. 60

[16] L.-A. Wu, H. J. Kimble, J. L. Hall, and H. Wu, "Generation of squeezed states by parametric down conversion," *Phys. Rev. Lett.*, vol. 57, no. 20, p. 2520, 1986. 55

[17] J. Ye, D. W. Vernooy, and H. J. Kimble, "Trapping of single atoms in cavity QED," *Phys. Rev. Lett.*, vol. 83, p. 4987, 1999. 60

[18] C. J. Hood, T. W. Lynn, A. C. Doherty, A. S. Parkins, and H. J. Kimble, "The atom-cavity microscope: Single atoms bound in orbit by single photons," *Science*, vol. 287, no. 5457, p. 1447, 2000. 1, 6

[19] G. T. Foster, L. A. Orozco, H. M. Castro-Beltran, and H. J. Carmichael, "Quantum State Reduction and Conditional Time Evolution of Wave-Particle Correlations in Cavity QED," *Phys. Rev. Lett.*, vol. 85, p. 3149, 2000. 1

[20] M. A. Armen and H. Mabuchi, "Low-lying bifurcations in cavity quantum electrodynamics," *Phys. Rev. A*, vol. 73, p. 063801, June 2006. 1, 9, 37

[21] P. Berman, Ed., *Cavity Quantum Electrodynamics*. San Diego: Academic Press, 1994. 1, 10, 92

[22] H. Carmichael, "Quantum fluctutations in absorptive bistability without adiabatic elimination," *Phys. Rev. A*, vol. 33, no. 5, p. 3262, 1986. 4, 8, 97

[23] A. Boca, R. Miller, K. M. Birnbaum, A. D. Boozer, J. McKeever, and H. J. Kimble, "Observation of the Vacuum Rabi Spectrum for One Trapped Atom," *Phys. Rev. Lett.*, vol. 93, no. 233603, 2004. 6

[24] B. Dayan, A. S. Parkins, T. Aoki, E. P. Ostby, K. J. Vahala, and H. J. Kimble, "A photon turnstile dynamically regulated by one atom," *Science*, vol. 319, no. 5866, p. 1062, 2008. 6

[25] B. Mollow, "Power spectrum of light scattered by two-level systems," *Phys. Rev.*, vol. 188, no. 5, p. 1969, 1969. 8

[26] C. Cohen-Tannoudji, J. Dupont-Roc, and G. Grynberg, *Atom-Photon Interactions: Basic Processes and Applications*, 2nd ed. New York: Wiley-Interscience, 1998. 8, 15

[27] M. A. Armen, A. E. Miller, and H. Mabuchi, "Spontaneous single-atom phase switching of multi-photon fields with sub-attojoule dissipated energy," April 2009, submitted. 8

[28] H. Mabuchi and H. M. Wiseman, "Retroactive Quantum Jumps in a Strongly Coupled Atom-Field System," *Phys. Rev. Lett.*, vol. 81, no. 21, p. 4620, November 1998. 8, 38, 104

[29] K. Srinivasan and O. Painter, "Linear and nonlinear optical spectroscopy of a strongly coupled microdisk-quantum dot system," *Nature*, vol. 450, no. 7171, p. 862, 12 2007. 9

[30] A. Faraon, I. Fushman, D. Englund, N. Stoltz, P. Petroff, and J. Vuckovic, "Coherent generation of non-classical light on a chip via photon-induced tunnelling and blockade," *Nat Phys*, vol. 4, no. 11, p. 859, 11 2008. 9

[31] H. Gang, C.-Z. Ning, and H. Haken, "Codimension-two bifurcations in single-mode optical bistable systems," *Phys. Rev. A*, vol. 41, no. 5, p. 2702, 1990. 92, 104, 105

[32] H. Gang, C. Z. Ning, and H. Haken, "Distribution of subcritical Hopf bifurcations and regular and chaotic attractors in optical bistable systems," *Phys. Rev. A*, vol. 41, no. 7, p. 3975, 1990. 92

[33] L. Mandel and E. Wolf, *Optical Coherence and Quantum Optics.* New York: Cambridge University Press, 1995. 12, 21, 27, 28, 66

[34] A. E. Siegman, *Lasers.* Sausalito, CA: University Science Books, 1986. 15, 43, 44, 45

[35] D. Walls and G. Milburn, *Quantum Optics*, 2nd ed. Springer, 2008. 17, 19, 27, 28, 37, 62, 112

[36] C. W. Gardiner and P. Zoller, *Quantum Noise*, 2nd ed. New York: Springer, 2000. 17

[37] L. A. Lugiato, *Theory of Optical Bistability.* Amsterdam: Elsevier Science, 1984, vol. XXI, p. 69. 21, 24, 96, 97, 98

[38] Q. Turchette, "Quantum optics with single atoms and single photons," Ph.D. dissertation, California Institute of Technology, 1997. 22

[39] C. J. Hood, "Real-time measurement and trapping of single atoms by single photons," Ph.D. dissertation, California Institute of Technology, 2000. 22, 51

[40] S. McCall and H. Gibbs, "Optical bistability," in *Proceedings of the International Conference on Optical Bistability*, C. Bowden, M. Ciftan, and H. Robl, Eds. New York: Plenum, 1981, p. 1. 24

[41] H. Gibbs, *Optical Bistability: Controlling Light Within Light.* New York: Academic Press, 1985. 24

[42] A. Szoke, V. Daneu, J. Goldhar, and N. Kurnit, "Bistable optical element and its applications," *Appl. Phys. Lett.*, vol. 15, p. 376, 1969. 24

[43] C. Savage and H. Carmichael, "Single-atom optical bistability," *IEEE J. Quan. Elec.*, vol. 24, no. 8, p. 1495, 1988. 24, 92

[44] M. Lax, "Quantum Noise IV. Quantum Theory of Nosie Sources," *Phys. Rev.*, vol. 145, no. 1, p. 110, 1966. 35, 86

[45] H. M. Wiseman and G. Milburn, "Quantum theory of field-quadrature measurements," *Phys. Rev. A*, vol. 47, no. 1, p. 642, 1993. 36, 37, 38

[46] C. W. Gardiner, A. S. Parkins, and P. Zoller, "Wave-function quantum stochastic differential equations and quantum-jump simulation methods," *Phys. Rev. A*, vol. 46, no. 7, p. 4363, 1992. 36

[47] L. Bouton, R. van Handel, and M. James, "A discrete invitation to quantum filtering and feedback control," *SIAM Review*, vol. 51, p. 239, 2009. 36, 38

[48] R. van Handel and H. Mabuchi, "Quantum Projection Filter for a Highly Non-linear Model in Cavity QED," *J. Opt. B: Quantum Semiclass. Opt.*, vol. 7, p. S226, 2005. 37, 38

[49] C. W. Gardiner, *Handbook of Stochastic Methods*, 2nd ed. Springer, 2002. 37

[50] H. M. Wiseman, "Quantum trajectories and quantum measurement theory," *Quantum Semiclass. Opt.*, vol. 8, p. 205, 1996. 37

[51] G. Sarma, "The third bowl effect," private communication. 37, 59

[52] S. M. Tan, "A computational toolbox for quantum and atomic optics," *J. Opt. B: Quantum Semiclass. Opt.*, vol. 1, p. 424, 1999. 38

[53] G. Rempe, R. J. Thompson, H. J. Kimble, and R. Lalezari, "Measurement of ultralow losses in an optical interferometer," *Optics Letters*, vol. 17, no. 5, p. 363, 1992. 43

[54] C. J. Hood, H. J. Kimble, and J. Ye, "Characterization of high-finesse mirrors: Loss, phase shifts, and mode structure in an optical cavity," *Phys. Rev. A*, vol. 64, no. 033804, 2001. 43, 45

[55] D. A. Steck. Cesium D line data. [Online]. Available: http://george.ph.utexas.edu/dsteck/alkalidata/cesiumnumbers.pdf 46, 51, 53, 57

[56] Epoxy Technology, "H21D." [Online]. Available: http://www.epotek.com/ 47

[57] E. Rivin, *Passive Vibration Isolation*. New York: ASME Press, 2003. 48

[58] J. Rao, *Advanced Theory of Vibrations*. New York: John Wiley & Sons, 1992. 48

[59] QWIKI, "RTV615." [Online]. Available: http://qwiki.stanford.edu/wiki/RTV615 48

[60] A. Abramovici, T. Lyons, and F. Raab, "Measured limits to contamination of optical surfaces by elastomers in vacuum," *Applied Optics*, vol. 34, no. 1, p. 183, 1995. 48

[61] J. C. Snowdon, *Vibration and shock in damped mechanical systems.* New York: John Wiley & Sons, 1968. 49

[62] K. M. Birnbaum. Ultra-high vacuum chambers. [Online]. Available: http://www.its.caltech.edu/~qoptics/Vacuum/UHV_chambers_updated.pdf 49

[63] Y. Sasaki, "A survey of vaccum material cleaning procedures: A subcommittee report of the american vacuum society recommended practices committee," *J. Vac. Sci. Technol. A*, vol. 9, no. 3, p. 2025, 1991. 49

[64] G.C.G. Corp., Glendale, Ca. 49

[65] K. Birnbaum, "Cavity QED with Multilevel Atoms," Ph.D. dissertation, California Institute of Technology, 2005. 51, 52, 61

[66] J. K. Stockton, "Continuous Quantum Measurement of a Cold Atomic Ensemble," Ph.D. dissertation, California Institute of Technology, 2006. 52

[67] H. P. Yuen and V. W. Chan, "Noise in homodyne and heterodyne detection," *Optics Letters*, vol. 8, no. 3, p. 177, 1983. 55, 64

[68] C. E. Wieman and L. Hollberg, "Using diode lasers for atomic physics," *Rev. Sci. Instrum.*, vol. 62, no. 1, p. 1, 1991. 57

[69] K. MacAdam, A. Steinbach, and C. Wieman, "A narrow-band tunable diode laser system with grating feedback and a saturated absorption spectrometer for cs and rb," *Am. J. Phys.*, vol. 60, no. 12, p. 1098, 1992. 57

[70] R. W. P. Drever, J. L. Hall, F. V. Kowalski, J. Hough, G. M. Ford, A. J. Munley, and H. Ward, "Laser phase and frequency stabilization using an optical resonator," *Appl. Phys. B*, vol. 31, p. 97, 1983. 57

[71] J. Shirley, "Modulation transfer processes in optical heterodyne saturation spectroscopy," *Optics Letters*, vol. 7, no. 11, p. 537, 1982. 57

[72] J. L. Hall, L. Hollberg, T. Baer, and H. G. Robinson, "Optical heterodyne saturation spectroscopy," *Appl. Phys. Lett.*, vol. 39, p. 680, 1981. 57

[73] P. Horowitz and W. Hill, *The Art of Electronics*, 2nd ed. Cambridge, England: Cambridge University Press, 1989. 58, 71

[74] Photline Technologies, "NIR-MPX800-LN." [Online]. Available: http://www.photline.com/ 58

[75] D. E. Pritchard, E. L. Raab, V. Bagnato, C. E. Wieman, and R. N. Watts, "Light traps using spontaneou forces," *Phys. Rev. Lett.*, vol. 57, p. 310, 1986. 60

[76] A. M. Steane, M. Chowdhury, and C. J. Foot, "Radiation force in a magneto-optical trap," *J. Opt. Soc. Am. B*, vol. 9, p. 2142, 1992.

[77] P. Ungar, D. Weiss, E. Riis, and S. Chu, "Optical molasses and multilevel atoms: theory," *J. Opt. Soc. Am. B*, vol. 6, p. 2058, 1989.

[78] W. Demtroder, *Laser Spectroscopy*, 2nd ed. New York: Springer-Verlag, 1996. 60

[79] J. Dalibard and C. Cohen-Tannoudji, "Laser cooling below the doppler limit by polarization gradients: simple theoretical models," *J. Opt. Soc. Am. B*, vol. 6, p. 2023, 1989. 60

[80] Y. Castin, H. Wallis, and J. Dalibard, "Limit of doppler cooling," *J. Opt. Soc. Am. B*, vol. 6, p. 2046, 1989.

[81] J. McKeever, "Trapped atoms in cavity qed for quantum optics and quantum information," Ph.D. dissertation, California Institute of Technology, 2004. 60

[82] A. Miller, Ph.D. dissertation, Stanford University, 2010. 60

[83] Canadian Instrumentation & Research Ltd. [Online]. Available: http://www.cirl.com/ 60

[84] SAES Getters. [Online]. Available: http://www.saesgetters.com 60

[85] M. Collett, R. Loudon, and C. Gardiner, "Quantum theory of optical homodyne and heterodyne detection," *Journal of Modern Optics*, vol. 34, no. 6, p. 881, 1987. 62, 64, 65

[86] C. W. Gardiner and M. J. Collett, "Input and ouput in damped quantum systems: Quantum stochastic differential equations and the master equation," *Phys. Rev. A*, vol. 31, no. 6, p. 3761, 1985. 62

[87] P. L. Kelley and W. H. Kleiner, "Theory of Electromagnetic Field Measurment and Photoelectron Counting," *Phys. Rev.*, vol. 136, no. 2A, p. A316, 1964. 62

[88] H. J. Kimble and L. Mandel, "Photoelectric detection of polychromatic light," *Phys. Rev. A*, vol. 30, no. 2, p. 844, 1984. 62

[89] P. C. Hobbs, *Building Electro-Optical Systems: Making It All Work*, J. W. Goodman, Ed. Wiley-Interscience, 2000. 66

[90] J. Graeme, *Photodiode Amplifiers: OP AMP Solutions*, 1st ed. McGraw-Hill Professional, 1995. 66

[91] Hamamatsu Photonics, "S3883." [Online]. Available: http://www.hamamatsu.com/ 66

[92] P. C. Hobbs, "Photodiode front ends: The real story," *Optics and Photonics News*, p. 42, April 2001. 66

[93] R. Durbin, S. Eddy, A. Krogh, and G. Mitchison, *Biological Sequence Analysis: Probabilistic Models of Proteins and Nucleic Acids*. Cambridge, England: Cambridge University Press, 1998. 78, 79

[94] P. Mandel, *Theoretical Problems in Cavity Nonlinear Optics.* Cambridge, England: Cambridge University Press, 1997. 92, 96

[95] H. M. Wiseman and A. C. Doherty, "Optimal unravellings for feedback control in linear quantum systems," *Phys. Rev. Lett.*, vol. 94, p. 070405, 2005. 92

[96] S. Habib, K. Jacobs, and K. Shizume, "Emergence of chaos in quantum systems far from the classical limit," *Phys. Rev. Lett.*, vol. 96, p. 010403, 2006. 92

[97] A. Vardi and J. R. Anglin, "Bose-einstein condensates beyond mean field theory: Quantum backreaction as decoherence," *Phys. Rev. Lett.*, vol. 86, p. 568, 2001. 92

[98] A. V. Kozlovskii and A. N. Oraevskii, "Removal of single-atom optical bistability by quantum fluctuations," *J. Exp. Theor. Phys.*, vol. 88, p. 1095, 1999. 92

[99] C. J. Hood, M. S. Chapman, T. W. Lynn, and H. J. Kimble, "Real-time cavity qed with single atoms," *Phys. Rev. Lett.*, vol. 80, p. 4157, 1998. 92

[100] T. Wellens and A. Buchleitner, "Bistability and stochastic resonance in an open quantum system," *Chem. Phys.*, vol. 268, p. 131, 2001. 92

[101] A. T. Rosenberger, L. A. Orozco, H. J. Kimble, and P. D. Drummond, "Absorptive optical bistability in two-state atoms," *Phys. Rev. A*, vol. 43, p. 6284, 1991. 96

[102] L. A. Orozco, H. J. Kimble, A. T. Rosenberger, L. A. Lugiato, M. L. Asquini, M. Brambilla, and L. M. Narducci, "Single-mode instability in optical bistability," *Phys. Rev. A*, vol. 39, p. 1235, 89. 103

[103] H. Gang and Y. Guo-jian, "Instability in injected-laser and optical-bistable systems," *Phys. Rev. A*, vol. 38, p. 1979, 1988. 103

[104] K. Wiesenfeld and B. McNamara, "Small-signal amplification in bifurcating dynamical systems," *Phys. Rev. A*, vol. 33, no. 1, p. 629, 1986. 104

[105] J. Guckenheimer and P. Holmes, *Nonlinear Oscillations, Dynamical Systems, and Bifurcations of Vector Fields.* New York: Springer-Verlag, 1983. 107, 108